

**Quantum Thermal Transport in Disordered Media using Atomistic Simulation and
Machine Learning**

by

Amirreza Hashemi

Bachelor of Science, Mechanical Engineering, Isfahan University of Technology, 2012
Master of Science, Mechanical Engineering, The University of Akron, 2015
Master of Science, Applied Mathematics, The University of Akron, 2016

Submitted to the Graduate Faculty of the
Swanson School of Engineering in partial fulfillment
of the requirements for the degree of
Doctor of Philosophy

University of Pittsburgh

2022

UNIVERSITY OF PITTSBURGH

SWANSON SCHOOL OF ENGINEERING

This dissertation was presented

by

Amirreza Hashemi

It was defended on

January 24, 2022

and approved by

Karl Johnson, Ph.D., William Kepler Whiteford Professor, Department of Chemical & Petroleum Engineering

Guofeng Wang, Ph.D., Associate Professor, Department of Mechanical Engineering and Materials Science

Alan McGaughey, Ph.D., Professor, Department of Mechanical Engineering and Department of Materials Science and Engineering (secondary), Carnegie Mellon University

Dissertation Director: Sangyeop Lee, Ph.D., Associate Professor, Department of Mechanical Engineering and Materials Science and Department of Physics (secondary)

Copyright © by Amirreza Hashemi

2022

Quantum Thermal Transport in Disordered Media using Atomistic Simulation and Machine Learning

Amirreza Hashemi, PhD

University of Pittsburgh, 2022

Topological disorder provides tremendous opportunities to design and manipulate solid materials due to added degrees of freedom to the atomistic structures. Disorder directly impacts electric, magnetic, thermal, electrical and mechanical properties. In many disordered materials, the engineering electronic properties are interlocked on understanding the relationship between the topological disorder and thermal transport. However, this requires a multidisciplinary approach that combines the structural and transport properties.

In the first phase of this thesis, we focus on thermal transport in the amorphous silicon structure. Several recent experimental and computational studies show that the thermal conductivity of amorphous silicon varies with sample size. This suggests that phonon-like propagating vibrational modes carry a significant amount of heat in amorphous silicon. In this work, we show the dependence of the propagon thermal conductivity to the structural medium-range order (MRO) which has been uncorroborated in previous studies. The results indicate that the structures with MRO show significantly larger propagon thermal conductivity than the structures without MRO. As the extent of MRO depends on the material preparation method, our study suggests that the thermal conductivity of amorphous Si also should depend on the material preparation methods.

We also tackled quantum thermal transport across grain boundaries in graphene. For disordered structures like GBs, developing a high-fidelity machine learning interatomic potential (MLIP) requires a large training dataset due to the variation of GBs and large configurational

space. In this work, we present an efficient approach based on the small set of GBs to develop MLIPs while covering the entire configurational space. The simulation results unveil the interplay of dislocation density with out-of-plane buckling. We revealed the influence of GB buckling on the scattering of flexural modes. Furthermore, we lay the foundation to expand the current framework to mode resolved atomistic Green's function in order to obtain a full phonon scattering matrix.

Table of Contents

1.0 Introduction.....	1
1.1 . Contributions	4
2.0 Dependence of Propagon Thermal Conductivity on Medium-range Order in Amorphous Si.....	7
2.1 Background.....	7
2.2 Atomistic Structure	10
2.2.1 Dihedral Angle Distribution.....	11
2.2.2 Fluctuation Electron Microscopy	12
2.3 Thermal Conductivity Calculation	14
2.3.1 Allen Feldman Thermal Conductivity a Green-Kubo Approach.....	14
2.4 Vibrational Mode Properties and Analysis	20
2.4.1 Dynamic Structural Factor	20
2.4.2 Calculation of Lifetimes and Thermal Conductivity using Mormal Mode Decomposition	21
2.5 Summary	26
3.0 Graphene Grain Boundary, Atomistic Green’s Function, and Transport Properties.....	28
3.1 Grain Boundary Structure	28
3.2 Machine Learning Interatomic Potential.....	30
3.2.1 Gaussian Approximation Potential	31
3.3 Landauer Formula and Ballistic Transport.....	34

3.4 Atomistic Green's Function.....	36
3.4.1 What is Green's Function?.....	36
3.4.2 Dynamical System of Equations for a Harmonic System.....	38
3.4.3 Atomistic Green's Function for a Decoupled Device with Two Contacts.....	39
3.4.4 Surface Green's Function.....	43
3.4.4.1 Analytical Approach to Solve Surface Green's Function	43
3.4.4.2 Decimation Technique to Solve Surface Green's Function	44
3.4.5 Self-energy and Coupled Green's Function.....	47
3.4.6 Transmission Function and Transmittance.....	50
3.4.7 Local Density of States.....	55
3.4.7.1 Remarks.....	59
4.0 Quantum Phonon Transport Across Grain Boundaries in Graphene using	
Machine Learning Based on Small Dataset.....	61
4.1 Introduction	61
4.2 Methods	64
4.2.1 Identifying the Small Set of GBs Representing the Entire Configurational	
Space of GBs	64
4.2.2 Training GAP	69
4.2.3 AGF Simulation.....	71
4.3 Results and Discussions.....	72
4.4 Conclusion	83
5.0 Mode Resolved Atomistic Green's Function	86
5.1 Bloch Wave.....	86

5.2 Mode Matching Approach.....	87
5.3 Bloch Theorem and Bloch Matrix.....	91
5.4 Combined Approach: Mode-matching Approach with Green’s Function Solution	94
5.5 Transmission Matrix and Transmission Coefficient.....	98
5.6 The Caroli Expression.....	100
5.7 Remarks.....	103
5.8 Verifications	104
5.9 Appendices	107
5.9.1 Appendix A: Boundary Condition for the Left Side of the Device.....	107
5.9.2 Appendix A: Boundary Condition for the Right Side of the Device	108
5.9.3 Appendix B: Mode Group Velocity	108
5.9.4 Appendix C: Gram-Schmidt Procedure and QR Decomposition	109
5.9.5 Appendix D: Propagating Waves	110
6.0 Summary and Future Directions.....	111
6.1 Summary	111
6.2 Future Directions.....	112
Bibliography	116

List of Tables

Table 1 Fitting of propagon lifetimes (B in THz²-s for ω^{-2} and THz³-s for ω^{-3})	24
Table 2 List of the 20 GBs with their structural properties. The 5 representative GBs chosen by the SOAP dissimilarity analysis are indicated with superscripts † and ‡ for the structures relaxed by TSF and DFT, respectively.	66
Table 3 List of hyperparameters for GAPTSF and GAPDFT	70

List of Figures

Figure 1 Prospective views of a-Si structures for (a) CRN (b) MROC (c) MROR, the blue and grey lines indicate regions with SRO and MRO respectively. The length of all three structures is 3.28nm. The figure is from Ref. [11]. 11

Figure 2 Dihedral angle distribution in the MRO and CRN structures 12

Figure 3 Calculated FEM for MRO and CRN structures 14

Figure 4 Comparison of DOS for MRO and CRN structures with an eyeguide for the ω^2 scaling 16

Figure 5 Comparison of mode diffusivity for different structures. The dashed line located at 2 THz shows the distinction of the propagon and diffuson modes 17

Figure 6 Propagon and A-F thermal conductivity values for the different structures. The propagon thermal conductivity (κ_{pr}) is roughly estimated as $\kappa_{GK}-\kappa_{AF}$ 19

Figure 7 Dynamic structural factor for two wavevectors representing propagon and diffuson: (a) longitudinal and (b) transverse structural factors for propagons and (c) longitudinal and (d) transverse structural factors for diffusons 21

Figure 8 Lifetimes and fitted lines for (a) MROR (b) MROC (c) CRN structures and (d) the zoom-in comparison of three structures in the propagon frequency range. 23

Figure 9 Propagon and A-F thermal conductivity values for the different structures. The propagon thermal conductivity is predicted by extrapolating the lifetime of propagons to low frequency limit using NMD. The left and right figures assume the ω^{-2} and ω^{-3} 26

Figure 10 A typical structure containing two identical GBs with periodic boundary conditions along both the directions parallel and perpendicular to the GB direction. Each

rectangle formed by the dashed line represents one unit cell. The lattice vectors of the two grains forming the GB are (a_{i1}, a_{i2}) , with $i=1, 2$ for grains 1 and 2, respectively. The tilt angle between the chiral vector $L_i = n_{i1}a_{i1} + n_{i2}a_{i2}$ and the lattice vector along the armchair direction a_{i2} is θ_i . The GB is characterized by the misorientation angle $\theta_M = \theta_1 + \theta_2$ and the boundary line angle $\theta_L = |\theta_1 - \theta_2|$ 28

Figure 11 Constructing a supercell by matching the hexagonal rings at the right boundary of A and left boundary of B. The atoms 1 and 2 are labeled by 1' and 2' after rotating A by 180° . The periodic structure is constructed by shifting B so that the atom 1' over 30

Figure 12 The excitation propagation of (a) retarded Green's function and (b) self-advance Green's functions 37

Figure 13 schematic view of the device with two semi-infinte contacts. Transmission direction is assumed to be left to right (from contact 1 to contact 2) 40

Figure 14 Frequency distribution exchange for the isolated contact (left) and a broadening of frequency level for a coupled system of contact and device (right) 58

Figure 16 Five representative GBs from (a) TSF and (b) DFT showing distinct features such as density of disclinations and their topological arrangements. The angle in each figure shows the misorientation angle. The green circle shows the cutoff radius for defining LAE. 69

Figure 17 Validation of GAPTSF against TSF for (a) formation energy of GBs, and (b) transmission function. The solid symbols in (a) represent GBs used for training the GAPTSF. The solid lines and dots in (b) are from GAPTSF and TSF, respectively. In (b), the two GBs with $\theta_M = 6.0^\circ$ and 48.36° and the other two GBs with $\theta_M = 9.43^\circ$ and 50.57° are from the training and testing dataset, respectively..... 72

Figure 18 Validation of GAPDFT against DFT for relaxed structures projected onto a-b plane. (a) $\theta_M=48.36^\circ$ from the training dataset and (b) $\theta_M=9.43^\circ$ from the test dataset. The color represents out-of-plane displacement in Å..... 73

Figure 19 Comparison of DFT, GAPDFT, and TSF for (a) GB formation energy, (b) core energy, and (c) strain energy. The solid symbols in (a) represent the GBs that were used for training GAPDFT. 74

Figure 20 Density of disclination for selected 20 GBs relaxed with TSF and GAPDFT showing the maximum at the θ_M of around 35° 76

Figure 21 Thermal resistance with varying misorientation angles at (a) 100 K, (b) 300 K, (c) 500 K, and (d) 1500 K. 77

Figure 22 Role of out-of-plane buckling for scattering of flexural phonon modes. (a-b) normalized thermal conductance as a function of temperature for (a) GBs showing monotonously decreasing behavior and (b) GBs showing increasing behavior at low temperatures. The values in the legends represent misorientation angle. (c) Phonon transmissivity for two representative GBs showing a remarkable difference in low phonon frequency range below 15 THz. (d) Comparison of the two representative GBs in terms of out-of-plane buckling. The color represents out-of-plane displacement of atoms and the pentagon and heptagon are marked in blue and red, respectively..... 79

Figure 23 Comparison of magnitudes of self-interaction force constants from GAPDFT and TSF for a training structure with $\theta_M=48.36^\circ$ and a test structure with $\theta_M=9.43^\circ$. The difference between GAPDFT and TSF is as large as 35%..... 81

Figure 24 Comparison of TSF and GAPDFT showing inaccuracy of TSF for predicting force constants on dislocation cores. (a-b) normalized error of self-interatomic force constants,

defined as $\Delta\phi_{ii, \text{TSF}} - \Delta\phi_{ii, \text{GAPDFT}}$ where $\Delta\phi_{ii}$ is the difference of self-interaction force constants in GB and perfect graphene..... 82

Figure 25 Comparison of TSF and GAPDFT showing inaccuracy of TSF for transmission function above mid phonon frequency. (a-b) suppressed transmission function from perfect graphene for 20 GBs. The values in the legend are misorientation angles. 83

Figure 26 A Bloch wave (bottom) can be decomposed into the product of a periodic function (top) and a plane wave (center). The left side and right side represent the same Bloch wave broken up in two different ways, involving the wave vector k_1 (left) or k_2 (right). In all plots, blue is real part and red is imaginary part.[154] 87

Figure 27 Schematic view of the device with two semi-infinite contacts which are divided into Bloch units 88

Figure 28 comparison of the dispersion between mode resolved AGF and direct phonopy calculation for pure graphene structure. Blue lines show the direct calculation from phonopy and red dots are the propagating modes of left or right contact calculated from mode resolved AGF solution of pure graphene..... 105

Figure 29 comparison of total transmission functions between total transmission function calculated from equations 3-65 and 5-47 with the trace of mode resolved transmission matrices of left and right leads 106

Figure 30. Dislocations in h-BN 115

1.0 Introduction

The continuous increase of thermal loads on the devices and materials has brought thermal transport studies into the forefront of the engineering process. The demands even seem to be increasing thanks to the new frontier technologies on semiconductors, information technology, 5G, and quantum computing [1]. Thermal transport in many of these applications is predominantly conductive and according to Fourier's law, conductive thermal transport is proportional to thermal conductivity which is a second-order tensor [2]. Therefore, the thermal conductivity values of the materials are key to engineering and designing new devices.

However, unlike the electrical conductivity, the range of thermal conductivity values of dense solids at room temperature is between 1 W/m-K (amorphous materials) to 2300 W/m-K (diamond) [3] which puts some constraints on the engineering process. One solution to ease these constraints, aside from discovering new materials with high and low thermal conductivity, is to tune the structure and material processing. Another key parameter in the thermal transport of solid materials is the mean free path (MFP) which is defined as the extent to which a phonon transports in space. The range of MFP can vary from several nanometers to micrometers [2]. Both thermal conductivity and MFP are size-dependent parameters and upon the sample size. That means we should deal with these parameters vigilantly as the size of the electrical device and the technology application is inclined to routinely become smaller. In recent years, a good understanding of thermal conductivity value and MFP has been obtained for crystalline materials. Several experimental works using ultrafast lasers measured thermal conductivities, also theoretical and simulation works have demonstrated good agreements with experimental results for a large number of crystalline materials [4].

However, thermal transport in disordered media has many open questions for a variety of reasons including difficulty with consistent material processing, the lack of full understanding of how the disorder affects the scattering process, and a large number of involved structural-dependent variables to the thermal transport. This issue is the main motivation for our current research.

In this thesis, we discuss a two-phase study on thermal transport in disordered media. In the first phase, we discuss the dependence of phonon-like propagating vibrational modes (propagons) thermal conductivity on medium-range order (MRO) which is defined as 10 to 20 Å in amorphous silicon (a-Si) structure. Several recent experimental and computational studies show that the thermal conductivity of a-Si varies with sample size. [5-8] This suggests that propagons carry a significant amount of heat in a-Si. The previous computational studies used the continuous random network (CRN) atomistic structure [9, 10] that represents an ideal random structure without medium- and long-range orders.

However, recent spectroscopy results [11, 12] reveal that the actual atomistic structure of a-Si contains MRO that the CRN structure does not. Here, we show the dependence of the propagon thermal conductivity on the MRO which has not been discussed in the previous studies. We compare the extent of MRO and the propagon thermal conductivity in several model amorphous Si structures using simulated fluctuation electron microscopy, dihedral angle distribution, and molecular dynamics simulation. We use empirical potential (Tersoff) and molecular dynamics simulation to calculate the thermal conductivity of a-Si. We calculate total thermal conductivity using the Green-Kubo approach and Allen-Feldman thermal conductivity of two sets of structures with and without MRO. Two sets of structures have the same short-range order while one includes MRO and the other does not. We estimate the propagon thermal

conductivity values by subtracting Allen-Feldman thermal conductivity from total thermal conductivity. The results indicate that the structures with MRO show significantly larger propagon thermal conductivity (over 50 %) than the structures without MRO. We also provide structural factor analysis and lifetime calculation with normal mode decomposition. As the extent of MRO depends on the material preparation methods, our study suggests that the thermal conductivity of amorphous Si also should depend on the material preparation method [13].

In the second phase, we discuss a simulation framework to study quantum thermal transport across grain boundaries of graphene. The grain boundary structures are incredibly important in the design of polycrystalline materials for applications including energy storage, electronic systems, and sensors. However, thermal transport through grain boundaries with the inclusion of structural differences and bonding strengths has not been studied in-depth and with high accuracy. For the grain boundaries, the experimental works are limited and the thermal conductance values are varied significantly [14]. Analytical models to calculate the transmission function such as the acoustic mismatch model [15] and diffusive mismatch model [16, 17] fail to include the structural differences and bonding strengths. [18, 19] In terms of simulations, molecular dynamic simulations are mostly done in combination with wave-packet simulation [14, 20, 21] to find spectral transmission function; these simulations are expensive and the spectral range of calculation is limited. Another set of simulations [22-24] was done using Green's function where a few numbers of grain boundary structures were studied for graphene.

To the best of our knowledge, the past works are limited to the use of empirical potentials and the number of grain boundary structures do not include all possible structural differences. In the current research, we studied graphene GB structures with the full inclusion of the structural and bonding strength information using first principle level accuracy. The steps for the simulation

framework are a) machine learning interatomic potential which is trained by first-principle calculations b) calculation of the transmission function of grain boundary structures using quantum field theory approach known as atomistic Green's function (AGF) c) develop the mode resolved AGF that provides polarization resolved transmission information. AGF is designed to solve the non-periodic dynamical system with Hamiltonian matrices of interatomic force constants, therefore, we employ the trained machine learning-based potential into the second step to calculate the transmission function using AGF. To calculate the thermal transport, we model the grain boundary as an interfacial junction with two crystalline structures on the sides. Under the assumption of ballistic transport, we use the Landauer formula to calculate the thermal conductance and Kapitza resistance in interfacial junctions. We further show how the AGF is combined with the mode matching approach to calculate the mode resolved transmission properties of the non-periodic system. We show the validation of the mode resolved AGF for the perfect graphene structure.

1.1 . Contributions

In Chapter 2, we simulated fluctuation electron microscopy and analyzed dihedral angle distribution to distinguish the amorphous structures with and without MRO. We calculated the thermal conductivity of the amorphous structures using the Green-Kubo approach and the Allen-Feldman approach. Then we show the dynamical structure factor as evidence of the larger propagon contribution of structures with MRO. We implemented modal analysis using normal mode decomposition to confirm our proposition for the dependence of propagating vibrational modes on the MRO.

In Chapter 3, we review the previous conventional methodologies which are used in the simulation framework from structure generation to interfacial thermal conductance calculation. We introduce the method to generate the grain boundary structures of graphene. We show how machine learning potential is trained from the first principle dataset. Finally, we provide a detailed description of the Landauer formula, Green's function, and AGF. Also, we discuss the physical interpretation of AGF simulation.

In Chapter 4, we discuss ab initio phonon transport across GBs of graphene using Machine Learning Interatomic Potential (MLIP) based on a small dataset. We show a systematic approach based on the dissimilarity calculations of the local atomic environment to find the best representatives for the training of MLIPs. We provide the details of the training process and show the success of the calculations for MLIPs based on the empirical potential and ab initio data. Using AGF and MLIPs, we present the transmission function and transport properties of graphene GBs.

In Chapter 5, we discuss the details of the mode resolved AGF approach based on our understanding of the original mode matching approach, Bloch theorem, and Bloch wave representation, and the connection between the Bloch waves and transmission functions. We provide the detailed derivations of the Bloch equation and we discuss our modifications that enhance the numerical simulations of mode resolved AGF for large atomistic structures. Finally, we show the verification of the in-house code for perfect graphene and large atomistic structure.

In Chapter 6, we conclude the thesis research and present the possible future directions.

This thesis results in the following publications:

1. One published paper in the Journal of Applied Physics as a first author which discusses the research on a-Si. I conducted numerical simulations and analyzed the simulation results. The details of this paper are presented in chapter 2. [13]

2. One published paper as a co-author discusses the MLIP for crystalline Si and crystalline Si with vacancies. I helped with the implementation of the machine learning approach. [25]
3. One unpublished paper as a first author paper (under review) discusses the quantum thermal transport in graphene GBs. I assembled and conducted a simulation framework including the development of the necessary codes and analyzing the final results. The details of this paper are presented in chapters 3 and 4. [26]

2.0 Dependence of Propagon Thermal Conductivity on Medium-range Order in Amorphous Si

2.1 Background

Amorphous silicon (a-Si) is widely used in many applications, such as thin film transistors, active matrix displays, image sensor arrays, multi-junction solar cells, and multilayer color detectors. Effective thermal management is one of the key challenges in these applications, and thus it is necessary to understand thermal transport in a-Si. [27] Although the thermal conductivity of amorphous materials usually has a very weak classical size effect, recent studies showed that the thermal conductivity of a-Si largely depends on the sample size. [6-8, 28] The size dependence of the thermal conductivity in a-Si has an important implication on the thermal management of a broad range of applications, particularly where the characteristic length is in the sub-micrometer scale. [29]

Thermal transport in non-metallic solids is attributed to atomic vibrations. The vibrational eigenmodes in amorphous materials are mainly divided into two groups: propagating and non-propagating modes. The propagating modes have longer wavelengths than the non-propagating modes as amorphous materials at a sufficiently large length scale can be considered a nearly homogenous medium. For a-Si, the vibrational eigenmodes with wavelengths longer than 1.5 nm (or frequencies of less than 2 THz) are known to exhibit propagating characteristics. [9, 30] The propagating vibrational modes, called propagons, resemble phonons in crystalline solids. The thermal conductivity of the propagon can be calculated using the simple kinetic theory of phonon gas similar to the phonon thermal conductivity of crystalline materials. The non-propagating

modes are further divided into diffusons and locons; diffusons are vibrational eigenmodes that are extended into the entire amorphous sample, while locons are spatially localized. [31] The thermal conductivity of non-propagating modes is often calculated with an expression given by Allen and Feldman (here, referred to as A-F). [31-33]

In a-Si, propagons significantly contribute to thermal transport, resulting in the size-dependent thermal conductivity. [6, 7] While the non-propagons contribution is not affected by the classical size effect, the propagons contribution can be largely affected through diffuse boundary scattering. Previous experimental studies clearly show that propagon thermal conductivity is significant in a-Si. [5-8, 34] In these experimental studies, thermal conductivity strongly depends on the sample size, suggesting that the propagon largely contributes to the total thermal conductivity. Propagons are scattered by diffuse boundary scattering and they experience less scattering in large samples which results in a larger thermal conductivity. If heat is carried mostly by non-propagating modes, the thermal conductivity should not depend on the sample size as long as the sample size is large enough that the quantum size effect can be ignored. Also, numerical studies indicate that the propagon contribution to total thermal conductivity is large in a-Si compared with other amorphous materials. Larkin and McGaughey showed that the propagon thermal conductivity can be as large as 40 % in a-Si while the propagon contribution of amorphous silica is about 6 %. [9] Also, Moon et al. [28] and He et al. [35] showed that the propagon vibrations are the dominant contributor of thermal conductivity in a-Si using the structural factor and lifetime of vibrational modes.

Common amorphous structures maintain a short-range order (SRO) in the length scale less than 5 Å while they lack long-range order. [36] A continuous random network (CRN) is a good example of this notion. Atomistic structures generated from the CRN are a random-based atomic

setting with a bond-swapping algorithm. CRN builds the structure with SRO and retains the disorder beyond the second neighbor lengths such that the defects and voids are eliminated. [37] The CRN structure of a-Si contains less than 1-3% defect and void concentration. [38]

Though CRN is sufficiently reliable to represent the SRO, the recent reports on a-Si indicate that some experimentally observed structures rather exhibit low degrees of disorder and some order in the length scale of 10 to 20 Å, called medium-range order (MRO). [39, 40] An example configuration of MRO observed in a-Si is a paracrystalline phase. Paracrystalline is defined as a parallel piped structural order which embedded into the structure within a longer range than SRO. [41] In amorphous structures, it is generally difficult to find the correlation between the atoms in a long-range using atomic correlation tools such as radial distribution function (RDF). [42] Treacy and Borisenko were able to measure the existence of local order and the possibility of paracrystalline structure inclusion inside a-Si using the fluctuation electron microscopy (FEM). [11] The FEM is a hybrid diffraction/imaging technique that exhibits the topological crystallinity in the length corresponding to its probe size. They estimated that the volumetric portion of the paracrystalline phase is about 10 to 15% in their ion-implanted a-Si samples. [11] The FEM data led to the development of model a-Si structures. [43] The clear difference is that the CRN structures do not exhibit any MRO, while those based on the experimental FEM data inherit certain degrees of MRO. [40]

The evidence of MRO was reported in previous studies for a-Si structures, [44-46] and the magnitude of MRO largely depends on the materials processing method. It has been shown that a significant MRO exists in many as-deposited amorphous silicon samples. [47] In particular, deposition conditions can largely affect the MRO. For a vapor-deposited sample, the presence and magnitude of MRO increase with the temperature of the substrate. [43] One reason may be related

to the fact that the two-level tunneling system is diminished by increasing the substrate temperature. [48] Besides, post-annealing processes can affect MRO. The degree of MRO could be reduced by post-annealing of the amorphous samples, but it does not fully disappear. [11] If the thermal conductivity depends on MRO, the large variance of experimental thermal conductivity values of a-Si from the literature [5-7, 34, 49-54] may be related to the different material processing methods and conditions in addition to the different uncertainty level of each experiment. However, previous computational studies either considered the sample model similar to CRN structure [9] or used a melt-quench procedure [28, 35] to create the structure using empirical potentials. The CRN-like structures have SRO but lack MRO. To our best knowledge, the relationship between MRO and thermal conductivity in a-Si has not been studied.

In this chapter, we study the influence of MRO on propagon thermal conductivity. We examine MRO in three different model a-Si structures with the same size of 3.28 nm, using dihedral angle distribution and FEM simulations. Then, we calculate the propagon thermal conductivity using the Green-Kubo (G-K) approach, normal mode decomposition (NMD), and A-F formalisms for those structures. Finally, we discuss the relationship between MRO and propagon contribution to thermal transport.

2.2 Atomistic Structure

We use three structures with the same size (3.28 nm) but the different extent of MRO (figure 1). The two model structures that contain MRO are from literature. [11] Those structures were constructed by modifying a crystalline configuration or a fully random configuration through a hybrid-reverse Monte Carlo technique [43] such that the resulting model structures exhibit the

same MRO from the experimental FEM data. The computational cost of the generation of the structures with MRO is extremely high due to large computational cost of FEM simulations that are required to enforce the MRO constrain, which limits the sample size in the current work. In this chapter, these structures are referred to as MROC (MRO modified from Crystal) and MROR (MRO modified from Random structure). The third structure that was generated using CRN is also from literature. [37] To minimize uncertainty, 10 CRN structures were studied and the results were averaged over all CRN samples. The MRO and CRN structures have similar RDF. [11] However, RDF is based on a two-body correlation and cannot capture MRO. [55] Before performing the structure characterization and thermal transport simulations, all three structures were relaxed using the energy minimization method with Tersoff potential [56] to find the equilibrium atomistic structure at 0 K. All the simulation results presented in this work are from the Tersoff potential.

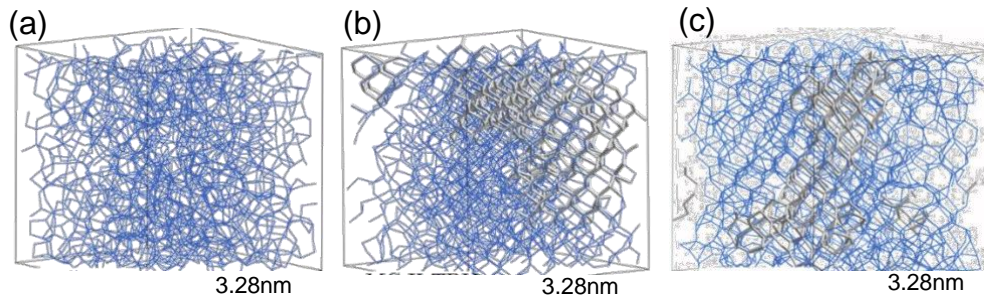


Figure 1 Prospective views of a-Si structures for (a) CRN (b) MROC (c) MROR, the blue and grey lines indicate regions with SRO and MRO respectively. The length of all three structures is 3.28nm. The figure is from Ref. [11].

2.2.1 Dihedral Angle Distribution

To estimate MRO in all three structures, first, we calculate dihedral angle distribution. A dihedral angle is an intersecting angle between two sets of three atoms having two atoms in

common and its distribution measures atomic order in a longer range than the bond angle distribution. While the bond angle distribution usually identifies SRO, the dihedral angle distribution can be used to examine MRO. [39] In figure 2, the three structures have two peaks near 60° and 180° , which are the dihedral angles of a perfect crystal Si structure. [57] However, those peaks have different widths in the three structures; the peaks of MROC and MROR are narrower and sharper than those of the CRN structure. These results agree well with previous reports [58, 59] indicating more significant MRO in the MROC and MROR structures than in the CRN structure.

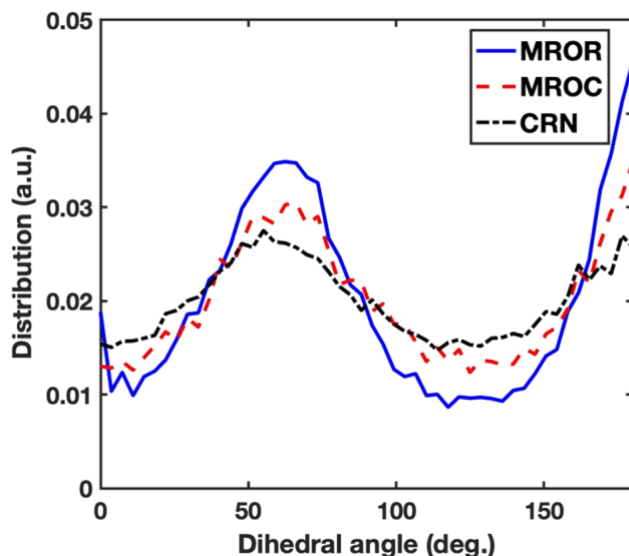


Figure 2 Dihedral angle distribution in the MRO and CRN structures

2.2.2 Fluctuation Electron Microscopy

We further analyze MRO in the three model structures using FEM. The FEM provides detailed information about the structural arrangement and orientation through three or four body

correlation while RDF measures two-body correlation. [55, 60, 61] In principle, FEM measures the normalized variance (V) of electron beam diffraction intensity defined as

$$V(\mathbf{k}, Q) = \frac{\langle I^2(\mathbf{k}, Q) \rangle}{\langle I(\mathbf{k}, Q) \rangle^2} - 1 \quad 2-1$$

where I is the beam intensity. Both variance and intensity depend on the wavevector (\mathbf{k}) of the incident electron beam and the inverse of the probe size (Q). The variance measures the fluctuation of the diffraction beam intensity. If the structure is fully random with no order in the length scale of the probe size, then the diffracted intensity pattern should be homogenous regardless of the diffraction angle. However, for the structures with MRO, the intensity has a fluctuation; the diffracted beam intensity becomes large if the incident beam sees a paracrystalline region and the Bragg's condition is satisfied. Previous studies observed a large variance in a-Si for the probe size of 10 Å, representing MRO in this length scale. [11, 40, 41, 43]

In order to identify the structural order, we change the probe size from 5 to 30 Å incrementally and perform the FEM simulation on each structure. We use FEMSIM code [62] for all the FEM simulations. We apply incident beams to a sample with 200 different orientations. The FEM probe surfs the sample over smaller cubes at different orientations of the sample. The diffraction signals are averaged over all the raster positions and orientations, which can be used to determine the variance ensemble. Among different tested probe sizes, we observe that only for the probe size of 10 Å, there is a clear significant FEM variance difference between MRO and CRN structures. Considering that the probe size of 10 Å is defined on projected two-dimensional planes, the structural orders are considered to exist roughly within 10 to 20 Å in three-dimensional space. In figure 3, we compare the variance for MRO and CRN structures calculated using a probe size of 10 Å. The variance of CRN structure is nearly constant with minimal peaks while MRO structures show large variance in the range of wavevectors between 0.2 to 0.9 Å⁻¹. The clear peak

of MRO structures around 0.3 and 0.5 \AA^{-1} indicates the existence of MRO in those model structures. While a previous study [11] shows a similar variance of MROR and MROC structures, our results show that the variance of MROR is slightly larger than that of MROC. This may originate from the number of orientations for the FEM simulation [63]; the previous study [11] used 50 orientations and we used more than 200 orientations and confirmed the convergence with respect to the number of orientations.

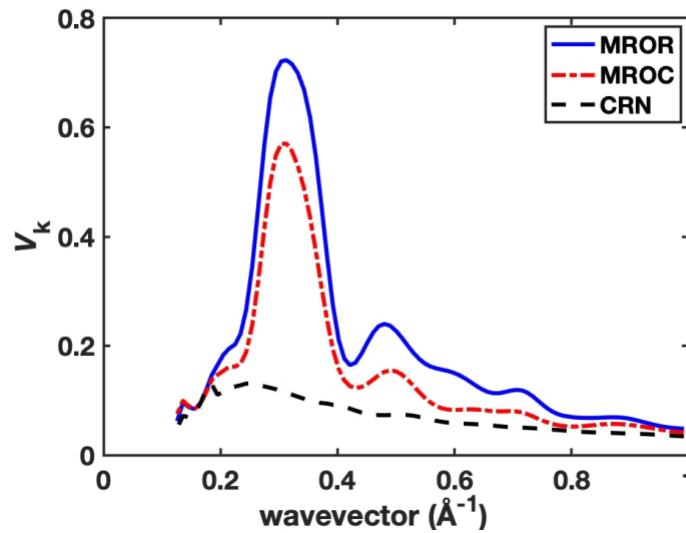


Figure 3 Calculated FEM for MRO and CRN structures

2.3 Thermal Conductivity Calculation

2.3.1 Allen Feldman Thermal Conductivity a Green-Kubo Approach

The thermal conductivity of amorphous materials can be divided into propagon contribution (κ_{pR}) and non-propagon contribution (κ_{AF})

$$\kappa_{\text{vib}} = \kappa_{\text{pr}} + \kappa_{\text{AF}}. \quad 2-2$$

The non-propagating thermal conductivity, κ_{AF} , is calculated as

$$\kappa_{\text{AF}} = \frac{1}{\Omega} \sum_{i, \omega_i > \omega_{\text{cut}}} C(\omega_i) D_{\text{AF}}(\omega_i) \quad 2-3$$

where Ω is the volume of a sample. The ω_i is the frequency of the i th diffusion mode and ω_{cut} is the cutoff frequency that distinguishes between propagating and diffusons. The $C(\omega_i) =$

$k_B \left[\frac{\hbar\omega_i/2k_B T}{\sinh(\hbar\omega_i/2k_B T)} \right]^2$ is the specific heat of vibrational eigenmodes and $D_{\text{AF}}(\omega_i)$ is the mode

diffusivity which is expressed as [32]

$$D_{\text{AF}}(\omega_i) = \frac{\pi\Omega^2}{\hbar^2\omega_i^2} \sum_{j \neq i} |S_{ij}|^2 \delta(\omega_i - \omega_j) \quad 2-4$$

where S_{ij} indicates the heat current operator [32] in the tensor form and δ is the Dirac delta function. The total thermal conductivity is calculated using the G-K formalism given as

$$\kappa_{\text{GK}} = \frac{\Omega}{3k_B T^2} \int_0^\infty \langle \mathbf{S}(t) \cdot \mathbf{S}(0) \rangle dt \quad 2-5$$

where $\mathbf{S} = (1/\Omega) [\sum_i E_i \mathbf{v}_i - \sum_{i < j} (\mathbf{f}_{ij} \cdot \mathbf{v}_j) \mathbf{r}_{ij}]$ is the heat current vector and is calculated as the summation of the potential energy and kinetic energy per atom (E_i). In the heat current vector, the \mathbf{f}_{ij} is the force between atoms i and j , the \mathbf{r}_{ij} is the distance vector of two atoms, and the \mathbf{v}_j is the velocity vector. The k_B and T are the Boltzmann constant and temperature, respectively. The integrand is the heat current autocorrelation function. We roughly estimate the propagating thermal conductivity as

$$\kappa_{\text{pr}} = \kappa_{\text{GK}} - \kappa_{\text{AF}}. \quad 2-6$$

In order to calculate κ_{AF} , we need to determine the cutoff frequency separating propagating and non-propagating modes. In the past studies [6, 9, 28, 30, 31], there exist different choices of

cutoff between propagon and diffuson using different criteria. Here we choose 2 THz for cutoff frequency based on the onset of the density of states (DOS) where it follows ω^{-2} scaling at low frequency. [9] Figure 4 shows the DOS of all three structures with an eyeguide for the ω^{-2} scaling. For all three structures, the DOS below 2 THz follows the the ω^{-2} scaling, showing that the vibrational eigenmodes below 2 THz exhibit a linear dispersion like Debye phonon dispersion of the crystalline phase.

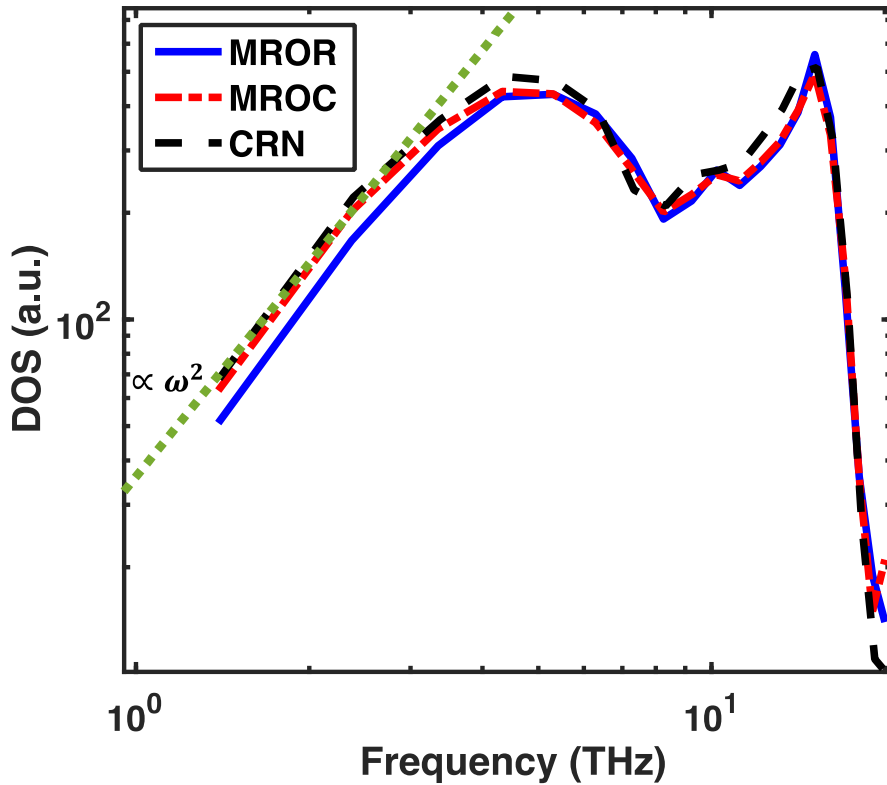


Figure 4 Comparison of DOS for MRO and CRN structures with an eyeguide for the ω^2 scaling

In addition, we present the mode diffusivity defined in Eq. 2-4 for all three structures in figure 5. We also included the mode diffusivity of the melt-quench structure with a similar size (3.28 nm) that has been widely used for thermal transport simulation. [64] It is worth mentioning that the phonon calculation for a melt-quench structure produces imaginary frequencies due to metastability; in our case, the percentage of the number of imaginary frequencies to the total

number of frequencies is less than 0.06 % and we dismiss them here. All four structures were relaxed with the Tersoff potential and mode diffusivities were calculated using the GULP package [65].

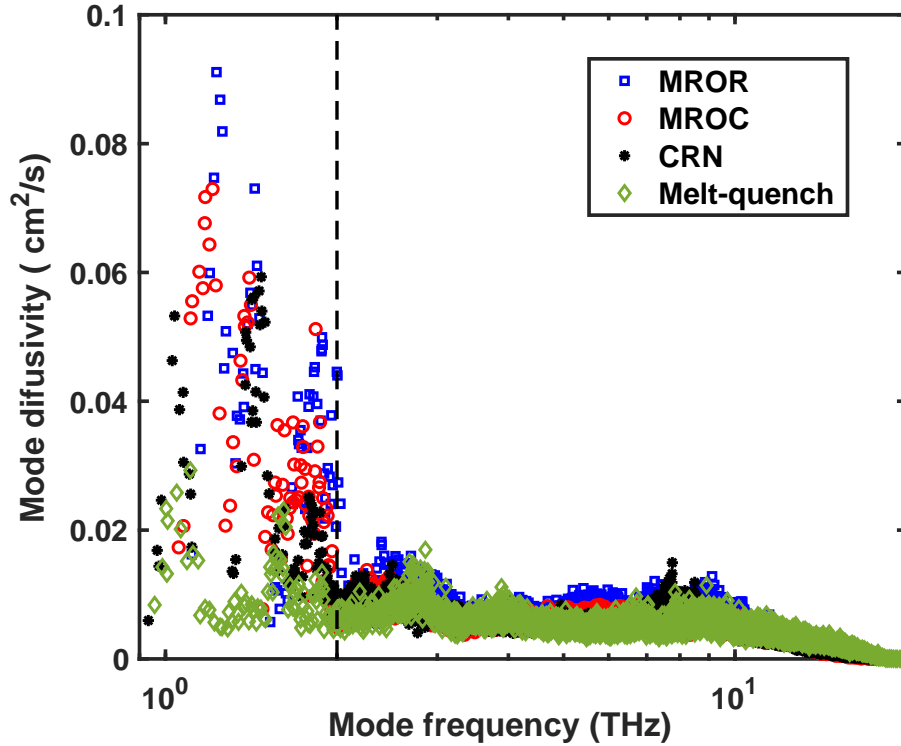


Figure 5 Comparison of mode diffusivity for different structures. The dashed line located at 2 THz shows the distinction of the propagon and diffuson modes

The mode diffusivity in figure 5 exhibits remarkably different behaviors for frequencies below and above 2 THz; it has very large values below 2 THz but shows a plateau region above 2 THz. The drastic change of mode diffusivity at around 2 THz was considered as a feature of the transition from propagon to diffuson in a previous study. [9] In addition, it was shown previously that the vibrational eigenvectors with frequencies below 2 THz show the periodic nature as is expected for propagon. [30] Thus we believe the 2 THz cutoff is a reasonable choice for all three structures.

With the cutoff frequency of 2 THz and mode diffusivity, the A-F thermal conductivity was calculated using the GULP package [65]. The broadening factor for the A-F thermal conductivity is 5 times the average mode frequency spacing (0.0016 THz) and the uncertainty of the A-F thermal conductivity is calculated by changing the broadening factor within $\pm 10\%$ differences. The A-F thermal conductivity of MROR, MROC, CRN, and melt-quench structures are 0.88 ± 0.05 , 0.7 ± 0.05 , 0.7 ± 0.05 , and 0.69 ± 0.05 W/m-K respectively. It is observed that the MROR structure has a larger A-F thermal conductivity compared to the CRN structure. A similar behavior that A-F thermal conductivity increases with the order of atomic arrangements was reported in the previous work on hydrogenated a-Si thin film. [34]

The G-K bulk thermal conductivity was calculated using LAMMPS GPU [66] with Tersoff potential [36] for Si atoms. First, we thermalized all structures at 300 K through NVT simulations which were followed by 20 million iterations of NVE with a time step of 0.5 fs for G-K calculations. We confirmed that the heat current autocorrelation function approaches a statistically stationary state for all simulation results. The G-K calculations were performed on each structure with 10 random seeds for initial velocity distribution and the final value was averaged over all the samples and seeds. We considered 20000 iterations with a lag time of 5 timesteps to perform the heat current autocorrelation calculation. The calculated G-K thermal conductivity values are shown in figure 6. The G-K thermal conductivity of MROR, MROC, and CRN structures are 1.35, 1.15, and 1.0 W/m-K, respectively.

The difference between A-F and G-K thermal conductivity values can provide a rough estimate for propagon thermal conductivity. The propagon thermal conductivity of MROR and MROC structures are as large as 0.47 and 0.45 W/m-K which are over 50 % larger than the

propagon thermal conductivity of CRN structure. This suggests that there is a strong correlation between propagon thermal conductivity and MRO.

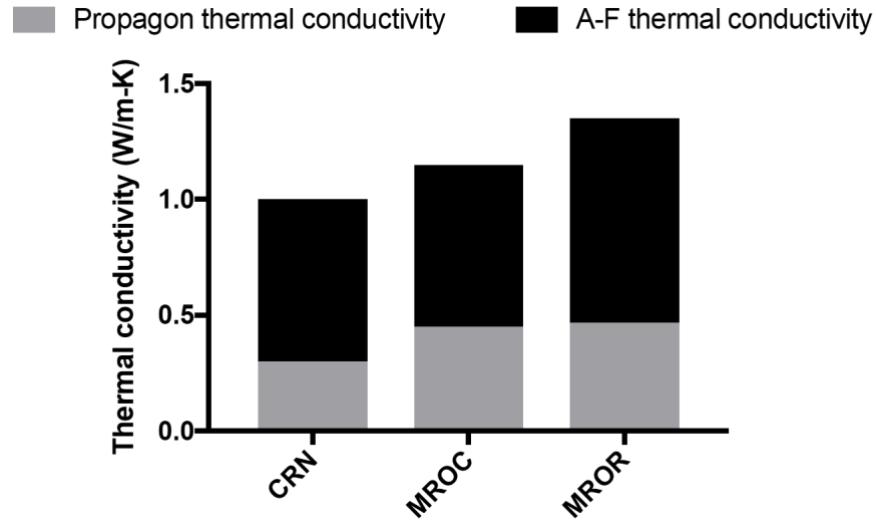


Figure 6 Propagon and A-F thermal conductivity values for the different structures. The propagon thermal conductivity (κ_{pr}) is roughly estimated as $\kappa_{GK} - \kappa_{AF}$.

The propagon thermal conductivity of CRN structure seems to be smaller than the previous study [9] which shows as large as 40 % contribution with the same CRN structure. We believe this difference originates from the different sizes of samples. The propagon thermal conductivity depends on the size of the sample as it limits the number of available propagon modes. In our case, the MRO structures available in the literature [11] are small and we had to use the CRN structures with the same size (3.28 nm) for the direct comparison between the MRO and CRN structures. The previous studies [9, 28] used a relatively large sample with a size of 4.3 nm and the bulk thermal conductivity is extrapolated to the infinitely large sample. Later in this chapter, we will estimate the propagon thermal conductivity for larger systems by extrapolating the lifetime of propagons from the NMD to the long-wavelength limit.

2.4 Vibrational Mode Properties and Analysis

2.4.1 Dynamic Structural Factor

In order to characterize the behavior of vibrational mode, we calculate the dynamic structural factors. The dynamic structural factors are defined as

$$S_{L,T}(\mathbf{k}, \omega) = \sum_{\nu} E_{L,T}(\mathbf{k}, \nu) \delta(\omega - \omega(\mathbf{k} = \mathbf{0}, \nu)) \quad 2-7$$

where the \mathbf{k} is the phonon wavevector, the ω is the frequency and the ν is the phonon branch. The subscript L and T refer to longitudinal and transverse polarizations. The $E_{L,T}$ is

$$E_{L,T}(\mathbf{k}, \nu) = \left| \sum_b u_b^{L,T}(\mathbf{k}, \nu) e^{i\mathbf{k} \cdot \mathbf{r}_b} \right|^2 \quad 2-8$$

where \mathbf{r}_b is the equilibrium position of atom b . The $u_b^{L,T}$ are the longitudinal (L) and transverse (T) components of vibrational eigenvectors defined as $u_b^L = \hat{\mathbf{k}} \cdot \mathbf{e}(\nu, b)$ and $u_b^T = |\hat{\mathbf{k}} \times \mathbf{e}(\nu, b)|$ where $\hat{\mathbf{k}}$ is a unit vector along the longitudinal direction and \mathbf{e} is a vibrational eigenvector. Since a-Si is isotropic, the structural factor is independent of the direction and is calculated in one direction. Also, the maximum wavevector (\mathbf{k}_{\max}) is π/a where a is the lattice constant of crystalline silicon (5.43 Å) and the minimum wavevector is limited by the size of the sample.

The comparisons between the structural factors of the MRO and CRN structures are shown in figure 7 for the two wavevectors representing propagons and diffusons. The small wavevector, $0.34|\mathbf{k}_{\max}|$, corresponds to the frequency of around 1.8 THz and 1.1 THz for longitudinal and transverse polarization respectively. The large wavevector, $0.8|\mathbf{k}_{\max}|$, corresponds to the frequency of around 4 THz and 2.2 THz for longitudinal and transverse polarization respectively. The corresponding frequency is defined as a frequency where the structural factor has a maximum

peak. For the short wavevector representing propagons, the peaks for both longitudinal and transverse structural factors of MRO structures are narrower than the CRN case showing the significant periodic nature of vibrational eigenmodes in those structures. For the large wavevector representing diffusons, however, structural factors of MRO and CRN structures have a similar width. The results clearly indicate the strong dependence of propagon vibrational modes on MRO. The large difference in the structural factors is clearly seen between propagons and diffusons which agrees with previous works. [9, 28]

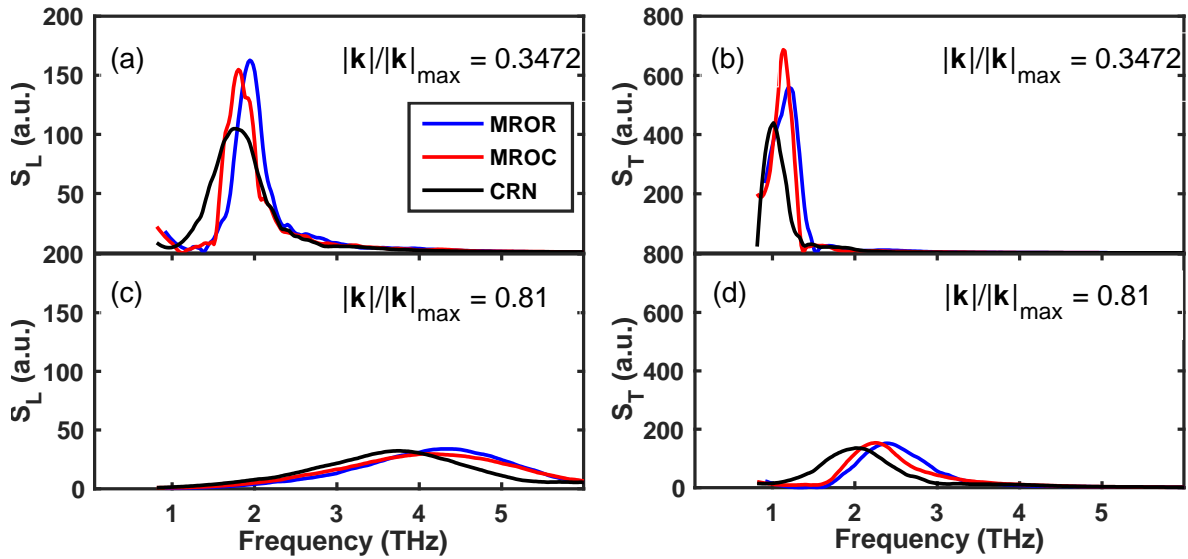


Figure 7 Dynamic structural factor for two wavevectors representing propagon and diffuson: (a) longitudinal and (b) transverse structural factors for propagons and (c) longitudinal and (d) transverse structural factors for diffusons

2.4.2 Calculation of Lifetimes and Thermal Conductivity using Normal Mode

Decomposition

Further, we calculated the lifetimes of vibrational modes for low frequencies below the cutoff frequency (2 THz) using NMD [67] of molecular dynamics (MD) simulation results. We

collected 100,000 snapshots of velocity trajectories in an equilibrium state of NVE simulation which was run over 1 million iterations with a time step of 0.5 fs at 300K. The velocity trajectories of atomic structure are projected onto vibrational modes as follows:

$$\dot{q}(\mathbf{k} = \mathbf{0}, \nu; t) = \sum_{\alpha}^3 \sum_b^n \sqrt{\frac{m_b}{N}} \dot{u}_{\alpha}(b; t) e_{\alpha}^*(\mathbf{k} = \mathbf{0}, \nu; b) e^{i(\mathbf{k}=\mathbf{0}) \cdot \mathbf{r}_b} \quad 2-9$$

where \dot{u}_{α} is the α component of the atomic velocity. Then we calculate the spectral energy of each vibrational mode by integrating over the simulation time. The spectral energy is calculated as

$$\Phi(\nu, \omega) = \frac{1}{4\pi\tau_0} \left| \int_0^{\tau_0} \dot{q}(\nu; t) e^{-i\omega t} dt \right|^2 \quad 2-10$$

where τ_0 is the simulation time. The lifetime of vibrational mode can be found by fitting the spectral energy with the Lorentzian function in the following form

$$\Phi(\nu, \omega) = \frac{C_0(\nu)}{[\omega_0(\nu) - \omega]^2 + \Gamma^2(\nu)} \quad 2-11$$

where $C_0(\nu)$ is a constant value. The $\Gamma(\nu)$ has a relation with the lifetime as follows:

$$\tau(\nu) = \frac{1}{2\Gamma(\nu)}. \quad 2-12$$

We extrapolate the lifetime of propagons to the long-wavelength limit in order to calculate the propagon thermal conductivity for an infinitely large a-Si sample. The rough estimation of propagon thermal conductivity using $\kappa_{\text{GK}} - \kappa_{\text{AF}}$ does not include the contributions from propagons with wavelengths larger than the sample size (3.28 nm). We extrapolate the lifetime using the widely assumed ω^{-2} and ω^{-3} dependences of phonon lifetime below 2 THz:

$$\tau(\omega) = B\omega^{-n}$$

where B is a constant and n is a scaling exponent i.e., 2 or 3 [5, 9, 34, 50]. The fitting was performed using the least square of error method. The lifetime as well as the fitted line are compared in figure 8.

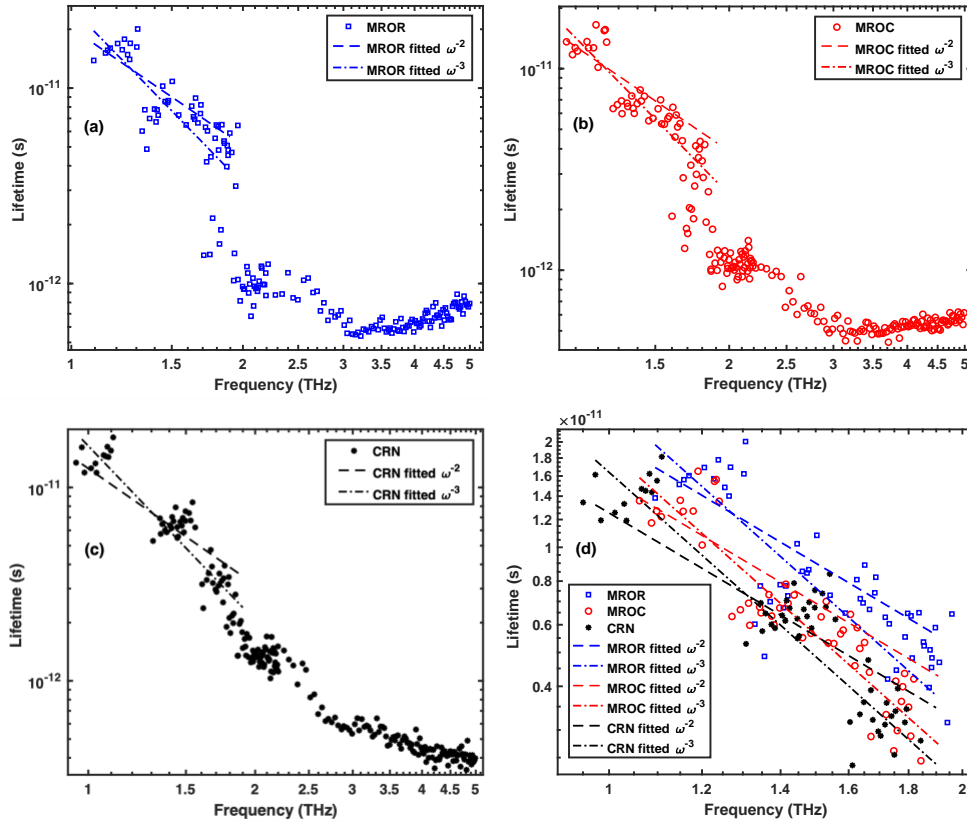


Figure 8 Lifetimes and fitted lines for (a) MROR (b) MROC (c) CRN structures and (d) the zoom-in comparison of three structures in the propagon frequency range.

In Table 1, we show the fitting constant (B) for three different structures. The fitting constant B assuming ω^{-2} dependence for CRN structure agrees well with that reported in the previous study assuming the same structure and ω^{-2} dependence. [9] The B for MRO structures are considerably larger than the CRN structure which lead to longer lifetime and mean free path of propagon.

Table 1 Fitting of propagon lifetimes (B in THz²-s for ω^{-2} and THz³-s for ω^{-3})

	ω^{-2}	ω^{-3}
CRN	1.2×10^{-11}	1.6×10^{-11}
MROC	1.5×10^{-11}	1.9×10^{-11}
MROR	2.0×10^{-11}	2.6×10^{-11}

The propagon thermal conductivity for an infinitely large sample is then calculated as

$$\begin{aligned}
 \kappa_{\text{pr}} &= \frac{1}{3\Omega} \int_0^{\omega_{\text{cut}}} DOS_{\text{L}}(\omega) C(\omega) v_{\text{L}}^2 \tau(\omega) d\omega \\
 &+ \frac{2}{3\Omega} \int_0^{\omega_{\text{cut}}} DOS_{\text{T}}(\omega) C(\omega) v_{\text{T}}^2 \tau(\omega) d\omega
 \end{aligned} \tag{2-14}$$

where $DOS_{\text{L,T}}(\omega)$ is the DOS based on the 3D Debye model and is given as $\Omega\omega^2/2\pi^2v_{\text{L,T}}^3$. The $C(\omega)$ is the heat capacity and $v_{\text{L,T}}$ are the longitudinal and transverse group velocities. Here the group velocities are obtained from the structural factors at low frequency. Based on our dynamic structural factors calculation, all three structures have similar group velocities; the transverse (v_{T}) and longitudinal (v_{L}) group velocities are about 3620 m/s and 7240 with a variance of 1 %. The group velocity values are in close agreement with the previous work [9] for CRN. It is worth mentioning that the thermal conductivity would diverge when the ω^{-3} dependence is assumed. In this case, to bound the thermal conductivity, we consider a boundary scattering based on the largest experimental sample which has the thickness (t_{B}) of 80 μm . [34] Hence the lifetime is estimated following the simple model for boundary scattering rate which is combined with the intrinsic scattering rate through the Matthiessen rule [68]

$$\frac{1}{\tau_{\text{eff}}} = \frac{1}{\tau_{\text{bulk}}} + \frac{2v_s}{t_B} \quad 2-15$$

In figure 9, based on the extrapolation, we calculate the propagon thermal conductivity values for each structure including contributions from propagons with long wavelengths. When the propagon lifetime is assumed to follow ω^{-2} dependence, the propagon thermal conductivities are 1.49 and 1.14 W/m-K for MROR and MROC, respectively, which show 116 and 65 % larger than that of CRN structure. If the ω^{-3} dependence is assumed, the propagon thermal conductivity values are 2.87 and 2.19 W/m-K for MROR and MROC, respectively, which are 117 and 66 % larger than that of the CRN structure. For both MRO structures, the predictions indicate that 63 and 77 % of total thermal conductivity is contributed from propagons when the propagon lifetime is assumed to follow ω^{-2} and ω^{-3} , respectively. The predicted values clearly show a more pronounced contribution of propagon in MRO structures.

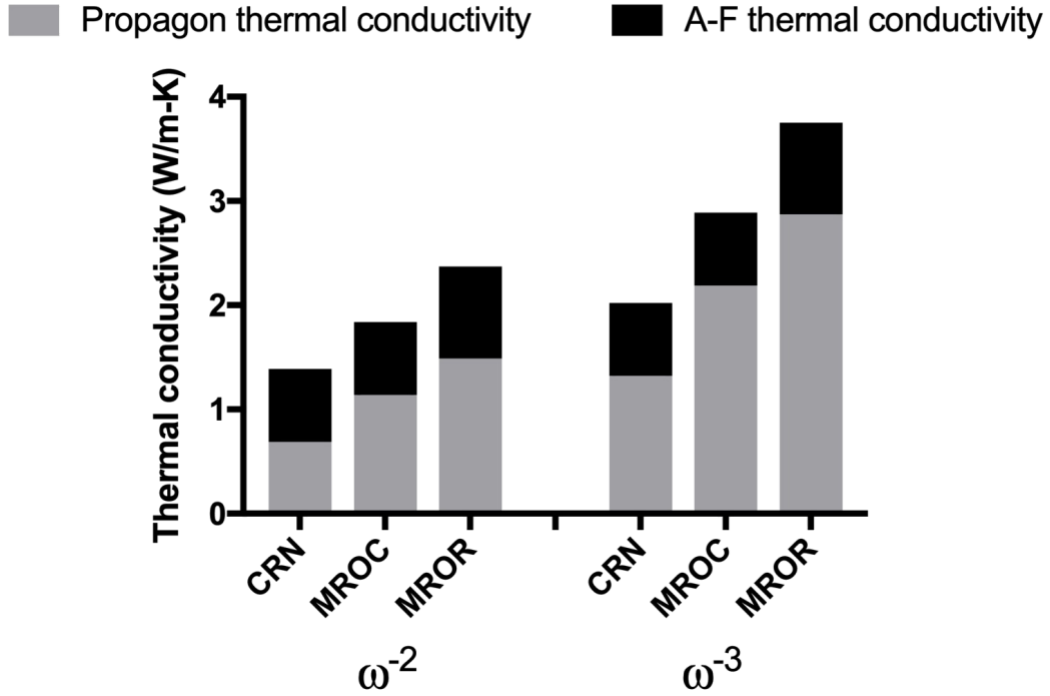


Figure 9 Propagon and A-F thermal conductivity values for the different structures. The propagon thermal conductivity is predicted by extrapolating the lifetime of propagons to low frequency limit using NMD. The left and right figures assume the ω^{-2} and ω^{-3}

2.5 Summary

We have discussed the dependence of thermal conductivity on MRO. We showed two atomistic structures for amorphous silicon with MRO. We confirmed the presence of MRO using dihedral angle distribution and FEM simulation in those two structures. The results show the presence of structural order in the medium range of 10 to 20 Å. The rough estimation of κ_{pr} using the G-K and A-F thermal conductivities for a small system with a size of 3.28 nm show that κ_{pr} of MRO structures are 50 % larger than that of CRN structure. We also compared the propagons in MRO and CRN structures using the structure factor and the lifetime of propagons from NMD

of MD simulation data, showing the noticeably longer lifetimes of propagons for MRO structures. Then, the κ_{pr} was calculated for a larger system by extrapolating the lifetime of propagons to the infinite wavelength limit. The κ_{pr} is up to 117 % larger in MRO structures compared to the CRN structure. Our study provides evidence of a strong correlation between MRO and propagon thermal conductivity. This has an important implication for understanding and manipulating thermal transport in a-Si. The MRO often depends on the synthesis methods and post-annealing processes [11, 12] and thus the thermal conductivity of a-Si is expected to also depend on those conditions. Our study may explain the large thermal conductivity of a-Si that had been reported previously [5-8, 34] while conclusive determination of the influence of MRO on measurements of thermal conductivity requires a side-by-side structural analysis of experimental samples. Our work may prompt the future experimental studies in that direction.

3.0 Graphene Grain Boundary, Atomistic Green's Function, and Transport Properties

3.1 Grain Boundary Structure

In order to create structures with periodic boundary conditions, we constructed structures containing two identical grain boundaries (GBs) which are placed in the inversed direction with respect to each other. Therefore, we maintain the periodic boundary conditions along with both parallel and perpendicular directions to the GB direction, as shown in figure 10.

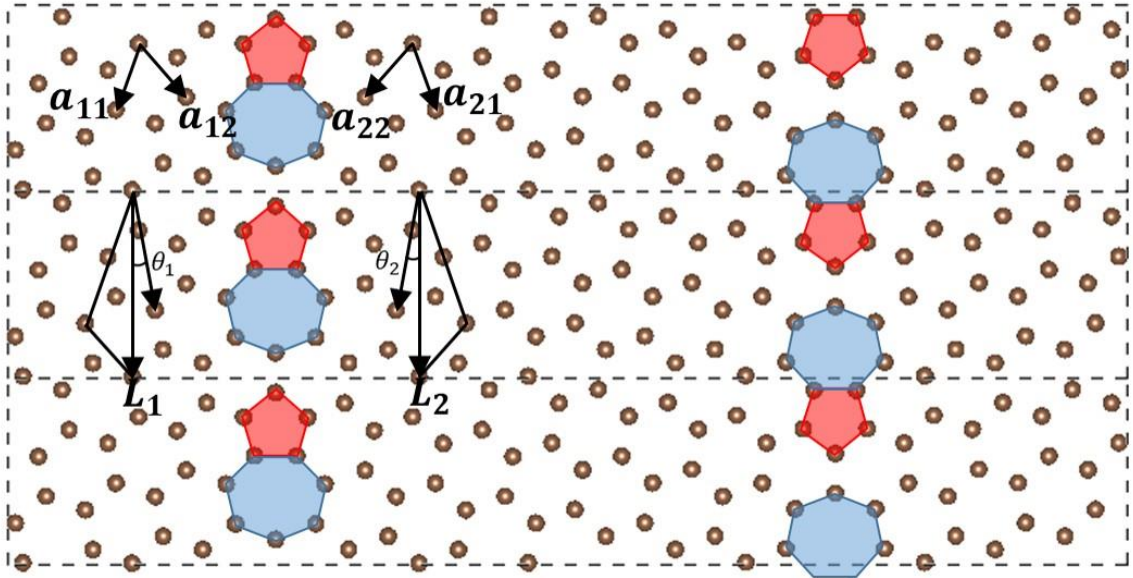


Figure 10 A typical structure containing two identical GBs with periodic boundary conditions along both the directions parallel and perpendicular to the GB direction. Each rectangle formed by the dashed line represents one unit cell. The lattice vectors of the two grains forming the GB are (a_{i1}, a_{i2}) , with $i=1, 2$ for grains 1 and 2, respectively. The tilt angle between the chiral vector $L_i = n_{i1}a_{i1} + n_{i2}a_{i2}$ and the lattice vector along the armchair direction a_{i2} is θ_i . The GB is characterized by the misorientation angle $\theta_M = \theta_1 + \theta_2$ and the boundary line angle $\theta_L = |\theta_1 - \theta_2|$.

We first construct a single GB (the left one in figure 10) which is periodic along the GB direction and nonperiodic along the perpendicular direction. The lattice vectors of the two grains forming the GB are $(\mathbf{a}_{i1}, \mathbf{a}_{i2})$, with $i = 1, 2$ for grains 1 and 2, respectively and the lattice constant is a . The tilt angle (θ_i) is defined as angle between the chiral vector $\mathbf{L}_i = n_{i1}\mathbf{a}_{i1} + n_{i2}\mathbf{a}_{i2}$ and the lattice vector \mathbf{a}_{i2} along the armchair direction. The GB (of any two-dimensional material) is characterized by the misorientation angle defined as $\theta_M = \theta_1 + \theta_2$ and the boundary line angle defined as $\theta_L = |\theta_1 - \theta_2|$. The symmetries of graphene lattice result in θ_M varying from 0° to 60° , and θ_L from 0° to θ_M . [69]

For each grain i , the length of the chiral vector $|\mathbf{L}_i| = a\sqrt{(n_{i1}^2 + n_{i2}^2 + n_{i1}n_{i2})}$ is defined as the periodic repeating unit length along the GB direction, where n_{i1}, n_{i2} are integer numbers such that $\tan \theta_i = (n_{i1} - n_{i2})/\sqrt{3}(n_{i1} + n_{i2})$. To form a GB, $|\mathbf{L}_i|$ of the corresponding two grains should be commensurate, i.e., $|\mathbf{L}_1|/|\mathbf{L}_2| = p/q$, where p, q are positive integers, in which case the GB length is $l_{GB} = q|\mathbf{L}_1| = p|\mathbf{L}_2|$. In this work, we consider only high symmetric GBs with $\theta_1 = \theta_2$, for which the GB length of the unit cell is $|\mathbf{L}_1| = |\mathbf{L}_2|$.

After constructing a single GB supercell (named A), we rotate it by 180° to build the GB supercell named B. Then, we merge the two supercells A and B to construct a periodic structure along the direction perpendicular to the GB direction by shifting B to match the hexagonal rings at the right boundary of A and left boundary of B, and then removing the superposition atoms, as illustrated in figure 11.

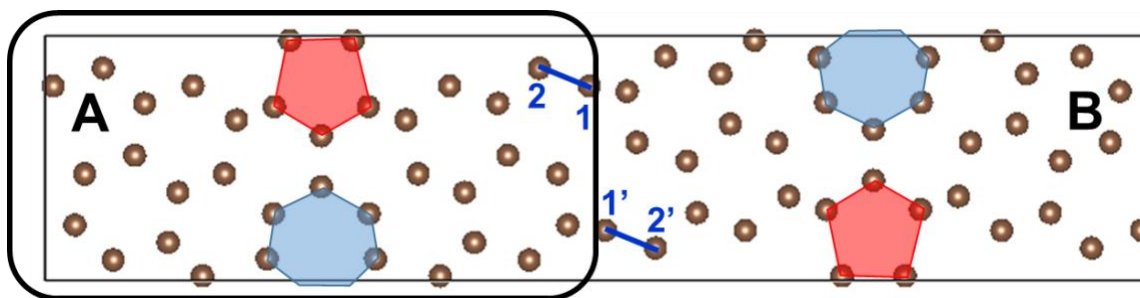


Figure 11 Constructing a supercell by matching the hexagonal rings at the right boundary of A and left boundary of B. The atoms 1 and 2 are labeled by 1' and 2' after rotating A by 180°. The periodic structure is constructed by shifting B so that the atom 1' over

3.2 Machine Learning Interatomic Potential

Density functional theory (DFT) simulations are widely considered a high-fidelity simulation method in the materials science and solid-state physics. The DFT has shown high accuracy for many-body systems, atoms, molecules, and electronic structure modeling. However, DFT simulations are computationally expensive and its scalability is unfavorable; the computational cost increases as $\sim O(N^3)$ where N is the total number of electrons in a system. For years, empirical interatomic potentials have been used to do classical MD simulations for large atomistic structures and in a variety of problems. The empirical potentials are analytical formulations which are mostly interpolated from DFT calculations. They are computationally cheaper and thus can be useful for large scale simulations. However, there are two major issues with empirical potentials: a) conventionally they have rigid functional form that limits their applicability to the limited number of applications or properties b) a good agreement may be related to the fortitude cancellation of the embedded errors [70]. Machine learning interatomic

potentials (MLIPs) have emerged as an alternative to overcome the aforementioned problems [71, 72]. They do not require rigid functional forms and thus can describe multiple phases with an accuracy comparable to ab initio calculations, while the cost is much cheaper than the density functional theory (DFT) calculations. MLIPs have been shown to successfully describe properties of materials with an accuracy of ~ 1 meV/atom for energy [70-84]. Notably, several previous studies showed that MLIPs can have higher accuracy and reproduce correct harmonic force constants for the crystalline phase [20,22,24,32]. MLIP often has a tradeoff of the transferability and accuracy [70] which are both necessary for thermal transport calculation. A large set of input training data enforces the interpolation to be dominant which diminishes the transferability, or in other words extrapolations. Hence, we believe focusing on grain boundary structures of two-dimensional materials, such as graphene, yields a good balance for an MLIP with good transferability and high accuracy. Additionally, to our best knowledge, the MLIPs have not been examined for thermal transport of interfacial materials such as grain boundary structures. The structures of grain boundaries are widely varied and they show some uncertainty upon the buckling. Here, we demonstrate that the Gaussian approximation potential (GAP) [20], which is a type of MLIP, has high accuracy and flexibility to describe interatomic interactions with a DFT accuracy for a large set of grain boundary structures of graphene.

3.2.1 Gaussian Approximation Potential

Here I provide a summary of the GAP developed by [85-87]. Our goal is to develop a machine-learning potential based on the data from density functional theory calculations. The GAP method has two major components. First, a set of descriptors for the atomistic structure is developed so that (1) it satisfies the translation, rotation, and permutation invariances, and (2) the

atomistic structures are captured precisely while the high-dimensional atomic position data are mapped onto relatively low dimensional space. Second, the mapping between environments and the target quantities such as atomic energies and forces is done by a kernel which is associated with the similarity of environments. We use the smooth overlap of atomic positions (SOAP) [87]. One advantage of GAP is that the training is performed using simple linear algebra rather than iterative nonlinear optimization of a multimodal function, as in the case of neural networks.

The interatomic potential is a relatively high dimensional function to accurately describe the energy and forces of any given atom. In GAP, the high dimensional interatomic potential is divided into purely repulsive and attractive potential descriptors. The repulsive pair potential descriptors are pre-defined/pre-calculated interaction of a pair of atoms using DFT results with cubic spline fitting. The attractive potential descriptor is a many-body kernel fit. Therefore, the total GAP model energy for a system is the linear combination of the repulsive and attractive descriptors as follows

$$E = \sum_{i < j} V^{(2)}(r_{ij}) + \sum_i \sum_s^M \alpha_s K(\mathcal{R}_i, \mathcal{R}_s) \quad 3-1$$

where i and j are the atomic indices, $V^{(2)}$ is the repulsive pair potential, r_{ij} is the distance between any pair of atoms, K and \mathcal{R}_i are kernel basis function and the collection of relative position vectors, also known as neighborhood, respectively. The first term is the predefined function in the GAP library. The second term is quantified by the similarity of neighboring pairs of atoms. Here, the objective is to pick a set of dissimilar pairs that captures the most variation of the energy field. To this point, neighbor density is calculated using the SOAP kernel as

$$\rho_i(\mathbf{r}) = \sum_{i'} f_{\text{cut}}(r_{ii'}) e^{-(\mathbf{r}-\mathbf{r}_{ii'})/2\sigma_{\text{atom}}^2} \quad 3-2$$

where the summation is the decaying functions to zero over the neighbors i' of atom i , f_{cut} and σ_{atom} are a cutoff function and smearing parameter respectively. Then the SOAP kernel of two neighbor environments is calculated over all possible 3D rotation, SO(3) rotation group [87], of two neighbor density as

$$\tilde{K}(\mathcal{R}_i, \mathcal{R}_j) = \int_{\hat{R} \in \text{SO}(3)} d\hat{R} \left| \int d\mathbf{r} \rho_i(\mathbf{r}) \rho_j(\hat{R}\mathbf{r}) \right|^2 \quad 3-3$$

and after normalization and raising to an integer power, the final kernel is calculated as:

$$K(\mathcal{R}_i, \mathcal{R}_j) = \delta^2 \left| \frac{\tilde{K}(\mathcal{R}_i, \mathcal{R}_j)}{\tilde{K}(\mathcal{R}_i, \mathcal{R}_i) \tilde{K}(\mathcal{R}_j, \mathcal{R}_j)} \right|^\zeta \quad 3-4$$

here δ is the hyperparameter corresponding to the energy scale of the many-body potential.

Practically to calculate the integral (Eq. 3-3), we expand the integral to a summation of the basis in a spherical harmonic space. Thus, the density function is given as

$$\rho_i(\mathbf{r}) = \sum_{nlm} c_{nlm}^i Y_{lm}(\hat{\mathbf{r}}) g_n(r) \quad 3-5$$

where Y_{lm} are the spherical harmonics, g_n are the radial functions, which are equispaced Gaussian functions, and c_{nlm}^i are the spectral coefficients on spherical space. The indices i , n , l , and m are atomic number, radial index, the coordinate, and spectral indices. Since the descriptors are unique rotationally and permutationally invariant of the neighbor environment, we can write the following spherical power spectrum vector:

$$\begin{aligned} \tilde{\mathbf{p}}_{n'nl}^i &= \sum_{m=-l}^l c_{nlm}^{i*} c_{n'tm}^i \\ \mathbf{p}^i &= \tilde{\mathbf{p}}^i / |\tilde{\mathbf{p}}^i| \end{aligned} \quad 3-6$$

If we use this notation, the SOAP kernel can be written as the scalar product of the above relation as:

$$K(\mathcal{R}_i, \mathcal{R}_j) = \delta^2 |\mathbf{p}^i \cdot \mathbf{p}^j|^\zeta \quad 3-7$$

Practically the SOAP kernel is then used in Eq. 3-1 in order to calculate the coefficients, α_s , in a linear system. This sums up the novelty of GAP to compare with other MLIPs where the many-body potential is projected into an infinite spectrum of spherical harmonics that yield the full description of the many-body interactions. Since the descriptors are defined in spherical space, they preserve the complete rotational invariance that eventually decreases the number of environments and configurations required to train the potential. However, since the representative set is infinite in an ideal case, a matrix reconstruction technique, known as CUR [88], is used to find the most important subset of the SOAP kernels. Therefore, the kernel calculations are reduced to a linear system with finite size and straight-forward formalism to calculate the spectrum coefficient is given by [89, 90] as:

$$\alpha^* = [\mathbf{K}_{MM} + (\mathbf{L}\mathbf{K}_{NM})^T \Lambda^{-1} \mathbf{L}\mathbf{K}_{NM}]^{-1} (\mathbf{L}\mathbf{K}_{NM})^T \Lambda^{-1} \mathbf{y} \quad 3-8$$

where \mathbf{K}_{MM} is the kernel matrix corresponding to the M reduced representative atomic environment, and \mathbf{L} is the linear differential operator of size $N \times D$ where N and D are the number of atoms from the input and the number of input data respectively, \mathbf{y} is the vector containing all the input data such as energies, forces, and virial stress components and lastly Λ^{-1} is the diagonal matrix where the elements represent the empirical weights of the input data values. More details about the details of GAP and input parameters can be found in Ref. [70].

3.3 Landauer Formula and Ballistic Transport

Landauer formula was first introduced to find the electron conductance in nanoscale junction based on the wave scattering. The formula also has been widely applied to predict phonon

transport and thermal transport in the ballistic regime. The ballistic regime is the regime in which the size of the system is considerably smaller than the mean free path of phonons. For a lattice model with the harmonic interaction, the scattering process is purely elastic with no energy loss and the Landauer formula is well suited to measure the thermal transport in this regime. For a junction with two heat baths when the heat flow transport is from left to right, the Landauer formula is given as

$$I = \int_0^{\infty} \frac{\hbar\omega}{2\pi} T(\omega) (f_L - f_R) d\omega \quad 3-9$$

where $f_{L/R} = \frac{1}{\exp\left(\frac{\hbar\omega}{k_B T_{L/R}}\right)}$ is the Bose-Einstein phonon distribution and $T(\omega)$ is called the transmission function or transmittance. We should note that the transmission function is independent of temperature and only the distribution function is temperature-dependent.

Thermal conductance is defined as

$$G = \lim_{T_L \rightarrow T, T_R \rightarrow T} \frac{I}{T_L - T_R} \quad 3-10$$

As we mentioned earlier, this relation gives the thermal conductance of ballistic thermal transport when the dissipation is minimal. Furthermore, the thermal conductivity is defined as $\kappa = GL/S$ where L and S are the length and cross-sectional area of the system respectively. In many thermal transport experiments/applications, the cross-sectional area is not well defined and, thus, it is better to measure thermal conductance.

In this chapter, we aim to calculate a transmission function using Green's function approach in particular for the set of problems where the thermal resistance occurs at interfaces. In the next sections, we will introduce AGF for thermal transport in interfacial materials and derive the transmission function based on the Landauer formula.

3.4 Atomistic Green's Function

3.4.1 What is Green's Function?

Mathematically Green's function is defined as an inverse of the differential operation in a linear dynamical system. Green's function is also known as the response function. Let's consider that the linear dynamical system is given as

$$Lu(x) = f(x) \tag{3-11}$$

where the L is a linear differential operator and $u(x)$ is the system's response. For a system with linear response upon given source $f(x)$, the response can be represented by responses upon many unit impulses. Thus, the dynamical equation for a unit impulse can be written as

$$LG(x, r) = \delta(x - r) \tag{3-12}$$

where $G(x, r)$ is Green's function of the linear operator L . In the above equation, $G(x, r)$ represents the system's response at location x upon the unit impulse which is applied at location r . Hence the solution of Eq. 3-11 at any location, $u(x)$, is

$$u(x) = \int G(x, r)f(r)dr \tag{3-13}$$

here the integration over the unitary responses results in the total response of the system.

The solution for Green's function may not be unique due to the complexity and non-linearity of the L kernel. Based on the symmetry assumption and the certain boundary conditions, the solution can be uniquely calculated for the Green's function. As a result, there are two common solutions for Green's function which are known as retarded and self-advance. These solutions are dependent on the choice of boundary conditions. The boundary conditions for retarded and self-advance Green's function are given as [91]

$$G^{\text{retarded}}(r, r) = 1 \tag{3-14}$$

$$G^{\text{retarded}}(\pm\infty, r) = 0$$

$$G^{\text{self-advance}}(r, r) = 1$$

$$G^{\text{self-advance}}(\pm\infty, r) = \infty$$

since the boundary conditions of the retarded Green's function are bounded, then the solution is possible. Therefore, hereafter, when we discuss Green's function, we refer to retarded Green's function. If the solutions for retarded and self-advance are well-posed, then they are the adjoint matrix of each other which means that the retarded solution can be mapped and transformed to the self-advance solution.

The physical interpretation of the Green's function is that it describes a response function which is propagating upon unit excitation at a specific location. The Green's function waves are similar to the water ripple and can be propagated in all directions symmetrically. For a retarded solution, the excitation is formed as a decaying propagation while for the self-advance solution is formed as a growing propagation. The physical interpretation of the Green's functions in one dimension is shown in figure 12. The solution waves for the retarded Green's function are propagating outward to the source location while the solution waves of self-advance are moving toward the source location.

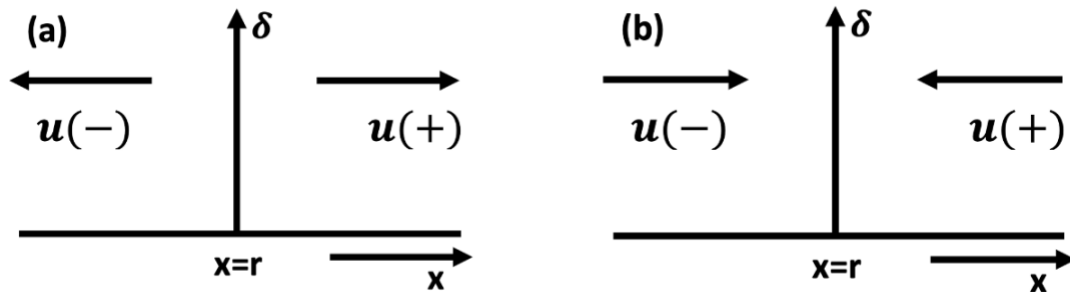


Figure 12 The excitation propagation of (a) retarded Green's function and (b) self-advance Green's functions

3.4.2 Dynamical System of Equations for a Harmonic System

Based on the Newtonian mechanics, the dynamical system for the atomistic vibration is described by the equation of motion of each atom

$$F_i = M_i \frac{d^2 u_i}{dt^2} = - \frac{\partial E}{\partial u_i} \quad 3-15$$

where the u_i is the displacement, M_i is the mass and F_i is the interacting force on atom i . The dynamical system represents the time-dependent evolution or trajectory of the atomic displacement in space. The potential landscape around atoms is described by its Taylor series about small atomic displacement

$$E = E_0 + \sum_i F_i u_i + \frac{1}{2} \sum_{i,j} \frac{\partial^2 E}{\partial u_i \partial u_j} u_i u_j + H.O \quad 3-16$$

here E_0 is the energy at the equilibrium position. The second term would be canceled since the summation of interacting forces on the equilibrium state is zero. Also in order to linearize the dynamical system and seize the calculation to the harmonic properties, the high order terms of Taylor expansion are dismissed. The shortened expansion of the Taylor series of energy is

$$E = E_0 + \frac{1}{2} \sum_{i,j} \phi_{ij} u_i u_j \quad 3-17$$

where the $\phi_{ij} = \frac{\partial^2 E}{\partial u_i \partial u_j}$ is the second-order force constant between two atoms of i and j . Then, Eq.

3-15 can be expressed using the second-order force constant

$$F_i = M_i \frac{d^2 u_i}{dt^2} = - \sum_j \phi_{ij} u_j \quad 3-18$$

Now to solve the dynamical equations (Eq. 3-17), we would substitute the wavefunction solution to reformulate the Eq. 3-17. The wavefunction solution is given as

$$u_j = \frac{\bar{u}_j}{\sqrt{M_j}} \exp(i\omega t) \quad 3-19$$

where \bar{u}_j is the wavefunctions. When we substitute the given solution into the Eq. 3-18, we get an eigenvalue problem that contains a set of independent frequencies and wavefunctions

$$\omega^2 \bar{u}_i = - \sum_j \phi_{ij} \frac{\bar{u}_j}{\sqrt{M_i M_j}} \quad 3-20$$

To simplify this equation, we stack the wavefunctions into a vector, force constants, and masses into matrices, hence we get

$$(\omega^2 \mathbf{I} - H) \bar{\mathbf{u}} = 0, \quad H = \frac{\Phi}{M} \quad 3-21$$

where H is the Hamiltonian matrix that its elements are force constants over effective masses of the atomistic structure. The wavefunctions are the shape functions of the solution. The multiplier of the wavefunctions ($\bar{\mathbf{u}}$) is an operator for the dynamical system, $L = (\omega^2 \mathbf{I} - H)$. As it was mention in the previous section, Green's function is namely the inverse of this operator, thus

$$G = (\omega^2 \mathbf{I} - H)^{-1} \quad 3-22$$

If the operator matrix is invertible then the Green's function calculation is rather trivial. However, mostly the operator is not well-posed. Also, the size of the operator matrix can be infinitely large if we assume an infinitely large crystal. In this chapter, we focus on the Green's function for an interface between two bulk samples that are semi-infinite, and thus our operator matrix size is semi-infinite. In the following section, we discuss atomistic Green's function (AGF) for an interface.

3.4.3 Atomistic Green's Function for a Decoupled Device with Two Contacts

Here I provide a summary of the atomistic Green's function method that was developed by [18, 91, 92]. We consider a system where two bulk materials share a physical interface. This system

can be decomposed of a bulk portion of two materials and an interface region sandwiched by the two materials. The interface region is called the device and the bulk portions are semi-infinitely large contacts that are coupled to the device. The schematic view of the system is shown in figure 13.

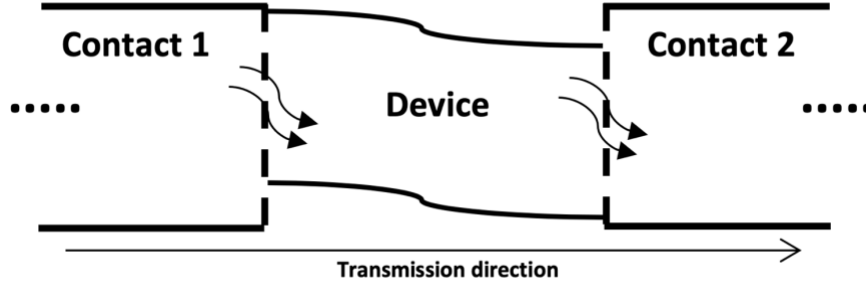


Figure 13 schematic view of the device with two semi-infinte contacts. Transmission direction is assumed to be left to right (from contact 1 to contact 2)

In many thermal transport applications, the goal is to calculate the conductance or resistance in the device. The device contains atomistic structures that differ from those of the bulk portion of materials, such as point defects, grain boundaries, etc. Here we begin from the Eq. 3-21 in order to develop the dynamical equations that will be used to find the thermal transport in the device. The coupled dynamical equation of the device with two contacts can be written as the following:

$$\omega^2 \mathbf{I} \begin{Bmatrix} \bar{u}_1 \\ \bar{u}_d \\ \bar{u}_2 \end{Bmatrix} = \begin{bmatrix} H_1 & \tau_1^\dagger & 0 \\ \tau_1 & H_d & \tau_2 \\ 0 & \tau_2^\dagger & H_2 \end{bmatrix} \begin{Bmatrix} \bar{u}_1 \\ \bar{u}_d \\ \bar{u}_2 \end{Bmatrix} \quad 3-23$$

where the \bar{u} is the wavefunctions, H is the Hamiltonian matrix and τ is the coupling Hamiltonian submatrix. The subscripts d, 1, and 2 represent the device, left contact, and right contact, respectively. The contacts are periodic and semi-infinitely large, therefore the Hamiltonian matrices of H_1 and H_2 have a semi-infinitely large size in two dimensions. However, τ_1 and τ_2

have an infinitely large size in a dimension align with one of the contacts and a finite size in a dimension aligns with the device. The current system of equation is infinitely large and inverse calculation of the matrix (i.e., Green's function) is not trivial.

To find the Green's function of the device, we first need to curtail the contact solution. Here the idea is to deal with the device portion in such a way that the influence of contacts would be imposed as boundary conditions on the device. In this way, the influence of two periodic contacts could be calculated and added to the device as some input boundary conditions. Then, we can solve the dynamical equation for the device only, which has a finite size.

The Hamiltonian system of Eq. 3-23 can be written with the wavefunctions of the contacts which are divided into the isolated portion (\bar{u}^i) representing the bulk solution of periodic contact and the reflected portion (\bar{u}^r) representing the change due to the coupling interface:

$$\begin{aligned} & \begin{bmatrix} (\omega^2 + i\eta)I - H_1 & -\tau_1^\dagger & 0 \\ -\tau_1 & \omega^2 I - H_d & -\tau_2 \\ 0 & -\tau_2^\dagger & (\omega^2 + i\eta)I - H_2 \end{bmatrix} \begin{Bmatrix} \bar{u}_1^i + \bar{u}_1^r \\ \bar{u}_d \\ \bar{u}_2^i + \bar{u}_2^r \end{Bmatrix} \\ & = \begin{Bmatrix} S_1 \\ 0 \\ S_2 \end{Bmatrix} \end{aligned} \quad 3-24$$

here $(\omega^2 + i\eta)$ is a perturbed frequency and we consider η as a perturbation to the frequency with a small positive value. Note that we imposed sources on the left and right contacts represented by S_1 and S_2 to equalize the equations upon added perturbation to the system. Both sources and wavefunctions are unknown at this point, but there are relations between sources and isolated wavefunctions which we will use to solve Eq. 3-24. In an ideal case without any perturbation, the Hamiltonian system of the isolated contacts would yield the periodic solution for an infinitely large contact. In order to solve the system of Eq. 3-24, we make two assumptions concerning

perturbation: first is that the perturbation is a positive value which leads to the retarded Green's function solution, and secondly perturbation is small enough that the dynamical system remains fully linear.

The contact Green's function known as decoupled Green's function or bulk Green's function is defined as $g_1 = ((\omega^2 + i\eta)I - H_1)^{-1}$, representing the Green's function of an isolated (decoupled) and infinitely large bulk contact 1. The damping term, $i\eta$, is related to the source term through $((\omega^2 + i\eta)I - H_1)\bar{u}_1^i = S_1$ for the isolated contact 1. Similarly using the bulk Green's function of the contact 2, $g_2 = ((\omega^2 + i\eta)I - H_2)^{-1}$ and $((\omega^2 + i\eta)I - H_2)\bar{u}_2^i = S_2$. Then, Eq. 3-24 can be simplified as follows:

$$\begin{aligned} g_1^{-1}\bar{u}_1^r - \tau_1^\dagger\bar{u}_d &= 0 \\ (\omega^2 I - H_d)\bar{u}_d - \tau_1(\bar{u}_1^i + \bar{u}_1^r) - \tau_2(\bar{u}_2^i + \bar{u}_2^r) &= 0 \\ g_2^{-1}\bar{u}_2^r - \tau_2^\dagger\bar{u}_d &= 0 \end{aligned} \quad 3-25$$

The Eq. 3-25 is simplified using the reflected wavefunctions of contact 1 ($\bar{u}_1^r = g_1\tau_1^\dagger\bar{u}_d$) and contact 2 ($\bar{u}_2^r = g_2\tau_2^\dagger\bar{u}_d$) as follows:

$$(\omega^2 I - H_d - \tau_1 g_1 \tau_1^\dagger - \tau_2 g_2 \tau_2^\dagger)\bar{u}_d = (\tau_1 \bar{u}_1^i + \tau_2 \bar{u}_2^i) \quad 3-26$$

the right-hand side is considered a source term for dynamical behavior of the device, $S = \tau_1 \bar{u}_1^i + \tau_2 \bar{u}_2^i$. Finally, the Green's function for the device which is known as coupled Green's function is expressed as follows:

$$G_d = (\omega^2 I - H_d - \Sigma_1 - \Sigma_2)^{-1} \quad 3-27$$

where Σ_1 and Σ_2 are $\tau_1 g_1 \tau_1^\dagger$ and $\tau_2 g_2 \tau_2^\dagger$, respectively, and they are called self-energy. In essence, the self-energy terms represent the change of device Hamiltonian due to the coupling with contacts. These boundary conditions include the coupling terms which show the strength of coupling interaction between the device and contacts as well as the bulk Green's function. Next

section, we will discuss the physical interpretation of the Green's function and the computational techniques to calculate the bulk and surface Green's function.

3.4.4 Surface Green's Function

Surface Green's function is what curtails the infinitely large bulk Green's function to finite size and an invertible portion of Green's function that captures the decay of response. This allows us to limit the size of Hamiltonian matrices that are defined in the previous section. Here we use periodicity and decaying aspects of the bulk Green's function to solve or approximate the bulk Green's function. Since the retarded Green's functions decays and contact is periodic, the bulk Green's function can be divided into an unlimited number of finite size matrices representing a bulk contact and a finite size matrix representing a portion close to the device. The latter portion of Green's function is called surface Green's function. Surface Green's function is a sufficient estimation of the bulk Green's function of contact to calculate the self-energies. In the next sections, we will discuss the ways to calculate the surface Green's function both analytically and numerically.

3.4.4.1 Analytical Approach to Solve Surface Green's Function

The main idea for finding surface Green's function in both analytical and numerical approaches is to use the invertibility of submatrices. If an infinitely large operator matrix is simplified as [91]

$$L_c = \begin{pmatrix} A & C \\ B & D \end{pmatrix} \quad 3-28$$

where A , B , C , and D are submatrices. For left contact as an example, only D considered having a finite size which resembles the surface Green's function and the rest is infinitely large. Here we assume that the submatrix of D is large enough that it includes all the dynamical interaction with the device. Hence the submatrix A solely represents the bulk portion of the set of force constants. It is easy to find the inverse of submatrix A due to periodicity. Also, from linear algebra, the following relation holds for the Eq. 3-28

$$g_b = (L_c)^{-1} = \begin{pmatrix} \dots & \dots \\ \dots & (D - CA^{-1}B)^{-1} \end{pmatrix}. \quad 3-29$$

In Eq. 3-21 the submatrix A represents a periodic portion of bulk and thus can be inverted. If we implement this formulation for the surface Green's function of left contact, then the generic formulation for surface Green's function is

$$g_L = (D - CA^{-1}B)^{-1}. \quad 3-30$$

Even though this analytical solution is simple, the inverse of matrix A can be non-trivial or computationally expensive. This motivates the decimation technique for the solution of the surface Green's function which is discussed in the following section.

3.4.4.2 Decimation Technique to Solve Surface Green's Function

The decimation technique is a computational approach that calculates the surface Green's function recursively using bulk Green's function. [93-95] Here the full contact Green's function is divided into several finite size Green's function representing a periodic portion of contact far from the device and a finite size Green's function representing a portion which is connected to a device. The requirement for the size of each submatrix is that each submatrix is large enough for the interaction to be limited to their neighboring submatrices. Since it is easier to follow the

mathematical operations up to down, here we begin with the Green's function of the right contact which is shown as

$$g_b = \begin{bmatrix} g_{0,0} & g_{1,0} & \cdots & \cdots \\ g_{0,1} & \ddots & \ddots & \\ \vdots & \ddots & g_{n,n} & \\ \vdots & & & \ddots \end{bmatrix} \quad 3-31$$

where $g_{0,0}$ is the surface Green's function for the right contact. In the decimation technique, the recursive technique is employed to solve the surface Green's function.

$$(\omega^2 I + i\eta - H_c)g_b = I \quad 3-32$$

here H_c is the Hamiltonian of contact. The algorithm for the decimation technique can be summarized in the following steps:

1. Divide the full contact Green's function and the operator matrix to finite portions where each portion is sufficiently large to cover the surface Green's and the interaction between two units is limited to the neighboring ones

$$\begin{bmatrix} \omega^2 I - H_0^s & \tau_0 & 0 & \cdots \\ \tau_0^\dagger & \omega^2 I - H_0^b & \tau_0 & \cdots \\ 0 & \tau_0^\dagger & \ddots & \ddots \\ \vdots & \vdots & \ddots & \ddots \end{bmatrix} \begin{bmatrix} g_{0,0} & g_{0,1} & \cdots & \cdots \\ g_{1,0} & \ddots & \ddots & \\ \vdots & \ddots & g_{n,n} & \\ \vdots & & & \ddots \end{bmatrix} = I \quad 3-33$$

here H_0^s and H_0^b are the Hamiltonian matrices of the surface and bulk finite portion of one contact and the τ_0 is the coupling matrix of two divided portions. The subindices for the Hamiltonian matrices show the iteration number and the Eq. 3-33 is demonstrated at iteration 0.

2. Create and solve the system of equations obtained by multiplication of the operator matrix with a column of the Green's function matrix. As an example, in compact form for column 0, we get

$$(\omega^2 I - H_0^s)g_{0,0} + \tau_0 g_{1,0} = I \quad 3-34$$

$$\begin{aligned}\tau_0^\dagger g_{m-1,0} + (\omega^2 I - H_0^b) g_{m,0} + \tau_0 g_{m+1,0} &= 0, \\ m &= 1, 2, \dots\end{aligned}$$

3. Use the first equation in order to eliminate the divided Green's function element with odd indices and calculate the Green's function with even indices.

$$\begin{aligned}g_{2m+1,0} &= (\omega^2 I - H_0^b)^{-1} (-\tau_0^\dagger g_{2m,0} - \tau_0 g_{2m+2,0}) \quad m = 0, 1, 2, \dots \\ H_1^s &= H_0^s - \tau_0 (\omega^2 I - H_0^b)^{-1} \tau_0^\dagger, H_1^b \\ &= H_0^b - \tau_0 (\omega^2 I - H_0^b)^{-1} \tau_0^\dagger - \tau_0^\dagger (\omega^2 I - H_0^b)^{-1} \tau_0, \tau_1 \\ &= -\tau_0 (\omega^2 I - H_0^b)^{-1} \tau_0\end{aligned} \tag{3-35}$$

4. Use the same strategy as described in step 3 and remove another half of the remaining indices (now for the even indices).

5. Recursively repeat steps 3 and 4 to find the solution for the divided Green's functions. The generic form of the Green's function calculation is shown in the compact form of

$$\begin{aligned}H_n^s g_{0,0} + \tau_n g_{2^n,0} &= I \tag{3-36} \\ \tau_n^\dagger g_{(m-1)2^n,0} + H_n^b g_{m2^n,0} + \tau_n g_{(m+1)2^n,0} &= 0, \\ m &= 1, 2, \dots\end{aligned}$$

then the divided recursive matrices are derived as following

$$\begin{aligned}H_n^s &= H_{n-1}^s - \tau_{n-1} (\omega^2 I - H_{n-1}^b)^{-1} \tau_{n-1}^\dagger, H_n^s \\ &= H_{n-1}^b - \tau_{n-1} (\omega^2 I - H_{n-1}^b)^{-1} \tau_{n-1}^\dagger \\ &\quad - \tau_{n-1}^\dagger (\omega^2 I - H_{n-1}^b)^{-1} \tau_{n-1}, \tau_n^2 \\ &= -\tau_{n-1} (\omega^2 I - H_{n-1}^b)^{-1} \tau_{n-1}\end{aligned} \tag{3-37}$$

6. The recursive process would continue until $\tau_n \rightarrow 0$ and, therefore, the choice of n should be large enough to satisfy this condition. This condition is obvious since the separated portions are within 2^n difference and the long-range interaction are zero as n increases. As a result, we can calculate $g_{0,0} = (\omega^2 I - H_n^s)^{-1}$ which is surface Green's function for the right contact. A similar process could be applied for the left contact as well.

3.4.5 Self-energy and Coupled Green's Function

After surface Green's function calculation, we are going to solve the Eq. 3-26 for the device and calculate the coupled Green's function. The coupled Green's function is inverse of the operator and since the relation 3-27 is coupled with the surface Green's functions of contacts, it is called coupled Green's function.[91] Additionally, self-energies are the actual boundary condition that as a result of the decoupling of the system is appeared in the device equation. Self-energy is calculated as the projection of the surface Green's functions of contacts with the coupling matrices of such.

$$\Sigma = \tau g_s \tau^\dagger \tag{3-38}$$

We should note that the coupling matrices here are different from what was described in section 3.4.3 in terms of the size. In relation 3-27, the coupling matrices are infinitely large in one of the dimensions, while for the surface Green's function, the coupling matrices have a finite size in both dimension wherein one dimension they have a similar size to the device and the other dimension has the similar size as surface Green's function. The calculation for the coupled Green's function is a rather simple mathematical operation. The coupled Green's function for the device with two contacts is

$$G_d = (\omega^2 I - H_d - \Sigma_L - \Sigma_R)^{-1} \quad 3-39$$

where Σ_L and Σ_R are the self-energies of the left and the right contacts respectively. Self-energies have a similar size to the Hamiltonian matrix of the device but unlike that, the self-energies are non-Hermitian matrices. In mathematics, a non-Hermitian matrix is a matrix that is not self-adjoint or in other words, the conjugate transpose of this matrix is not equivalent to the matrix itself ($\Sigma \neq \Sigma^\dagger$). The dynamical system of the non-Hermitian operator generates imaginary eigenvalues while the Hermitian operator which generates only real eigenvalues. To understand the self-energy and impact of the imaginary eigenvalues on the solution, here we discuss the dynamical system in the time domain. The dynamical equation is defined

$$\frac{d^2\Psi}{dt^2} = \varepsilon^2\Psi \quad 3-40$$

and its solution is expressed as $\Psi = \exp(-i\varepsilon t)$ where ε is the eigenvalue of the dynamical system. When the operator is Hermitian, ε 's are real values. We should note that the Eq. 3-40 can be seen as an inverse Fourier transform of the Eq. 3-19 for a Harmonic system. Also, we should note that for a Harmonic system, the operator is always Hermitian and, thus, generates the real eigenvalues. But in the case of the non-Hermitian operator such as when the self-energy is added to the equation, the eigenvalues have imaginary components. The solution of Eq. 3-40 with the self-energy is

$$\Psi = \exp(-i(\sqrt{\varepsilon^2 - \Sigma})t), \quad 3-41$$

this relation can be simplified as follows

$$\Psi \approx \exp(-i\varepsilon t)\exp\left(i\frac{\Sigma t}{2\varepsilon}\right) \quad 3-42$$

If we differentiate the Σ based on its imaginary and its real components, we get

$$\Psi \approx \exp\left(-i\left(\varepsilon + \frac{\text{Re}(\Sigma)}{2\varepsilon}\right)t\right)\exp\left(-\frac{\text{Im}(\Sigma)}{2\varepsilon}t\right), \quad 3-43$$

the first part is similar to the solution for Eq. 3-40 where the real part of σ indicates the energy shift. The second part indicates the decaying function where the imaginary part of Σ is the decaying

factor. The decaying rate in the function represents a lifetime and its distribution has a broadening factor that has an inverse relation with the lifetime. For a given self-energy, the broadening factor (imaginary part) is what encounters the shift in energy (real part). It is easy to show that the broadening factor of the self-energy as

$$\Gamma = i(\Sigma - \Sigma^\dagger) \quad 3-44$$

where Σ^\dagger is the adjoint matrix of Σ and Γ is called “escape rate” or “leakage”. This relation simply returns the imaginary component of the self-energy. To find the width, the Lorentzian function can be fit into Γ in order to find the width of broadening as follows

$$\frac{1}{\tau} = -\frac{\text{Im}(\Sigma)}{\varepsilon} \quad 3-45$$

where τ identifies as a lifetime.

Similar to relation 3-44, the real part of the self-energy is calculated as

$$\Gamma = \frac{1}{2}(\Sigma + \Sigma^\dagger) \quad 3-46$$

Additionally, recalling from the surface Green’s function calculation, it is apparent now that how small imaginary perturbation adds a decaying function into the Hamiltonian equation of contact. However, the encounter component of the energy shift comes as output source term on the right-hand side rather than the real value shift in the frequency.

In summary, in the past few sections, we tried to lay down a detailed interpretation and derivation which lead to the calculation of coupled Green’s function and self-energy of the device. We observed the non-Hermitian aspect of self-energy generates a shift in energy and a broadening which encounters the generated shift. Thus, it is clear why we added a small perturbation to the frequency in Eq. 3-24. Small perturbation creates leakages on two sides of the device which result in non-equilibrium conditions and consequently allows phonon modes to transmit through the device. In this condition, leakages of energy in two sides of the device are not equilibrated and

that's why in many texts this method is known as non-equilibrium Green's function. Therefore, it is possible to calculate the transmission function. The process of adding and decaying for perturbed frequency often is seen as injection and removal of phonon frequency into the system respectively. This process tags the contact as a source and device as a channel that allows the sources to transmit the phonon through. It is obvious that if the perturbation would not be added to the system then the leakage is zero and there is no transmission and neither surface/bulk Green's function nor the source terms are defined. Here the question might be why small perturbation is only added to the contacts and not the device. Added small imaginary perturbation on each contact generates decaying wave propagation that could be dissipated along the semi-infinite length (for left contact, the decaying waves are left-going while for right contact, the decaying waves are right-going). Regarding the device, mathematically, the addition of perturbation to the dynamical system is not solvable since the boundary conditions for the Green's function is not clear. Also, the influence of added perturbation to the frequency physically is minimal for the device with a finite size. In the next sections, we show how the coupled Green's function and self-energies are used to calculate the transmission function and thermal conductance in the device.

3.4.6 Transmission Function and Transmittance

Here before getting to the calculation of transmission function based on Green's function, we are going to provide the definitions for common terms regarding the transmission process. The transmission process is quantified in different forms such as transmission function, transmissivity, and transmittance. The transmission function is defined as the number of transmitted phonon modes between two materials in contact with each other. The transmission function includes

important information such as the density of state of interfacial material and group velocity of the transmitting phonon modes. Transmittance is defined as a fraction of the incident phonon modes which are transmitted which is a proportional relation in contrast to the transmission function. Its value lies between 0 to 1 and is shown as follows

$$\theta = \frac{\Xi_{\text{transmitted}}(\omega)}{\Xi_{\text{incident}}(\omega)} \quad 3-47$$

where $\Xi_{\text{transmitted}}$ and Ξ_{incident} are the number of phonon modes which are transmitted and the number of incident phonon modes respectively. Additionally, transmissivity is defined as the probability of the phonon modes that are transmitted from the incident. Transmissivity is the main component of the classical approach such as DMM.

Next, we are going to derive the relation for the spectral transmission function based on the density matrix and then calculate the transmission function. The density matrix is what describes the statistical states of a quantum system. In one way, transmission function from contact to the device can be defined as a rate of change between their density matrices. Therefore, to calculate the transmission function, first, we need to calculate the density matrices of the device and contacts. For an isolated contact, the density matrix is given as

$$\rho_c(r, r') = \sum_n f_0(\omega_n^2) \phi_n(r) \phi_n^*(r') \quad 3-48$$

where ϕ_n and f_0 are the isolated wavefunctions and distribution function respectively. The above relation can be rewritten in matrix notation as

$$P_c = \sum_n f_0(\omega_n^2) \Phi_n \Phi_n^\dagger \quad 3-49$$

Moreover, we need to calculate the density matrix of the device. We also know that there is a Green's function for this system that connects the eigenfunctions of the device based on the eigenfunctions of the contact. If we incorporate a similar process as section 3.4.5 for the device, we get the wavefunction solution based on the wavefunctions of contact as $\Psi_n = G\tau\Phi_n$ where the

G is the Green's function of device and τ is the coupling matrix between device and contact. The right-hand side (source term) is calculated to be $S_c = \tau\Phi_n$. The density matrix for the device similar to contact is defined as

$$P_d = \sum_n f_0(\omega_n^2)\Psi_n\Psi_n^\dagger \quad 3-50$$

Using the relation between eigenfunctions of device and contact, we can expand the relation 3-50 based on the eigenfunctions of contact as

$$\begin{aligned} P_d &= \sum_n f_0(\omega_n^2)\Psi_n\Psi_n^\dagger = \\ &\int d\omega_n^2 f_0(\omega_n^2) \sum_n \delta(\omega_n^2)\Psi_n\Psi_n^\dagger = \\ &\int d\omega_n^2 f_0(\omega_n^2)G\tau[\sum_n \delta(\omega_n^2)\Phi_n\Phi_n^\dagger]\tau^\dagger G^\dagger \end{aligned} \quad 3-51$$

If we consider the following relations

$$\begin{aligned} A_c &= \sum_n \delta(\omega_n^2)\Phi_n\Phi_n^\dagger \\ \Gamma &= \tau A_c \tau^\dagger \end{aligned} \quad 3-52$$

then we can simplify relation 3-50 to

$$P_d = \int d\omega_n^2 f_0(\omega_n^2)G\Gamma G^\dagger \quad 3-53$$

now by defining $A = G\Gamma G^\dagger$, the relation 3-53 further simplifies to

$$P_d = \int d\omega_n^2 f_0(\omega_n^2)A \quad 3-54$$

This relation is the density matrix of the device with one contact. Now we derive the density matrix for a device with two contacts. We begin with the wavefunction of the device which is defined as

$$\Psi_n\Psi_n^\dagger = GSS^\dagger G^\dagger \quad 3-55$$

where the source term can be expanded in the following form

$$\begin{aligned}
SS^\dagger &= \tau_1 \Phi_1 \Phi_1^\dagger \tau_1^\dagger + \tau_2 \Phi_2 \Phi_2^\dagger \tau_2^\dagger + \tau_1 \Phi_1 \Phi_2^\dagger \tau_2^\dagger \\
&\quad + \tau_2 \Phi_2 \Phi_1^\dagger \tau_1^\dagger
\end{aligned} \tag{3-56}$$

and we know that the wavefunctions of two contacts are disjoint and disconnected, therefore $\Phi_1 \Phi_2^\dagger$ and $\Phi_2 \Phi_1^\dagger$ are zero and the relation 3-56 is simplified as $SS^\dagger = \tau_1 \Phi_1 \Phi_1^\dagger \tau_1^\dagger + \tau_2 \Phi_2 \Phi_2^\dagger \tau_2^\dagger$. Now it is straightforward to show the density matrix of the device is

$$\begin{aligned}
P &= \int d\omega_n^2 f_0(\omega_n^2) \sum_n \delta(\omega_n^2) \Psi_n \Psi_n^\dagger = \\
&\int d\omega_n^2 f_0(\omega_n^2) \sum_n \delta(\omega_n^2) G(\tau_1 \Phi_1 \Phi_1^\dagger \tau_1^\dagger + \tau_2 \Phi_2 \Phi_2^\dagger \tau_2^\dagger) G^\dagger = \\
&\int d\omega_n^2 f_0(\omega_n^2) G \tau_1 (\sum_n \delta(\omega_n^2) \Phi_1 \Phi_1^\dagger) \tau_1^\dagger G^\dagger + \\
&\int d\omega_n^2 f_0(\omega_n^2) G \tau_2 (\sum_n \delta(\omega_n^2) \Phi_2 \Phi_2^\dagger) \tau_2^\dagger G^\dagger \\
&= \int d\omega_n^2 f_0(\omega_n^2) G \tau_1 A_1 \tau_1^\dagger G^\dagger + \int d\omega_n^2 f_0(\omega_n^2) G \tau_2 A_2 \tau_2^\dagger G^\dagger
\end{aligned} \tag{3-57}$$

where A_1 and A_2 are the spectral function of the isolated right and the isolated left contacts respectively. If we consider $\Gamma_1 = \tau_1 A_1 \tau_1^\dagger$ and $\Gamma_2 = \tau_2 A_2 \tau_2^\dagger$, the relation 3-50 can be further simplified as

$$P = \int d\omega_n^2 f_0(\omega_n^2) G \Gamma_1 G^\dagger + \int d\omega_n^2 f_0(\omega_n^2) G \Gamma_2 G^\dagger \tag{3-58}$$

This relation points directly to the non-equilibrium density matrix for a device which results in the flow of the phonon modes from one contact to another. Now we calculate the current phonon flow in the device by finding the expression for derivative of the probability density. We begin with the dynamical system in Eq. 3-24 and we use the same notation here. The time derivative of probability density is given as

$$I \equiv \frac{d}{dt} \bar{u}_d \bar{u}_d^\dagger \tag{3-59}$$

where \bar{u}_d is the wavefunctions of the device. If we take a similar implementation to the relation 3-57 here, the rate of change of probability density is calculated as

$$I \equiv \frac{d}{dt} \bar{u}_d \bar{u}_d^\dagger = \frac{\omega (\text{Tr} [\bar{u}_d^\dagger \tau_1 \bar{u}_1 - \bar{u}_1^\dagger \tau_1^\dagger \bar{u}_d])}{2i} \quad 3-60$$

We take Eq. 3-60 from here and expand it with the eigenfunction that is divided into isolated and reflected wavefunctions as

$$I = \frac{\omega}{2i} \text{Tr} [\bar{u}_d^\dagger \tau_1 \bar{u}_1^i - \bar{u}_1^{i\dagger} \tau_1^\dagger \bar{u}_d] - \frac{\omega}{2i} \text{Tr} [\bar{u}_1^{r\dagger} \tau_1 \bar{u}_d - \bar{u}_d^\dagger \tau_1^\dagger \bar{u}_1^r] \quad 3-61$$

the current flow is now divided into two terms where the first and second terms are known as inflow and outflow respectively. The inflow is the rate of change of probability density proportional to the incident phonon modes (isolated contact modes) and the outflow is the rate of change proportional to the reflected/scattered phonon modes (reflected contact modes) from contact 1. The inflow can be modified in terms of the Green's function and source terms such that

$$I_{\text{inflow}} = \frac{\omega}{2i} \text{Tr} [S^\dagger G^\dagger S_1 - S_1^\dagger G S] = \frac{\omega}{2i} \text{Tr} [S_1 S_1^\dagger (G^\dagger - G)] = \frac{\omega}{2} \text{Tr} [S_1 S_1^\dagger A] \quad 3-62$$

similarly, for outflow, we get

$$I_{\text{outflow}} = \frac{\omega}{2i} \text{Tr} [\bar{u}_d^\dagger \tau_1 g_1^\dagger \tau_1^\dagger \bar{u}_d - \bar{u}_d^\dagger \tau_1 g_1 \tau_1^\dagger \bar{u}_d] = \frac{\omega}{2i} \text{Tr} [S^\dagger G^\dagger G S (\tau_1 g_1^\dagger \tau_1^\dagger - \tau_1 g_1 \tau_1^\dagger)] = \frac{\omega}{2i} \text{Tr} [G S S^\dagger G^\dagger \Gamma_1] \quad 3-63$$

Next, we sum over all the eigenstates and subtract the outflow from inflow, therefore we get

$$\begin{aligned}
J_1 &= I_{\text{inflow}} - I_{\text{outflow}} \\
&= \int \frac{\hbar\omega}{2\pi} \{\text{Tr}[A_d\Gamma_1]f_1 - \text{Tr}[f_1A_1\Gamma_1 + f_2A_2\Gamma_2]\}d\omega \\
&= \int \frac{\hbar\omega}{2\pi} \text{Tr}[A_2\Gamma_1][f_1 - f_2]d\omega \\
&= \int \frac{\hbar\omega}{2\pi} \text{Tr}[\Gamma_1G\Gamma_2G^\dagger][f_1 - f_2]d\omega
\end{aligned}
\tag{3-64}$$

where $\Xi_{\text{transmitted}} = \text{Tr}[\Gamma_1G\Gamma_2G^\dagger]$ is known as transmission function in spectral space and the relation 3-64 is equivalent of Landauer formula. An exactly similar process could be applied concerning the device and contact 2 and the transmission function in this case is

$$\begin{aligned}
\Xi_{\text{transmitted}} &= \text{Tr}[\Gamma_2G\Gamma_1G^\dagger] \\
J_2 &= \int \frac{\hbar\omega}{2\pi} \Xi_{\text{transmitted}} [f_2 - f_1]d\omega
\end{aligned}
\tag{3-65}$$

This concludes the spectral transmission function calculation. In many instances for transmission matrix and transmission function itself, a spectral function of A was defined in the derivations, next we will see how this function is used to calculate the local DOS.

3.4.7 Local Density of States

One of the important features of Green's function approach is the ability to calculate local DOS for any component of the system. To find the local DOS, first, we need to define global DOS which measures the number of the phonon modes at a particular frequency (ω) with a determined broadening factor (δ). The global DOS for a Harmonic matrix as H is defined as

$$D(\omega) = \sum_n^N \delta(\omega - \omega_n) = \sum_n^N 2\omega\delta(\omega^2 - \omega_n^2)
\tag{3-66}$$

here both relations satisfy the following property for a DOS

$$\int_{\omega_n-0^+}^{\omega_n+0^+} \delta(\omega - \omega_n) d\omega = \int_{\omega_n-0^+}^{\omega_n+0^+} 2\omega \delta(\omega^2 - \omega_n^2) d\omega = 1 \quad 3-67$$

Then the local DOS is calculated as a weighted form of relation 3-61 based on the probability density as

$$D(\vec{d}, \omega) = \sum_n^N 2\omega \delta(\omega^2 - \omega_n^2) \phi_n(\vec{d}) \phi_n^*(\vec{d}) \quad 3-68$$

where ϕ_n 's are the local eigenfunctions for mode n which are calculated for the contacts or the device. The local DOS can be written into a matrix form where the diagonal elements are calculated from relation 3-68. The modified relation is

$$D(\vec{d}, \vec{d}'; \omega) = 2\omega \sum_n^N \delta(\omega^2 - \omega_n^2) \phi_n(\vec{d}) \phi_n^*(\vec{d}') \quad 3-69$$

where the diagonal components of this relation are the spectral local DOS. Additionally, we define the spectral function as

$$A(\vec{d}, \vec{d}'; \omega) = 2\pi \sum_n^N \delta(\omega^2 - \omega_n^2) \phi_n(\vec{d}) \phi_n^*(\vec{d}') \quad 3-70$$

This relation enables us later to derive the local DOS based on the Lorentzian function.

Here we can write the local DOS based on this spectral function such that

$$D(\vec{d}, \vec{d}'; \omega) = \frac{\omega A(\vec{d}, \vec{d}'; \omega)}{\pi} \quad 3-71$$

here we can fit a Lorentzian function for diagonal elements of matrix A . If n th element of the matrix A is given then the spectral function of that element is

$$A(\omega) = 2\pi \delta(\omega^2 - \omega_n^2) = \lim_{\eta \rightarrow 0^+} \frac{2\eta}{(\omega^2 - \omega_n^2)^2 + \eta^2} \quad 3-72$$

where the Lorentzian function further can be separated into two fractions as

$$\lim_{\eta \rightarrow 0^+} \frac{2\eta}{(\omega^2 - \omega_n^2)^2 + \eta^2} \approx i \left(\frac{1}{\omega^2 - \omega_n^2 + i0^+} - \frac{1}{\omega^2 - \omega_n^2 - i0^+} \right) \quad 3-73$$

It is apparent that the first fraction is the definition of retarded Green's function and the second fraction is the definition of the self-advance Green's function. Therefore, the spectral function is calculated such that $A(n, n; \omega) = i(G(n, n; \omega) - G^*(n, n; \omega))$. Furthermore, we can generalize these relations in matrix notation. The generalized spectral function is

$$A(\omega) = 2\pi\delta(\omega^2 I - H) \quad 3-74$$

where H is the Hamiltonian matrix with diagonal elements. Based on this relation, spectral function A can be generalized with the Green's function as

$$\begin{aligned} A(\omega) &= 2\pi\delta(\omega^2 I - H) \\ &= i((\omega^2 - H + i0^+)^{-1} - (\omega^2 - H - i0^+)^{-1}) \\ &= i(G - G^\dagger) \end{aligned} \quad 3-75$$

here G is a retarded Green's function in a matrix format.

As we have seen before, the broadening of DOS is tied with the choice of η . Earlier we mentioned that η should be small enough to retain a linear dynamical system. However, continuity of DOS requires a broadening factor which is larger than the frequency difference between two local DOS's of interfacial materials. This means that the choice of η should be large enough that the continuous local DOS's are obtained for a coupled system of device and contacts. Figure 14 shows the interpretation of the frequency exchange in the interface as a source (contact) and drain (device).

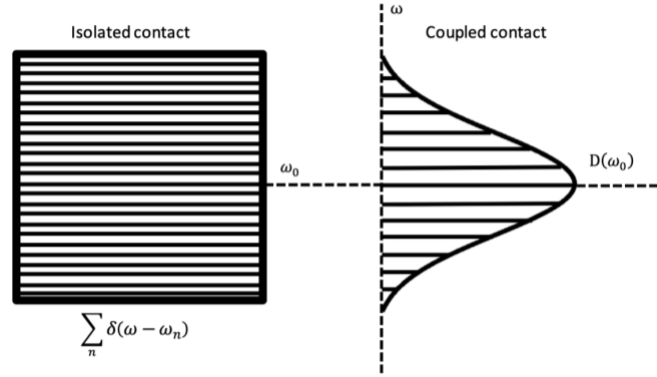


Figure 14 Frequency distribution exchange for the isolated contact (left) and a broadening of frequency level for a coupled system of contact and device (right)

Figure 14 indicates how the frequency from an isolated contact is changed to the frequencies in the coupled system of contact and device. The frequency levels in isolated contact are a quantized set. We can see two quantized frequency levels which would indicate the frequency of the device and contact. The set of frequencies would match each other at the interface. The difference in frequency level is included in the source term and the broadening necessary to match the quantized frequency levels is the small perturbation. The only way to get continuous DOS is to maintain a fine frequency grid and appropriate choice of η to cover the differences.

Additionally, from Green's function representation, we know that the broadening is also described by the self-energy term. If the self-energy term is calculated, then its imaginary component shows the broadening factor, which in this case, Green's function is given as $G = (\omega^2 I - H - \Sigma)^{-1}$; if we put this equation back into the local DOS, we obtain second relation to calculate the local DOS as

$$A(\omega) = G\Gamma G^\dagger \quad 3-76$$

If we compare relations 3-68 with 3-64 or 3-65, we could see how the local DOS is playing a role in the transmission function formulation. Also, we note this formulation is more useful when the self-energy or escape rate terms are calculated.

Moreover, in many instances, the frequency times DOS is reported. In literature [91, 93], usually, the frequency times Green's function is noted as $G^<$, therefore the relations for frequency times local DOS are calculated as

$$fA = i(G^< - G^{<\dagger}) = G^<\Gamma G^{<\dagger} \quad 3-77$$

3.4.7.1 Remarks

1. In practical applications, the size of each component is important. The device usually includes all the dissimilarities but it should be large enough to make a clear separation between two contacts. As we have assumed and shown in this chapter, two contacts do not interact with each other. Also, the size of contacts depends on their periodic units and the size of small perturbation. The size of contact should be large enough that the periodicity is fully obtained and the frequency demonstrates a decaying behavior.
2. The surface Green's function is the response to the addition of a small decaying component (imaginary frequency) to the dynamical system of contact. The decay of the additional component constitutes the Dirichlet boundary condition at the far end of the contact which satisfies the requirement for surface Green's function solution. The validity of the surface Green's function depends on capturing the full decay length; however, the extent of decay depends on the value of a small imaginary component which is an arbitrary value in our simulations. In this regard, the decimation technique provides a robust recurrent numerical

technique that guarantees the convergence of the decaying process in contact for any arbitrary value of an imaginary component. The analytical approach is only good when there is a full understanding of the extent of the decaying process in a contact.

3. All the given calculations can be generalized into the 2D and 3D materials. If the material's non-periodicity is along transmission direction only, other periodic dimensions could be dealt with as a simple lattice dynamics calculation. For instance, if we have a 3D material with only non-periodic structure along the transmission direction, we only need to solve the Green's function along the transmission direction and the transmission function would be the average over all the polarization in two other periodic dimensions. In this case, the problem reduces to the solution which resembles many 1D atomic chains of the device and two contacts. [18, 96, 97]

4.0 Quantum Phonon Transport Across Grain Boundaries in Graphene using Machine Learning Based on Small Dataset

4.1 Introduction

Grain boundaries (GBs) are of interest in many applications because they are common defects and largely affect electrical, mechanical, and thermal properties. For two dimensional (2D) materials such as graphene, experimental studies showed that GBs commonly exist in graphene sheets prepared by exfoliation [69, 98-101], causing the fundamental physical properties of polycrystal samples largely deviate from those of single crystals. Therefore, engineering GBs is an effective way to achieve desired electronic, thermal, and mechanical properties in many applications [14, 102-109].

The physical properties are largely dependent on the local atomic structure of GB [101, 102, 110] and thus it is important to establish the structure-property relationship on how a GB structure affects the physical properties. However, establishing such a structure-property relationship has been challenging mainly for two reasons. The first is that GBs have extremely large configurational space. For example, three dimensional (3D) materials have 5 degrees of freedom (misorientation angle noted as θ_M hereafter, line angle, and three degrees of freedom of crystalline grain orientation in 3D space) for GB structures, making the configurational space extremely large. The second is that the experimental characterization of individual GB requires significant efforts particularly for preparing samples with a geometrically well-defined GB. The samples with GBs have been prepared by bonding two wafers with a twist angle but it often leaves

a void at the interface [111]. Therefore, it is challenging to experimentally study enough number of GBs to draw a statistically conclusive finding on the structure-property relationship.

Atomistic simulation can be a useful tool for the study of GBs if it has high predictive power, but also has major challenges. The atomistic simulation for thermal transport such as molecular dynamics (MD) [103-105, 112-114] and the atomistic Green's function (AGF) [109, 115] require an interatomic potential. A common approach for the interatomic potential has been empirical potentials that have a rigid functional form parametrized based on quantum mechanical calculation results and experimental data. Although the empirical potentials have been useful for promoting the understanding of physical phenomena from an atomistic level, they have clear limitations. For the physical properties that were not considered for the parametrization, empirical potentials do not provide an accurate prediction. Also, because of its rigid functional form, it is usually not flexible enough to describe a wide range of atomic configurations. On the contrary, ab initio calculation can be highly accurate and have a predictive power without adjustable parameters as demonstrated by the recent studies. For example, the high thermal conductivity of boron arsenide was experimentally confirmed [116-118] after the prediction from ab initio simulation [119]. Also, the significant hydrodynamic phonon transport in graphitic materials was predicted using ab initio simulation first [120, 121] and then experimentally confirmed [122, 123]. However, the ab initio simulation for thermal transport has been limited to single crystalline phase and point defect cases. For the thermal transport across GBs, the ab initio simulation is not feasible due to its high computational cost considering the size of GB atomic structures.

A recently emerging method is to use machine learning schemes to predict the interatomic interactions based on the dataset from ab initio simulations [25, 124-134]. This so-called machine learning interatomic potential (MLIP) was motivated by the fact that the interatomic interaction is

a function in a high dimensional space where machine learning outperforms conventional regression methods. Recently developed MLIPs show that the MLIP can be as accurate as ab initio calculations while its computational cost is several orders-of-magnitude cheaper than the ab initio calculations [25, 70, 124, 125]. In particular, the MLIP was proven for predicting the thermal transport in the crystalline phase [25, 125, 128] and partially disordered crystalline phase that has vacancies [25]. This confirms that the MLIP is accurate enough to correctly capture subtle anharmonicity, which is critical for phonon-phonon scattering and phonon-strain field scattering, and is also flexible enough to describe various atomic configurations including vacancies. However, extending the past success of MLIP to spatially extended disorder case (e.g., GBs) has some challenges. Unlike vacancies, the GBs have extremely large atomic configurational space. Therefore, the training dataset should be carefully designed such that it can represent the entire configurational space. In addition, the size of the training dataset should be minimal since generating the training dataset from ab initio calculation can be prohibitively expensive considering the typical size of GB structures.

In this work, we develop MLIPs using the Gaussian regression, called the Gaussian approximation potential (GAP) [70, 72], for studying phonon transport across graphene GBs. We use a systematic framework based on the structural unit model to select the complete and orthogonal training dataset. With the carefully chosen a few GBs for the training dataset, we show that the GAP can produce identical results as the ab initio calculations for the wide range of GBs while its computational cost is 6 orders of magnitude cheaper than the ab initio calculations. We should note that our MLIP is 3 orders of magnitude more expensive than the empirical potential for a molecular dynamic simulation. Using the GAP and AGF, we then report several important features of phonon transport across GBs in graphene with its high predictive power. We distinguish

the influence of dislocation core and extended strain field on phonon scattering, and reveal an intriguing scattering of flexural phonon modes by out-of-plane buckling in graphene GBs. We also briefly evaluate an empirical Tersoff potential (TSF) [135, 136] that has been widely used in past studies by comparing it to GAP.

4.2 Methods

4.2.1 Identifying the Small Set of GBs Representing the Entire Configurational Space of GBs

In this work, we consider a total 20 GBs that covers the full span of θ_M (0° to 60°) which include a variety of disclination densities and different topological arrangement of disclinations. We focus on symmetric GBs with zero line angle because several parameters that are expected to affect phonon scattering such as GB formation energy, dislocation density, and out-of-plane roughness are nearly unchanged with the line angle in graphene [100]. To best of our knowledge, the set of selected GBs represent the most complete set of graphene GBs which are studied for thermal properties. The θ_M and coincidence site lattice (CSL) Σ values of the 20 GBs are listed in Table 1. The supercells containing each of GBs were generated using an algorithm based on the centroidal Voronoi tessellation [100]. Then, we appended the same supercell that is rotated by 180° resulting in two GBs along with the opposite directions in a supercell. Such supercells are preferred for the subsequent relaxation process using MD simulation since they have translational symmetry along all directions including the direction perpendicular to the GB line. An example supercell is shown in figure 10.

We then relaxed the obtained supercell by running MD simulations at 300 K in the NVT ensemble over 100 ps using the LAMMPS package, with a time step of 0.5 fs and TSF potential. Those supercells were used for training a GAP based on TSF interatomic potential (GAPTSF), which was used for the validation of our methods. A separate set of 20 supercells were further relaxed by density functional theory (DFT) calculation to develop another GAP based on DFT (GAPDFT) which we used to study the phonon transport across GBs in graphene. For the DFT calculations, we used the energy minimization scheme in the VASP package using ultrasoft pseudopotentials with a plane wave cutoff energy of 286 eV. The convergence criteria for energy and force were set to 10^{-8} eV and 10^{-6} eV/Å, respectively. The resulting supercells relaxed by TSF and DFT slightly differ as shown in Table 2.

Table 2 List of the 20 GBs with their structural properties. The 5 representative GBs chosen by the SOAP dissimilarity analysis are indicated with superscripts † and ‡ for the structures relaxed by TSF and DFT, respectively.

index	θ_M (deg.)	CSL Σ	Structures relaxed by TSF		Structures relaxed by DFT	
			GB period (Å)	Disclination density (Å ⁻¹)	GB period (Å)	Disclination density (Å ⁻¹)
1	6.01 [†]	91	23.7608	0.0842	23.3084	0.0858
2	7.34	61	19.4537	0.1028	19.0835	0.1048
3	9.43	37	15.1509	0.132	14.8627	0.1346
4	10.99	109	26.0123	0.1537	25.5172	0.1568
5	13.17 [‡]	19	10.8593	0.1842	10.6527	0.1877
6	16.43	49	17.4449	0.2293	17.1116	0.2337
7	17.9 [†]	93	24.0326	0.2497	23.5727	0.2545
8	21.79 [‡]	7	6.6012	0.3029	6.4725	0.309
9	26.01 [‡]	79	22.1546	0.3611	21.7306	0.3681
10	27.8	39	15.5647	0.3855	15.2662	0.393
11	29.41	97	24.5397	0.4075	24.0737	0.4154
12	32.2	13	8.9919	0.4448	8.8178	0.4536
13	35.57	67	20.3977	0.3922	20.0072	0.3998
14	40.35 ^{†,‡}	103	25.2933	0.3163	24.8106	0.3224
15	42.1	31	13.8792	0.2882	13.6149	0.2938
16	44.82 [†]	43	16.3393	0.2448	16.0284	0.2496
17	46.83	57	18.8093	0.2127	18.4503	0.2168
18	48.36 ^{†,‡}	73	21.2859	0.1879	20.8804	0.1916
19	49.58	91	23.7631	0.1683	23.3122	0.1716
20	50.57	111	26.2369	0.1524	25.7374	0.1554

A challenge in developing an MLIP for GBs is how to prepare a complete set of training data. Considering the typical period length of GBs and the area strained by a GB, a supercell that contains a GB can be often too large for the ab initio calculation. Thus, for the training dataset, it is critical to select a small set of GBs that can represent the entire configurational space of GBs. In early studies developing an MLIP for general purpose, a fraction of the total database was chosen for the training dataset without much rationale, with the remaining as the testing dataset [25, 70, 72, 73, 137]. Recently, active learning schemes have been proposed to reduce the size of training dataset [138-140], making it possible to simulate the dynamic evolution of systems such as phase change in a large scale for a long time period. While the active learning scheme can be used for general cases, it does not allow to use of preexisting knowledge on the system of study even when it is available. Besides, the active learning scheme is more suitable for molecular dynamics simulation in which a training dataset is added based on the measured uncertainty at each time step. For phonon transport simulation, the lattice dynamics-based method (e.g., AGF) has several important advantages over molecular dynamics simulations such as modal analysis and no statistical error.

We use the fact that most GBs have hierarchical structures with basic building blocks as demonstrated in the previous studies that analyzed the GB structures with the structural unit model [141-143]. A basic idea is to identify those basic building blocks or unique local atomic environments (LAEs) from many GBs and find a small set of GBs that contain the complete set of the unique LAEs [144]. Then, an MLIP trained with the data from the small set of GBs is expected to accurately capture the interatomic interactions of GBs in the entire configurational space.

We used the smooth overlap of atomic positions (SOAP) [87] descriptor to find the smallest GB dataset that contains all the representative LAEs in the 20 GBs. The SOAP descriptor places a Gaussian function on each atom to construct the density of neighbor atoms ρ_i , which is then expanded in a basis set of radial functions $g_n(r)$ and spherical harmonics $Y_{lm}(r)$ as

$$\rho_i(\mathbf{r}) = \sum_{nlm} c_{nlm}^{(i)} g_n(r) Y_{lm}(\mathbf{r}), \quad 4-1$$

where $c_{nlm}^{(i)}$ are the expansion coefficients for atom i . The descriptor is formed from these coefficients by computing the power spectrum elements

$$p_{nn'l}^{(i)} = \frac{1}{\sqrt{2l+1}} \sum_m c_{nlm}^{(i)} (c_{n'l m}^{(i)})^*. \quad 4-2$$

The resulting descriptor has invariance under translation, rotation, and the permutation of atoms. For each GB, a SOAP descriptor for each atom i in the GB is calculated and represented as coefficients of basis functions $\mathbf{p}_i = \{p_1, p_2, \dots, p_N\}$. The length of the SOAP vector N is determined by a radial basis cutoff n_{\max} and an angular basis (spherical harmonic) cutoff l_{\max} . We evaluate the dissimilarity of LAEs using SOAP descriptors which is defined as [144]:

$$d_{ij} = \sqrt{\mathbf{p}_i \cdot \mathbf{p}_i + \mathbf{p}_j \cdot \mathbf{p}_j - 2\mathbf{p}_i \cdot \mathbf{p}_j} \quad 4-3$$

where \mathbf{p}_i and \mathbf{p}_j are the SOAP vectors for the two atoms i and j . We introduce a parameter ϵ , serving as a criterion for the unique LAE. If $d_{ij} > \epsilon$, the \mathbf{p}_i and \mathbf{p}_j are different from each other indicating that the two atoms i and j are surrounded by different LAEs. Otherwise, we determine \mathbf{p}_i and \mathbf{p}_j represent the same LAE. In this work, we used 0.04 for the value of ϵ .

The 20 GBs covering the full span of θ_M contain a total of 5544 LAEs and the dissimilarity analysis show that there exists significant overlap among the 5544 LAEs; the total 5544 LAEs can be reduced to only 12 and 13 unique LAEs for the structures relaxed by TSF and DFT, respectively. The TSF and DFT produce slightly different structures after relaxation, and hence the number of

unique LAEs also differ. The analysis shows that the total 20 GBs covering the full span of θ_M can be composed using those 12 or 13 unique LAEs, confirming the idea that the extremely large configurational space of GBs in fact have a very small number of basic building blocks. We then identified 5 representative GBs shown in figure 16 that contain all of the 12 or 13 unique LAEs. The selected GBs significantly differ from each other in terms of the topological arrangements and the density of disclinations. We used the 5 GBs to generate a training dataset for our GAP, train the GAP, and performed the AGF simulation with the GAP to simulate the phonon transport across GBs as discussed in the method sections.

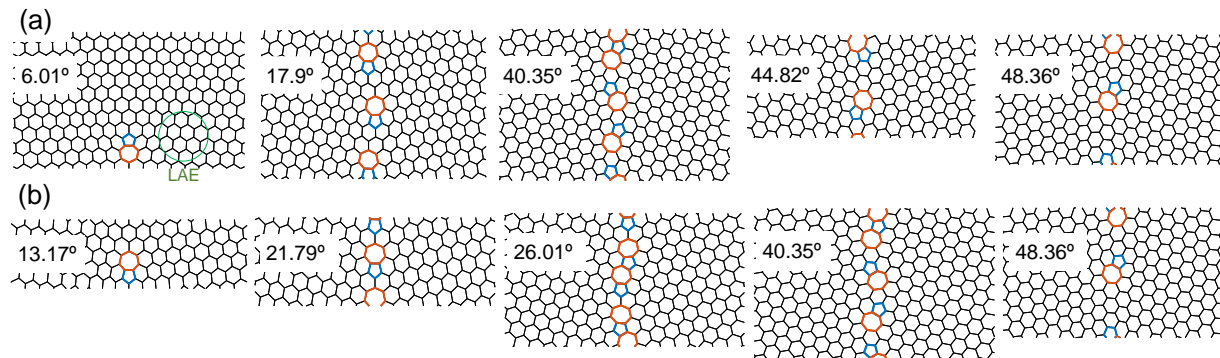


Figure 15 Five representative GBs from (a) TSF and (b) DFT showing distinct features such as density of disclinations and their topological arrangements. The angle in each figure shows the misorientation angle.

The green circle shows the cutoff radius for defining LAE.

4.2.2 Training GAP

We trained two separate GAPs: GAPTSF for the validation of our methods using relatively cheap TSF potential and GAPDFT for studying of phonon transport across GBs with ab initio accuracy. For training dataset, we performed MD simulations of the 5 representative GBs and obtained the snapshots of the atomic position, force, and energy. The MD simulations were

performed at 300 K in the NVT ensemble with a time step of 0.5 fs. After initial time steps for thermal equilibration, we took one snapshot every 50 time steps to reduce the correlation between snapshots. The training datasets for both GAPTSF and GAPDFT include relaxed structures of the 5 selected GB structures and 50 snapshots for each GB at 300K. After obtaining the training dataset, we used the hyperparameters listed in Table 3 to train GAPTSF and GAPDFT.

Table 3 List of hyperparameters for GAPTSF and GAPDFT

Hyperparameter	Note	2-body	3-body	SOAP
$r_{\text{cut}} (\text{\AA})$	Cutoff radius of the descriptor	4.0	4.0	4.0
$d (\text{\AA})$	Transition width over which the magnitude of SOAP descriptor monotonically decrease to 0	-	-	1.0
$\delta (\text{eV})$	Weight of different descriptors	10.0	3.7	0.07
N_t	Number of representative atomic environments selected using the corresponding sparse method	50	200	650
Sparse method		Uniform	Uniform	CUR
n_{max}	Radial basis cutoff	-	-	12
l_{max}	Angular basis cutoff	-	-	12
$\sigma_{\text{energy}} (\text{eV/atom})$	Expected error for atomic energy	0.001		
$\sigma_{\text{force}} (\text{eV/\AA})$	Expected error for force	0.0005		

4.2.3 AGF Simulation

For the AGF simulation, the supercell needs to be sufficiently large so that the leads do not have strain from a GB. The supercell we used for the AGF calculation is 10 times longer in the direction perpendicular to GBs than those we used for SOAP dissimilarity analysis and training GAP. Since the AGF simulation does not require translational symmetry along the heat flow direction, the supercells for the AGF calculation contain only one GB for each unlike those for training the GAP that have two GBs. The comparison of supercells for GAP training and AGF simulation in terms of the size can be found in Table S1 in the supplementary information. The second-order force constants were calculated using phonopy [145] and LAMMPS [146] with GAPTSF or GAPDFT. In the AGF simulation, we used decimation technique [94, 95] to approximate surface Green's functions and we used a frequency broadening factor of 1 cm^{-1} for the continuous representation of discrete eigenfrequencies. We observed a good convergence of transmission function with 20 transverse wavevectors for the GB with the largest width ($\theta_M=50.57^\circ$). For other GBs, the number of transverse wavevectors was determined such that the product of the number of transverse wavevectors and the width of GB is the same for all GBs. We should note that our AGF simulation framework result in nearly similar transmission function and thermal conductance to compare with previous work which used empirical potential and AGF simulation for graphene GBs [109]. From previous study, the calculated thermal conductance of two common GBs, GB17 and GB20, are $0.66 \text{ GW/m}^2\text{K}$ and $4.2 \text{ GW/m}^2\text{K}$ at 100K and 300K respectively which are close to our calculation of $0.65 \text{ GW/m}^2\text{K}$ and $4.18 \text{ GW/m}^2\text{K}$ at 100K and 300K respectively. This may serve as validation for our AGF simulation framework.

4.3 Results and Discussions

We use the GAPTSF to validate our simulation framework from selecting representative GBs to the AGF calculation. Unlike the ab initio calculation, the TSF potential is computationally cheap enough to generate the data of interatomic force constants and transmission function of all the 20 GBs. Therefore, the GAPTSF can be directly validated against the results from TSF for all the 20 GBs. In figure 17, we compare the GAPTSF and TSF for the GB formation energy, and spectral phonon transmission function. The GAPTSF and TSF agree well with each other for the prediction of the GB energy for both the training and testing GBs. In particular, the spectral phonon transmission functions, the property of interest in this work, are identical for all GBs. This confirms that the 5 GBs chosen from the LAE analysis are enough to represent the entire 20 GBs and thus the resulting GAP is highly accurate and reliable for a wide range of GBs.

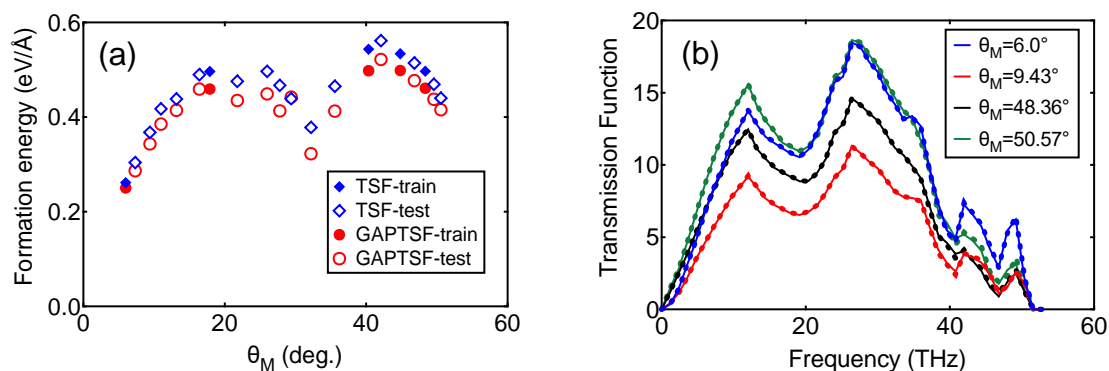


Figure 16 Validation of GAPTSF against TSF for (a) formation energy of GBs, and (b) transmission function. The solid symbols in (a) represent GBs used for training the GAPTSF. The solid lines and dots in (b) are from GAPTSF and TSF, respectively. In (b), the two GBs with $\theta_M=6.0^\circ$ and 48.36° and the other two GBs with $\theta_M=9.43^\circ$ and 50.57° are from the training and testing dataset, respectively.

With the success of GAPTSF, we proceeded to developing GAPDFT using the training dataset from DFT calculation. Like GAPTSF, the GAPDFT also shows excellent accuracy. The

root-mean-square of errors (RMSE) of energy and force are 0.0011 eV and 0.052 eV/Å respectively for the training set, and the RMSE of energy and force are 0.0019 eV and 0.066 eV/Å respectively for the testing set. In figure 18, we examine the GAPDFT compared to DFT for the relaxed atomistic structures. The structures relaxed by the GAPDFT are identical to those by DFT in particular for the out-of-plane atomic displacements.

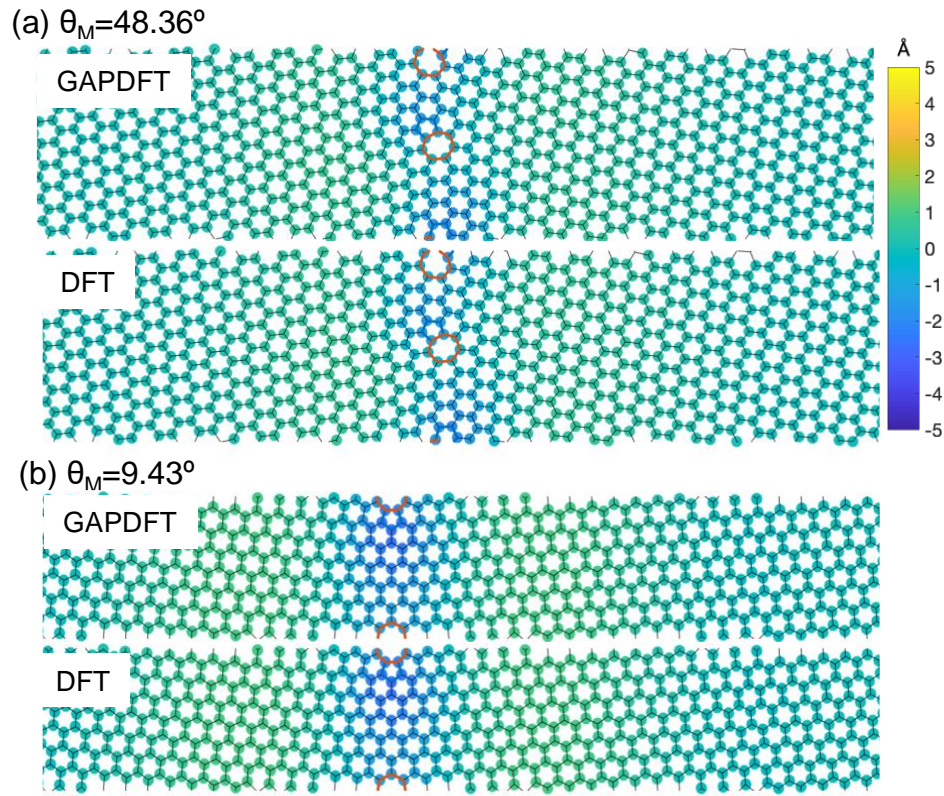


Figure 17 Validation of GAPDFT against DFT for relaxed structures projected onto a-b plane. (a) $\theta_M = 48.36^\circ$ from the training dataset and (b) $\theta_M = 9.43^\circ$ from the test dataset. The color represents out-of-plane displacement in Å.

Figure 19 presents the GB formation energy from GAPDFT and DFT, showing good agreement between them for the entire range of θ_M . The overall trend of GB formation energy from the GAPDFT follows the trend predicted by the Read-Shockley model [147]; the GB

formation energy is linear to θ_M for low θ_M ($<15^\circ$) and high θ_M ($>45^\circ$) while the mid-range θ_M show non-monotonic behavior of GB formation energy with respect to θ_M .

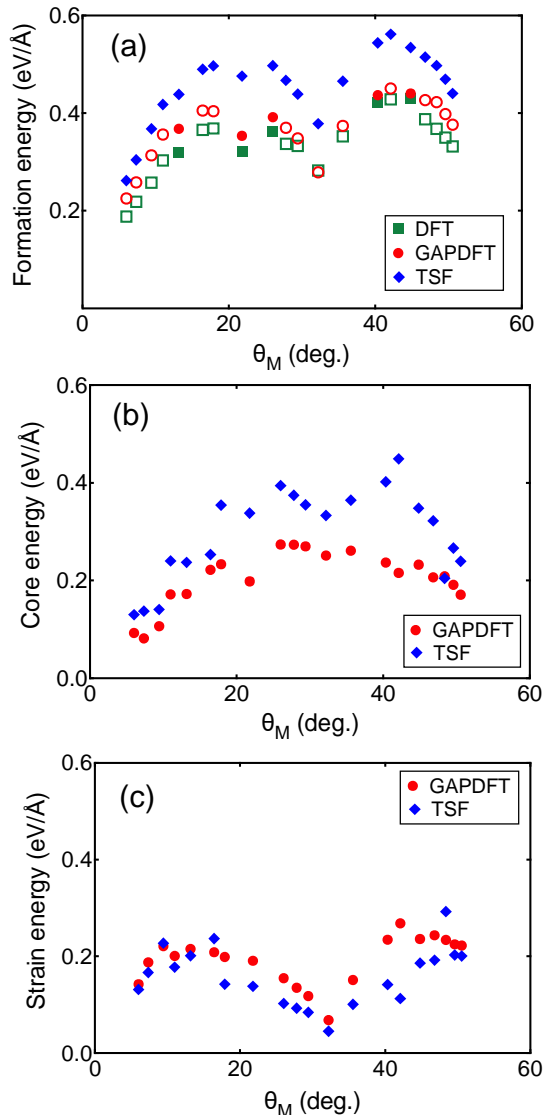


Figure 18 Comparison of DFT, GAPDFT, and TSF for (a) GB formation energy, (b) core energy, and (c) strain energy. The solid symbols in (a) represent the GBs that were used for training GAPDFT.

In figures 19b and 19c, we separate the GB formation energy into the contribution from local dislocation cores (core energy, E_{core}) and surrounding strain field (strain energy, E_{strain}) [148, 149] to better understand the GB formation energy and its effects on phonon transport. We should note that this is one of the noteworthy advantages of MLIPs. The MLIPs can predict each

atom's contribution to total energy while DFT cannot in principle. The core energy (E_{core}) and strain energy (E_{strain}) can be defined as:

$$E_{\text{core}} = \frac{\sum_i^{N_{\text{core}}} E_i - \frac{N_{\text{core}}}{N_{\text{tot}}} E_{\text{bulk}}}{l_{\text{unit}}} \quad 4-4$$

$$E_{\text{strain}} = \frac{\sum_i^{N_{\text{strain}}} E_i - \frac{N_{\text{strain}}}{N_{\text{tot}}} E_{\text{bulk}}}{l_{\text{unit}}} \quad 4-5$$

where N_{core} and N_{strain} are the number of atoms forming dislocation cores (pentagons and heptagons) and hexagon lattices, respectively. The N_{tot} is the total number of atoms. The E_{bulk} and l_{unit} are the energy per atom in the perfect crystalline phase and the length of GB. The core energy and strain energy from GAPDFT in figures 18b and 18c seem physically reasonable. Since the GB in 2D material is equivalent of 1D chains of aligned dislocations, the dislocation density only depend on the number of dislocations that are placed along the GB line. The dislocation density linearly increases with θ_M , have a maximum value at mid- θ_M , and linearly decreases with θ_M (see figure 20). Therefore, the core energy in figure 19b is maximum in the mid- θ_M range where the dislocation density is maximum. The strain energy is minimum in the same θ_M range where the lattice can open up to insert one additional lattice plane to form an edge dislocation and thus the strain is minimized [150].

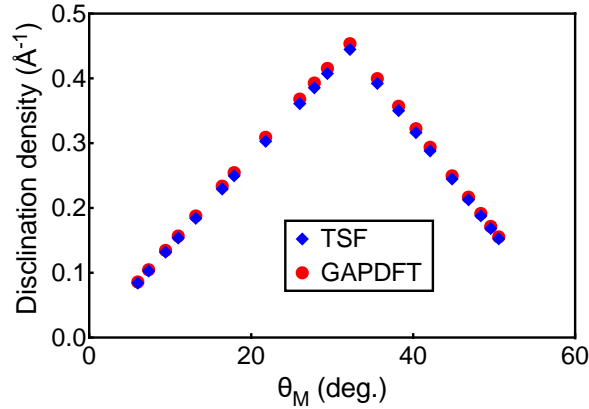


Figure 19 Density of disclination for selected 20 GBs relaxed with TSF and GAPDFT showing the maximum at the θ_M of around 35°.

In figure 21, we present the thermal resistance as a function of θ_M at various temperatures from the AGF and the Landauer formalism calculations. At high temperatures of 500 K and 1500 K in figures 21c and 21d, the thermal resistance has a concave shape with respect to θ_M , having a maximum resistance value at mid θ_M range. This behavior is similar to the case of Si and diamond at 1000 K that a previous study reports using molecular dynamics simulation with an empirical potential [104]. A common explanation for this behavior has been that the dislocation density is the maximum in the mid- θ_M and thus the phonon scattering by GBs is expected to be maximum in the mid- θ_M range. However, we observe different behaviors at low temperatures at 300 K and 100 K. At 300 K in figure 21b, the concave shape of thermal resistance becomes negligible and the resistance is nearly independent of the θ_M . As temperature further decreases to 100 K in figure 21a, the thermal resistance shows a convex shape with respect to θ_M , having the lowest thermal resistance at mid- θ_M . The behavior of thermal resistance at 100 K and 300 K is clearly opposite to the current understanding that the higher dislocation density leads to higher thermal resistance. For graphene GBs, the higher dislocation density does not necessarily lead to higher thermal resistance. In particular, at 100 K, the thermal resistance is even higher when the dislocation density is smaller.

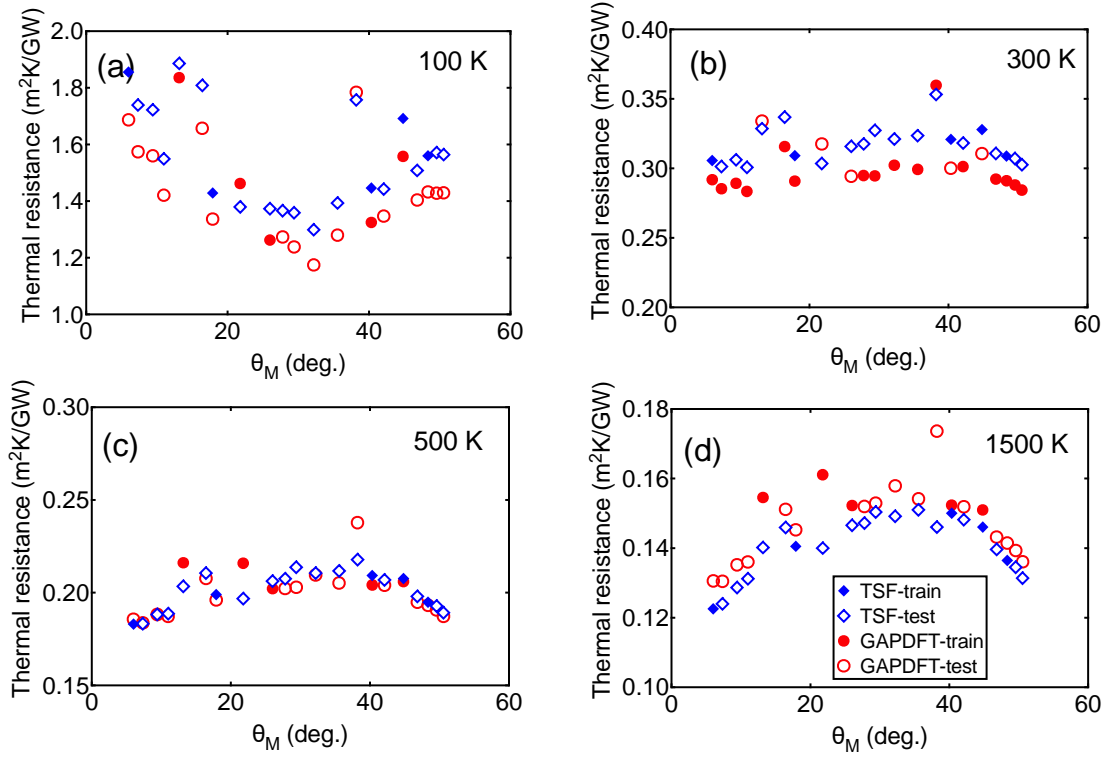


Figure 20 Thermal resistance with varying misorientation angles at (a) 100 K, (b) 300 K, (c) 500 K, and (d) 1500 K.

A possible explanation for this intriguing behavior of thermal resistance as a function of θ_M at different temperatures is that dislocation core and nearby strain field affect the phonon scattering by GBs to the different extents at different temperatures. At low temperatures, heat is mostly carried by long wavelength phonons which experience only weak scattering by dislocation cores since the wavelength is much longer than the characteristic size of the cores. The strain field can be a major contributor to the phonons scattering at low temperatures due to its spatially extended characteristics. This is supported by the fact that the strain energy distribution in figure 19c and the thermal resistance at 100 K in figure 21a have a similar trend with respect to θ_M ; both thermal resistance and strain energy are minimum in the mid- θ_M . At high temperatures where the short wavelength phonons are the major heat carriers, the wavelengths become comparable to the size of dislocation cores which thus cause strong scattering due to its nature of large lattice

distortion compared to the strain field. The thermal resistance at 500 K and 1500 K in figure 21 follow a similar trend as the core energy in figure 19b.

Observing the important role of the strain field for phonon scattering at low temperatures, we further investigate its detailed mechanisms. Figures 22a and 22b show the thermal conductance normalized by the ballistic thermal conductance of perfect graphene as a function of temperature. The normalization eliminates the specific heat effects from the conductance and thus shows how much the thermal conductance is suppressed by phonon scattering at a GB at various temperatures. The total 20 GBs can be clearly separated into two groups: one showing monotonously decreasing normalized thermal conductance as a function of temperature shown in figure 22a and the other showing increasing at low temperature and then decreasing normalized thermal conductance with temperature shown in figure 22b. It is interesting to see that most GBs of the first group are from mid- θ_M while the latter group is from the small and large θ_M . To explain the different behavior of the two GB groups, we consider spectral transmissivity defined as the phonon transmission function across a GB normalized by the ballistic phonon transmission function across single crystalline graphene. In figure 22c, we present the spectral transmissivity for the two GBs with θ_M of 6.02° and 32.20° that represent each group. In the frequency range below 15 THz which dominates the thermal transport below room temperatures, the two GBs show a remarkable difference. While the spectral transmissivity is high and nearly constant for the GB with $\theta_M=32.20^\circ$, the transmissivity for the GB with $\theta_M=6.02^\circ$ is low and increases rapidly with frequency. It is noteworthy that the majority of phonon states below 15 THz are from the flexural acoustic phonon branch due to the quadratic phonon dispersion and large density-of-states.

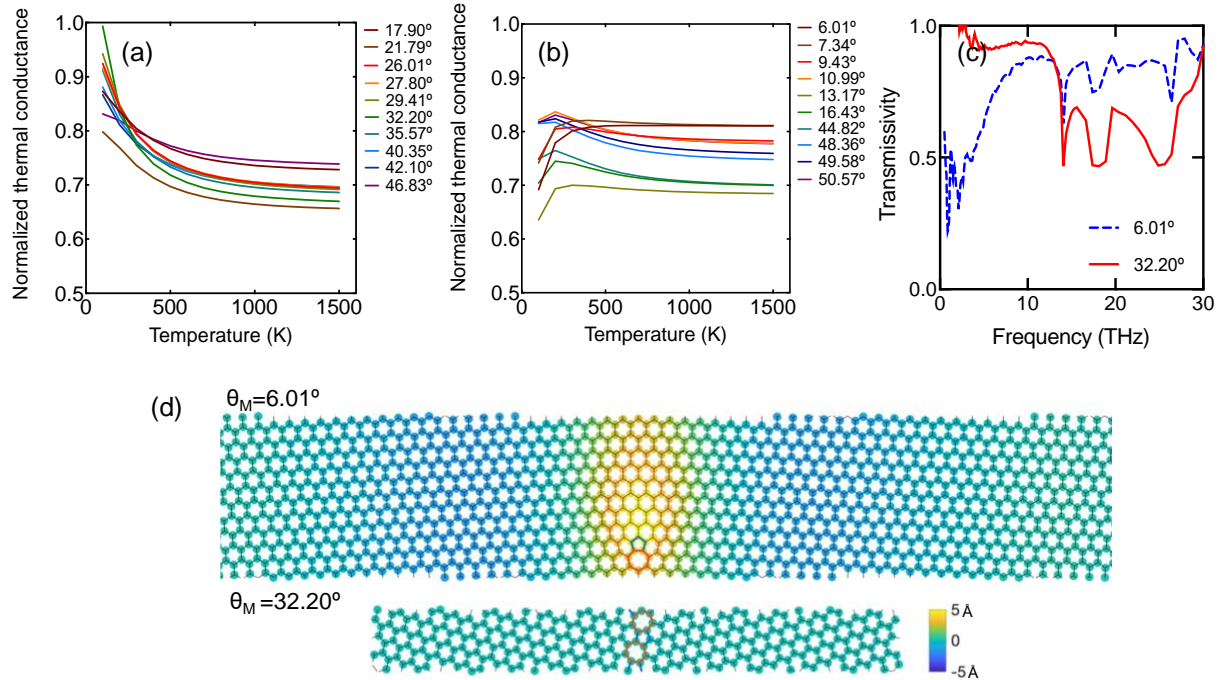


Figure 21 Role of out-of-plane buckling for scattering of flexural phonon modes. (a-b) normalized thermal conductance as a function of temperature for (a) GBs showing monotonously decreasing behavior and (b) GBs showing increasing behavior at low temperatures. The values in the legends represent misorientation angle. (c) Phonon transmissivity for two representative GBs showing a remarkable difference in low phonon frequency range below 15 THz. (d) Comparison of the two representative GBs in terms of out-of-plane buckling. The color represents out-of-plane displacement of atoms and the pentagon and heptagon are marked in blue and red, respectively.

The remarkably different scattering of flexural modes in the two GB groups is originated from the structural difference, in particular buckling induced by a GB. This is consistent with the previous studies [151, 152] that showed flexural modes are strongly scattered by buckling of GB structure. Previous study [151] reported the transmission reductions at low and high MA GBs exceed 40% and 20% respectively and could be as high as 80% for long wavelength phonons which are in the realm of low transmissivity values of our AGF results at long wavelength phonons due to buckling. Figure 22d shows that the two groups of GBs are very different in terms of out-of-plane buckling. The common disclinations in graphene, pentagon and heptagon, create

compression and dilation stress at the tips of disclinations, respectively. When a GB has low or high θ_M , the pentagon and heptagon disclinations are far from each other due to the low density of dislocations, and thus the out-of-plane buckling is induced to reduce the compressive and dilation strain. On the contrary, when a GB has a mid θ_M , the disclination cores are densely packed along the GB line with the pentagon and heptagon cores placed next to each other. In such a case, the compressive and dilation strain are canceled and the out-of-plane buckling does not occur [147]. Therefore, at low temperatures where the thermal phonon wavelength is comparable to the characteristic length of buckling, the significant buckling in GBs with low and high θ_M causes strong scattering of the flexural phonon modes. As a result, the GBs with low and high θ_M exhibit higher thermal resistance at 100 K than those with mid θ_M in figure 21a, although they have lower dislocation density.

Lastly, it would be interesting to present a brief comparison of GAPDFT and TSF since the TSF has been widely used in past studies while its accuracy for phonon transport across GBs has not been comprehensively examined. In figure 19, we compare GAPDFT and TSF for the GB formation, core, and strain energies. Figure 19a shows that the TSF overestimates the GB formation energy compared to the GAPDFT. This is because the core energy from TSF is larger than that from GAPDFT in the mid- θ_M range where the density of dislocation core is maximum as shown in figure 19b. On the contrary, for strain energy in figure 19c, the TSF and GAPDFT show similar predictions for the wide range of θ_M although the strain energy from TSF is slightly smaller. The comparison of the core and strain energy from TSF and GAPDFT indicates that TSF is reasonably accurate in predicting the energy of strained hexagon structure while poor in predicting the energy of severely distorted structures such as pentagons and heptagons.

The thermal resistances from TSF and GAPDFT in figures 21 are observed similar, but the force constants and spectral transmission functions behind the thermal resistance values are noticeably different for TSF and GAPDFT. For the self-interaction force constant in the crystalline phase, the TSF overpredicts by 35% compared to the GAPDFT (see figure 23). The force constant prediction by TSF has a more pronounced error in the core region of GBs.

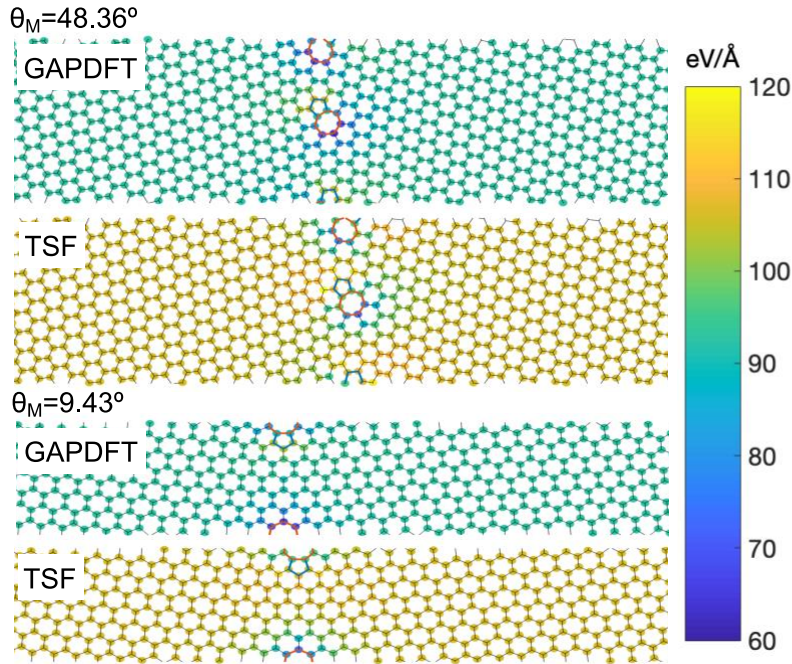


Figure 22 Comparison of magnitudes of self-interaction force constants from GAPDFT and TSF for a training structure with $\theta_M = 48.36^\circ$ and a test structure with $\theta_M = 9.43^\circ$. The difference between GAPDFT and TSF is as large as 35%.

In figures 24a and 24b, we present the error of TSF in predicting force constant change upon the introduction of GBs. We define the normalized error as $|\Delta\Phi_{ii,TSF} - \Delta\Phi_{ii,GAPDFT}| / \Delta\Phi_{ii,GAPDFT}$ where Φ_{ii} is a self-interaction force constant and $\Delta\Phi_{ii}$ is the difference of a self-interatomic force constant from the perfect crystalline case (i.e., $\Phi_{ii,GB} - \Phi_{ii,crystal}$). The figure shows that the error in the core region is pronounced and reaches up to 50% while the error is small for the surrounding

hexagons. This agrees with the aforementioned observation that the TSF has significant error for dislocations while is reasonably accurate for strained hexagons.

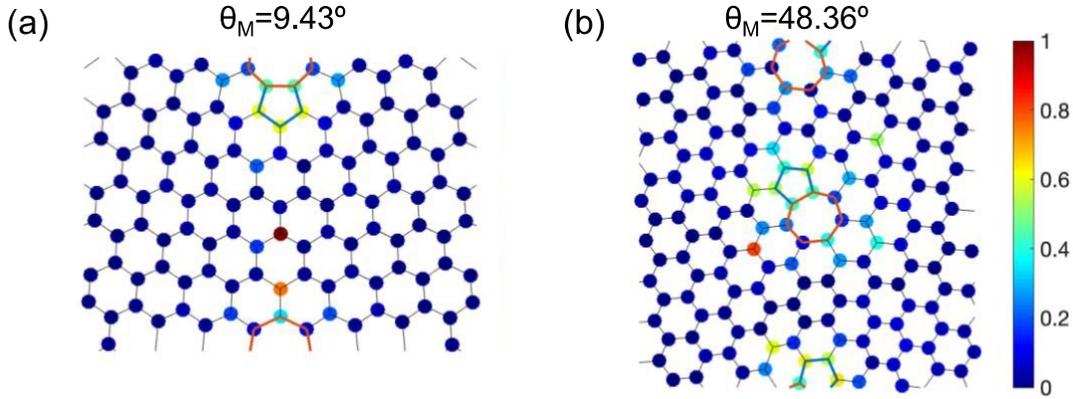


Figure 23 Comparison of TSF and GAPDFT showing inaccuracy of TSF for predicting force constants on dislocation cores. (a-b) normalized error of self-interatomic force constants, defined as $|\Delta\phi_{ii,TSF} - \Delta\phi_{ii,GAPDFT}|/\Delta\phi_{ii,GAPDFT}$ where $\Delta\phi_{ii}$ is the difference of self-interaction force constants in GB and perfect graphene.

As a result, the spectral transmissions from GAPDFT and TSF in figures 24a and 24b show substantial difference above 20 THz where dislocation cores are important for phonon scattering. Overall, the suppression of transmission functions from the perfect crystalline phase is noticeably larger in TSF than in GAPDFT, also supported by the overprediction of core energy by TSF in figure 19b. However, below 20 THz where the strain field is the dominant cause for phonon scattering, the GAPDFT and TSF show similar suppression of the spectral transmission function.

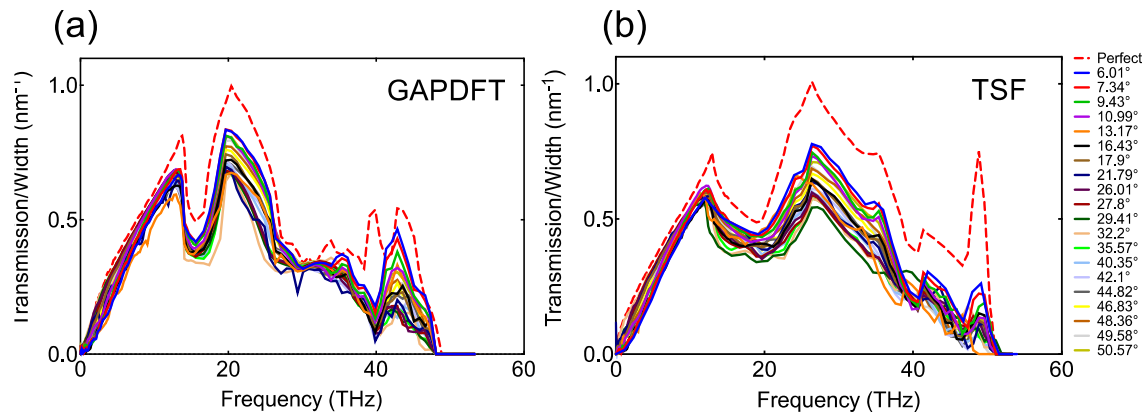


Figure 24 Comparison of TFS and GAPDFT showing inaccuracy of TFS for transmission function above mid phonon frequency. (a-b) suppressed transmission function from perfect graphene for 20 GBs. The values in the legend are misorientation angles.

4.4 Conclusion

In summary, we demonstrated that MLIPs trained with the rationally designed minimal dataset can predict phonon transport across GBs with ab initio predictive power and accuracy while the computational cost is affordable. Special attention was paid on reducing the required training dataset by employing the idea of structural unit model that GBs have hierarchical structures and have only a few basic building blocks. Our approach shows that only 5 GBs are enough to represent the entire configurational space and thus the small training dataset using those 5 GBs is sufficient for an MLIP. Indeed, our test using TFS and GAPDFT shows that force constants and spectral transmission functions from the TFS and GAPDFT are nearly identical for 20 GBs covering the entire configurational space.

The GAPDFT trained with the dataset from DFT reveals several intriguing characteristics of phonon scattering by GBs with ab initio accuracy. Previous studies for three dimensional bulk

materials suggested that thermal resistance increases with dislocation density, but we showed that graphene does not follow the same trend. The thermal resistance at room temperature does not depend on the dislocation density and even decreases with increasing dislocation density. We explained this with the two-dimensional structural characteristics of graphene: flexural phonon modes carrying the majority of heat and out-of-plane buckling induced by GBs. The heat-carrying flexural phonon modes are strongly scattered by the out-of-plane buckling which is pronounced for the GBs with low dislocation density. Thus, dislocation density alone cannot determine the scattering of phonons in polycrystalline graphene but the surrounding strain field plays an important role.

We also briefly examined the accuracy of TSF for thermal transport across GBs by comparing it to GAPDFT. The overall thermal resistance values from both TSF and GAPDFT reasonably agree with each other, but the force constants and spectral transmission functions show a noticeable difference. In particular, TSF shows inaccuracy in predicting dislocation cores (pentagons and heptagons) while is reasonably accurate for the strain field. As a result, the transmission functions from TSF agree with those from GAPDFT at low frequency where the strain field is important for phonon scattering, but shows noticeable error in the mid to high frequency range.

Our work provides deep insights into the atomic-level mechanisms governing phonon transport across graphene GBs, particularly for the buckling effects on phonon transmission and thermal resistance. This understanding may help to explain phonon transport across GBs in other two-dimensional materials and also to engineer their thermal properties using GBs. The present method for developing MLIPs with minimal training dataset can be easily extended to three dimensional materials. It would help to predict and understand thermal transport in the

polycrystalline phase of emerging materials for which a reliable interatomic potential has not been developed yet.

5.0 Mode Resolved Atomistic Green's Function

5.1 Bloch Wave

The mode matching scheme was first introduced to calculate the transmission function of electrons along with the periodic medium [153]. The approach is based on the Bloch theorem which states that the wavefunction can be written as Bloch waves of spatially periodic solution in a periodic medium. Hence the Bloch wave can be decomposed to an eigenfunction that repeats in unit cells and plane wave as shown as

$$u(\mathbf{r}) = \bar{u}(\mathbf{r})\exp(i\omega t)\exp(i\mathbf{k}\mathbf{r}) \quad 5-1$$

where $\bar{u}(\mathbf{r})\exp(i\omega t)$ is the wavefunction and $\exp(i\mathbf{k}\mathbf{r})$ is the plane wave. Schematic representation of the Bloch wave decomposition is shown in figure 26 where one mode with two wavefunctions and different plane waves are demonstrated

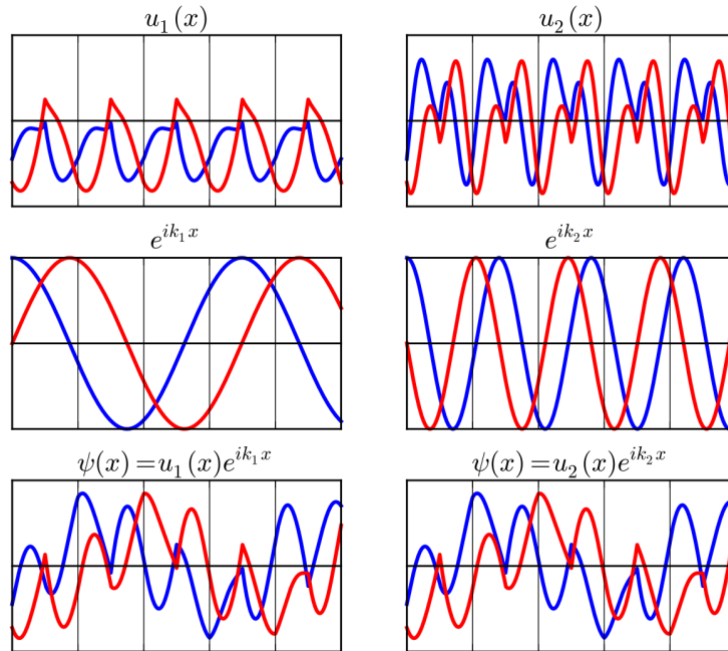


Figure 25 A Bloch wave (bottom) can be decomposed into the product of a periodic function (top) and a plane wave (center). The left side and right side represent the same Bloch wave broken up in two different ways, involving the wave vector k_1 (left) or k_2 (right). In all plots, blue is real part and red is imaginary part.[154]

5.2 Mode Matching Approach

We first discuss the original mode matching implementation and then we incorporate Green's function into the mode-matching approach. Figure 27 shows the schematic view of the divided units for the system of the device with periodic contacts

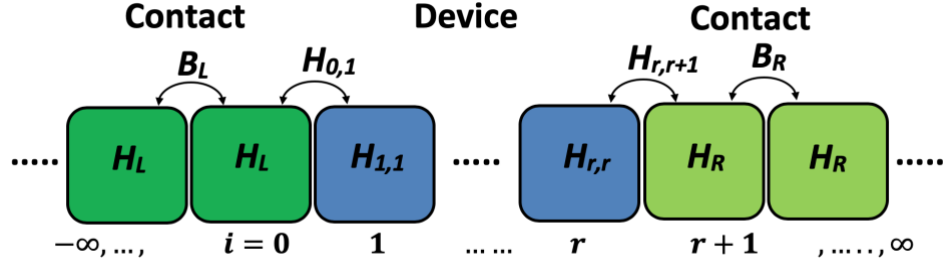


Figure 26 Schematic view of the device with two semi-infinite contacts which are divided into Bloch units

Here we derive the dynamical equation of a unit i th about the contact where the contact units are periodic. The Hamiltonian dynamical equation is given as

$$-H_{i,i-1}u_{i-1} + (\omega^2 I - H_{i,i})u_i - H_{i,i+1}u_{i+1} = 0 \quad 5-2$$

where u_i is the displacement of the unit i and u_{i-1} , and u_{i+1} are the displacements of the units $i + 1$, and $i - 1$ respectively. Based on the Bloch theorem, u_{i-1} , and u_{i+1} displacements have the same wavefunction with a phase difference. In the case of equisized unit division (equispaced), the phase difference is a constant number and is called the Bloch factor (λ). Thus, the neighboring displacements can be represented as $u_{i+1} = \lambda u_i$ and $u_{i-1} = \lambda^{-1} u_i$. We call $H_{i,i}$ “on-slice” Hamiltonian matrix that includes the force constants and effective masses of the isolated unit and we call $H_{i,i-1}$ and $H_{i,i+1}$ “hopping” Hamiltonian matrices that include the coupling force constants and effective masses of interacting neighbors of i th unit. The middle term represents the interaction of the atomistic model within the unit i and left and right terms refer to the coupling interaction with the neighboring left and right units respectively. For the sake of simplicity, we change the notation slightly for hopping Hamiltonian matrices such that $B_{L/R}$ and $B_{L/R}^\dagger$ are corresponding to $H_{i,i-1}$ (left Hamiltonian matrix) and $H_{i,i+1}$ (right Hamiltonian matrix) respectively. Therefore, the equation 5-2 is rewritten as

$$-B_{L/R}u_{i-1} + (\omega^2 I - H_{i,i})u_i - B_{L/R}^\dagger u_{i+1} = 0 \quad 5-3$$

which is true for all the units of $i = -\infty, \dots, 0$ and $i = r + 1, \dots, \infty$. Now we aim to derive this equation such that the solution from Bloch wave calculation is relevant. Hence, we substitute the set of Bloch waves into the equation 5-3 for each Bloch mode as

$$-B\lambda_n^{-1}\bar{u}_n(\pm) + (\omega^2\mathbf{I} - H_{i,i})\bar{u}_n(\pm) - B^\dagger\lambda_n\bar{u}_n(\pm) = 0 \quad 5-4$$

where $\bar{u}_n(\pm)$ is the right going or left going wavefunctions and λ_n is the Bloch factor of the n th mode of the unit i . Here we drop the subindices of L/R for simplification while the equation is valid for both left and right contacts. If we consider that a dual wavefunction, \tilde{u} , is available such that $\tilde{u}_m(\pm)\bar{u}_n(\pm) = \delta_{n,m}$; then we can project the equation 5-4 into the dual wavefunction (transpose conjugate of the wavefunction) where the result is

$$-B\lambda_n^{-1}\bar{u}_n(\pm)\tilde{u}_n(\pm) + (\omega^2\mathbf{I} - H_{i,i})\bar{u}_n(\pm)\tilde{u}_n(\pm) - B^\dagger\lambda_n\bar{u}_n(\pm)\tilde{u}_n(\pm) = 0 \quad 5-5$$

This new formulation is beneficial since contains the information of the probability density as well as the Bloch factor which includes the spatial information. Therefore, it is reasonable to define the Bloch matrix as $F_n^i = \lambda_n^i\bar{u}_n\tilde{u}_n$ and re-write the equation 5-5 in terms of F as

$$-BF^{-1}(\pm) + (\omega^2\mathbf{I} - H_{i,i}) - B^\dagger F(\pm) = 0, \quad 5-6$$

we should note that the Bloch matrices have a direct relation with the displacements where the solution for the displacement can be obtained as

$$u = u_i(+) + u_i(-) = F^{i-j}(+)\bar{u}_j(+) + F^{i-j}(-)\bar{u}_j(-). \quad 5-7$$

Up to here, we obtained the equation based on the Bloch matrices which is simple and relevant for any unit of the periodic contacts and we showed the relation for the displacement with the Bloch matrix solution. Now we use the solutions from contacts to calculate the dynamical equation of the device. If the solutions for the contacts are available, then we can use them as boundary conditions to find the solution of the device. We remind that the wavefunctions are transmitting from left contact to right contact. Therefore, the boundary conditions of the device using the relation 5-7 for the unit of -1 is set to be

$$\begin{aligned}
u_{-1} &= F_L^{-1}(+)u_0(+) + F_L^{-1}(-)u_0(-) \\
&= [F_L^{-1}(+) - F_L^{-1}(-)]u_0(+) + F_L^{-1}(-)u_0
\end{aligned} \tag{5-8}$$

and the boundary condition for the right side of the device is set to be

$$u_{r+1} = F_R(+)u_{r+2}(+) \tag{5-9}$$

The equation 5-2 is only valid for the contacts and in order to derive the dynamical equation of the device, we need to incorporate the boundary conditions into a similar system of equations. Here we generalize the equation 5-2 in the form that is valid for both contact and device. If the device is a periodic medium, similar to the contacts, it can be divided into equisized units where the indices are $i = 0, \dots, r$. The compact modified version of equation 5-2 is given as

$$-H'_{i,i-1}u_{i-1} + (\omega^2 I - H'_{i,i})u_i - H'_{i,i+1}u_{i+1} = Q_i u_0(+) \tag{5-10}$$

where the $H'_{i,i}$ now is the on-slice Hamiltonian matrix of device or contacts. The indices of the equation represent the divided units of device or contacts and its arrangement is shown in figure 26. The Q_i represents the source term of energy that only takes the values for the device. If we follow the same process as discussed earlier, we can write the equation 5-10 based on the Bloch matrix as

$$-H'_{i,i-1}F^{-1} + (\omega^2 I - H'_{i,i}) - H'_{i,i+1}F = Q_i \tag{5-11}$$

and using the relations 5-8 and 5-9, the modified Hamiltonian matrices and source term are calculated as

$$\begin{aligned}
H'_{0,0} &= H_L + B_L F_L^{-1}(-) \\
H'_{r+1,r+1} &= H_R + B_R^\dagger F_R^{-1}(+) \\
Q_0 &= B_L [F_L^{-1}(+) - F_L^{-1}(-)] \\
Q_i &= 0 \quad i \neq 0
\end{aligned} \tag{5-12}$$

The details of the calculations are provided in appendix A. It is worth mentioning to recall that all the calculations are done based on the left to right transmission direction. Therefore, for instance, if we consider an incoming wave of $u_0 = \bar{u}_{L,m}$ transmitting through the device from left

contact to the right contact, the transmission coefficient can be calculated using the right-side boundary condition of the device as

$$u_{r+2} = \sum_{n=1}^N \bar{u}_{R,n}(+) \tau_{n,m} \quad 5-13$$

Here the $\tau_{n,m}$ is n th mode transmission coefficient of right going wave which is generated from the m th mode of the wavefunctions on the left contact. u_{r+2} is the solution of the boundary condition on the right contact of the device and $\bar{u}_{R,n}$ represents the outgoing/right-going wavefunction on the right contact. A summary of the calculations for the mode-matching approach is as follows:

1. Calculate the system of equations (equation 5-6 or 5-11) for left and right contacts to find $F_{L/R}$
2. Calculate the Hamiltonian matrices and source term of a device based on left and right boundary conditions
3. Calculate the system of equations (equation 5-11) for the device
4. Calculate the mode resolved transmission and the displacements

Next, we will show the physical interpretation of the Bloch matrix and discuss the correlation between the Bloch matrix and the wavevector.

5.3 Bloch Theorem and Bloch Matrix

We already showed that the general equation describes the device and contacts based on the divided units and Bloch matrices. In addition to a simple representation of the dynamical matrix, here we show the importance of the Bloch matrix for the calculation of the wavevectors.

In a concise definition, the Bloch matrix is the projection of the wavefunction and its dual vector with the Bloch factor. The Bloch factor is a phase factor which for equisized and equispaced units becomes a constant. The general form of the Bloch matrix is given as

$$F = \sum_{n=1}^N \lambda_n \bar{u}_n \tilde{u}_n \quad 5-14$$

If we stack the modes into a single vector for both wave functions and Bloch factors, we can then show the Bloch matrix as

$$F = \mathbf{\Lambda} \bar{\mathbf{U}} \tilde{\mathbf{U}} \quad 5-15$$

where $\mathbf{\Lambda}$ ($\Lambda_{n,m} = \lambda_n \delta_{n,m}$) includes all the Bloch factors for all the orthogonal modes and $\bar{\mathbf{U}}$'s are the stacked wavefunctions. When the solution for the Bloch matrix is calculated with a dynamical system, then the information could translate to the wavefunctions and Bloch factor. For each Bloch matrix, an eigenvalue problem can be written that the eigenvalues are the Bloch factors and the eigenfunctions are the wavefunctions of the sliced unit. The Bloch eigenvalue problem is shown as

$$F(\pm) \bar{\mathbf{U}}(\pm) = \mathbf{\Lambda}(\pm) \bar{\mathbf{U}}(\pm) \quad 5-16$$

Once the Bloch factor, $\mathbf{\Lambda}$, is obtained, the modes which are defined for left and right contacts and self-advance and retarded are calculated with independent eigenvalue problems as following

$$F_{R/L}^{\text{ret/adv}}(\pm) \bar{\mathbf{U}}_{R/L}^{\text{ret/adv}}(\pm) = \mathbf{\Lambda}_{R/L}^{\text{ret/adv}}(\pm) \bar{\mathbf{U}}_{R/L}^{\text{ret/adv}}(\pm) \quad 5-17$$

where superscripts differentiate the retarded and self-advance solutions and subindices differentiate the right and left contacts. The solutions provide a set of modes which are propagating or evanescent in the left and right contacts. Propagating modes are the ones that are growing toward the source and evanescent modes are the ones which are decaying toward the source. The conditions to describe the type of modes are summarized as

$$\begin{aligned}
\lambda_n^{\text{ret}}(\pm) &= \lambda_n^{\text{adv}}(\mp); \quad \bar{u}_n^{\text{ret}}(\pm) = \bar{u}_n^{\text{adv}}(\mp) \text{ for} \\
&\quad \text{propagating} \\
\lambda_n^{\text{ret}}(\pm) &= \lambda_n^{\text{adv}}(\pm); \quad \bar{u}_n^{\text{ret}}(\pm) = \bar{u}_n^{\text{adv}}(\pm) \text{ for} \\
&\quad \text{evanescent}
\end{aligned}
\tag{5-18}$$

If the Bloch factors or eigenvalues for retarded and self-advance move into the opposite directions, then the modes are propagating waves and vice versa condition is the evanescent mode. This shows that the Bloch matrix is the implication of bulk translational symmetry along the transmission direction. When the Bloch factors are found; the wavevectors of propagating modes are then calculated with

$$\begin{aligned}
\lambda_{n_{R/L}} &= [\Lambda_{R/L}(\pm)]_{n,n} = \exp(ik_n a_{R/L}) \\
k &= \frac{1}{a_{R/L}} \cos^{-1} \text{Re} [\lambda_{n_{R/L}}]
\end{aligned}
\tag{5-19}$$

where a is the size of a divided unit of left or right contact and k is the wavevectors corresponding to the eigenvalue of the n th mode. This concludes the importance of the mode-matching approach to find the spatial and wavevector information. For a periodic model, the mode-matching approach significantly reduces the computational cost while remaining deficient for non-periodic models.

For AGF simulation of the non-periodic device with two contacts, the periodic contacts can be decomposed into plane waves and eigenfunctions using the mode-matching approach. Therefore the combination of mode-matching approach and atomistic Green's function (MAGF) was proposed to resolve the lack of wavevector resolution in AGF [155]. In MAGF, we consider similar assumptions to AGF where the device is sandwiched by two periodic and semi-infinite size contacts. Additionally, we divide the periodic medium into the periodic units where the Bloch waves are defined for each unit. Here it is assumed that the divided units have the same length and they are large enough that only interact with their neighboring units.

5.4 Combined Approach: Mode-matching Approach with Green's Function Solution

In this section, we aim to combine the mode-matching approach with Green's function. Our objective is to deal with the device and two contacts where the device is a non-periodic or a periodic medium. We pursue a similar process to the mode-matching approach, however, here we utilize Green's function to solve Bloch matrices of the dynamical system. The details of derivations are given previously and we continue to build on those formulations with the same notation. We initiate with the dynamical equation based on Bloch matrices for the contact as

$$-H'_{i,i-1}F^{-1} + (\omega^2\mathbf{I} - H'_{i,i}) - H'_{i,i+1}F = 0 \quad 5-20$$

similar to the definition of the divided units and Hamiltonian matrices, the Green's function can be divided into the number of Green's functions submatrices where each is defined as the inverse of a unit operator. If we apply this methodology to the equation 5-14, the relevant Green's functions equation will be obtained in which that represents the response of the unit i upon the excitation which is located at the unit j . The general form of Green's function equation for device and contacts is given as

$$-H'_{i,i-1}G'_{i-1,j} + (\omega^2\mathbf{I} - H'_{i,i})G'_{i,j} - H'_{i,i+1}G'_{i+1,j} = \mathbf{I}\delta_{i,j} \quad 5-21$$

Here we show the Green's function as G' to indicate that the response function can be divided into the isolated and the connected/coupled units. The $G'_{i,j}$ is the response function that the isolated unit i sees upon excitation at unit j and the $G'_{i-1,j}$ and $G'_{i+1,j}$ are the response functions of the units $i - 1$ and $i + 1$ upon excitation at unit j . Similar to the mode-matching approach, we assume that the transmission is right going from left contact to right contact. For right contact, the displacement solution can be expanded in terms of Green's function and source term which is initiated/executed at unit 0 from left contact. The expansion of displacements at unit i is given as

$$u_i = G'_{i,0}(+)Q_0(+)u_0(+) \quad 5-22$$

If we use the relation 5-13, we can find the elements of transmission matrix or namely modal transmittance as

$$\tau_{n,m} = \tilde{u}_{R,n}(+)G'_{r+1,0}(+)Q_0(+)\bar{u}_{L,m}(+) \quad 5-23$$

Next, we use a recursive calculation to solve Green's functions of contacts. For instance, the divided Green's function of left contact for units $i = -\infty, \dots, n$ where n is an arbitrary unit number below 0 is defined as $G'_{i,j} = G_{i,j}^{[k]}$ where the subindices i, j are the responsive and excitative unit indices respectively while the super indices $[k]$ shows the recursive sequence. If we apply a similar process for the calculation of the surface Green's function for contact here, then the Green's function of the left contact is derived as

$$\left[\omega'^2 \mathbf{I} - H_{n+1,n+1} - H_{n+1,n} G_{n,n}^{[n]}(\omega'^2) H_{n,n+1} \right] G_{n+1,n+1}^{[n+1]}(\omega'^2) = \mathbf{I} \quad 5-24$$

The solution is similar to what is solved from the decimation technique where the recursive Green's function, in the ideal case, will converge to the surface Green's function, therefore $g_L = G_{n,n}^{[n]}$ and $g_L = G_{n+1,n+1}^{[n+1]}$. We should note that the choice of n is important, n should be large enough that the convergence occurs within the ascending recursive calculation. Thus, we can write the solution for surface Green's function in a simplified fashion of

$$\left[\omega'^2 \mathbf{I} - H_L - B_L g_L(\omega'^2) B_L^\dagger \right] g_L(\omega'^2) = \mathbf{I} \quad 5-25$$

here H_L is the on-slice Hamiltonian, $H_{n+1,n+1}$ in equation 5-18, and B_L is the hopping Hamiltonian matrix, $H_{n+1,n}$ in equation 5-24. In a similar way, we can calculate the surface Green's function for right contact which is

$$\left[\omega'^2 \mathbf{I} - H_R - B_R g_R(\omega'^2) B_R^\dagger \right] g_R(\omega'^2) = \mathbf{I} \quad 5-26$$

we just note that the recursive process for the right contact in contrast to the left contact is a descending process. Now the solutions for the surface Green's functions are calculated, we can find the self-energies as

$$\Sigma_L = B_L g_L(\omega'^2) B_L^\dagger; \quad \Sigma_R = B_R^\dagger g_R(\omega'^2) B_R \quad 5-27$$

we use these self-energy terms as boundary conditions for the device to calculate the coupled Green's function.

In an ideal case for infinitely large contact where n is also considered to be large, the modified version of equation 5-20 turns to

$$-B_{R/L}^{\dagger} F_{R/L}^{-1}(\pm) + (\omega^2 I - H_{R/L}) - B_{R/L}^{\dagger} F_{R/L}(\pm) = 0 \quad 5-28$$

Accordingly, the recursive Green's function of an ideal contact is represented as

$$-B_{R/L}^{\dagger} G_{i-1,j}^{[n]} + (\omega^2 I - H_{R/L}) G_{i,j}^{[n]} - B_{R/L}^{\dagger} G_{i+1,j}^{[n]} = I \delta_{i,j} \quad 5-29$$

Using the similar recursion relation as 5-7, we can write the recursion Green's function based on the Bloch matrices as

$$\begin{aligned} G_{i,j}^{[n]}(\omega^2) &= F^{i-j}(-) G_{j,j}^{[n]}(\omega^2), \quad i < j \\ G_{i,j}^{[n]}(\omega^2) &= F^{i-j}(+) G_{j,j}^{[n]}(\omega^2), \quad i > j \end{aligned} \quad 5-30$$

For the diagonal elements of $G_{i,j}^{[n]}$ ($i = j$), if we incorporate the relation 5-30 into the equation 5-29, then we get

$$\left(\omega'^2 I - H_{R/L} - B_{R/L}^{\dagger} F_{R/L}(+) - B_{R/L}^{\dagger} F_{R/L}^{-1}(-) \right) G_{i,j}^{[n]} = I \quad 5-31$$

If we combine this equation with the previous equation in order to find the substitution for $\omega'^2 I - H_{R/L}$, then the diagonal elements of Green's function become as

$$\left[G_{j,j}^{[n]}(\omega^2) \right]^{-1} = B_{R/L}^{\dagger} \left[F_{R/L}^{-1}(+) - F_{R/L}^{-1}(-) \right] \quad 5-32$$

or equivalently

$$\left[G_{j,j}^{[n]}(\omega^2) \right]^{-1} = B_{R/L}^{\dagger} \left[F_{R/L}(-) - F_{R/L}(+) \right] \quad 5-33$$

Similar relations for the self-advance Bloch matrices can be derived. Now once the solution for the ideal and infinitely large contacts are defined, we implement the problem for a system of the device with two semi-infinitely large contacts where the surface Green's function is calculated. In this case, the surface Green's function is the closest recursion Green's function to the device, for instance for left contact is $g_L(\omega^2) = G_{0,0}^{[n]}(\omega^2)$. Using equation 5-23, we can write the equation for Green's function calculation of left contact with semi-infinite size as

$$\left(\omega'^2 \mathbf{I} - H_L - B_L^\dagger F_L^{-1}(-)\right) g_L = \mathbf{I} \quad 5-34$$

We should note that the right going wave is absent here because the contact has a semi-infinite size and is blocked on the right side. A similar equation can be written for the neighboring unit of $i = -1$, and $j = 0$ using the surface Green's function as

$$\left(\omega'^2 \mathbf{I} - H_L - B_L^\dagger F_L^{-1}(-)\right) F_L^{-1}(-) g_L = B_L^\dagger g_L \quad 5-35$$

by comparing two equations 5-34 and 5-35, we can find the surface Green's function based on the Bloch matrix

$$g_L = F_L^{-1}(-) (B_L^\dagger)^{-1} \quad 5-36$$

In a similar fashion, recursion Green's functions for $i = -\infty, \dots, -1$ can be calculated based on the Bloch matrix with left going or right going waves. The final relations for recursion Green's function of left contact and in the ideal case are given as

$$\begin{aligned} G_{i,0}^{[n]} &= F_L^{i+1}(-) (B_L^\dagger)^{-1} \\ G_{i,0}^{[n]} &= F_L^{i+1}(+) (B_L)^{-1} \end{aligned} \quad 5-37$$

A similar process could take place for the right contact and recursion Green's function can be calculated. Furthermore, it is easy to show that the self-energy terms are defined based on the Bloch matrices. Here are the definitions of the self-energies of left and right contacts

$$\Sigma_L = B_L F_L^{-1}(-) \quad 5-38$$

$$\Sigma_R = B_R^\dagger F_R(+)$$

these relations point out to the major advantage of the combined approach where once the Bloch matrices are calculated, then the calculations for many terms such as surface Green's functions and self-energy are rather straightforward.

Next is to use the contacts information in order to find the solution for the device. The dynamical system for the device or in general form is given as

$$-H''_{i,i-1}G'_{i-1,j} + (\omega^2 I - H''_{i,i})G'_{i,j} - H''_{i,i+1}G'_{i+1,j} = I\delta_{i,j} \quad 5-39$$

similarly, the Hamiltonian matrices are defined based on the surface Green's functions of the left and right contacts. The abbreviated Hamiltonian matrices and source term relations of equation 5-39 are

$$\begin{aligned} H''_{0,0}(\omega'^2) &= H_L + B_L g_L(\omega'^2) B_L^\dagger \\ H''_{r+1,r+1} &= H_R + B_R^\dagger g_R(\omega'^2) B_R \\ Q_0 &= B_L [F_L^{-1}(+) - F_L^{-1}(-)] \end{aligned} \quad 5-40$$

The calculation is similar to appendix A for the mode-matching approach. Up to this point, we have demonstrated that the solution for the Bloch matrices and Green's functions of the entire device and contacts. Next, we are going to draw a connection between the displacements and the transmission matrix.

5.5 Transmission Matrix and Transmission Coefficient

The transmission matrix is a physical matrix with the elements that are found by normalizing the modal transmission which was discussed earlier in equations 5-13. Transmission matrix is defined as

$$t_{n,m} = \sqrt{\frac{v_{R,n}(+)a_L}{v_{L,m}(+)a_R}} \tau_{n,m} \quad 5-41$$

where $v_{R,n}$ and $v_{L,m}$ are called Bloch velocities or mode resolved group velocities, also a_L and a_R are the left and the right length of each unit. The modes m and n are related to the left and right contacts respectively. The transmission matrix indicates how probable is that waves propagate from right to left contacts. Then the total transmission probability of propagating modes is given by

$$T(E) = \sum_{n,m}^{(+)} |t_{n,m}|^2 \quad 5-42$$

which is a summation of all the elements of the transmission matrix (trace of transmission matrix). The transmission matrix also can be obtained by Green's function and Bloch matrix. In order to do that, we need to find the relation between displacement and Green's function. We begin with the equation known as the Lippmann-Schwinger equation given by

$$\begin{aligned} u_i &= \bar{u}_{L,m,i}(+) + \sum_{j,k} G_{i,j} V_{j,k} \bar{u}_{L,m,k}(+) \\ &= \left[F_L^i(+) + \sum_{j,k} G_{i,j} V_{j,k} F_L^k(+) \right] \bar{u}_{L,m}(+) \end{aligned} \quad 5-43$$

where u_i known as the displacement of the unit i are divided into two portions. The first portion, $\bar{u}_{L,m,i}(+)$, represents the wavefunction which obeys the Bloch symmetry (and periodicity) and the second portion indicates the perturbed displacement. $V_{j,k}$ is the perturbation matrix and $G_{i,j}$ is the Green's function which is projected into the perturbation matrix. The second portion indicates the non-equilibrium nature of the displacement in terms of time evolution. This relation (5-43) was derived from the combination of perturbation theory and the Kubo approach. The wavefunction $\bar{u}_{L,m,i}$, also can be translated with the Bloch matrix such that $\bar{u}_{L,m,i} = F_L^i(+) \bar{u}_{L,m}$. The second

relation shows the incorporation of Bloch matrices into the Lippmann-Schwinger equation. Furthermore, the equation 5-43 can be simplified by the Dyson equation which results in the equation for the Green's function calculation as following

$$G_{i,0} = G_{i,0}^{(0)} + \sum_{j,k} G_{i,j} V_{j,k} G_{k,0}^{(0)} = \left[F_L^i(+) + \sum_{j,k} G_{i,j} V_{j,k} F_L^k(+) \right] G_{0,0}^{(0)} \quad 5-44$$

If we compare the equations 5-44 and 5-43 and use the relation 5-30, then we can easily find the source term as

$$u_i = G_{i,0}(E) \left[G_{0,0}^{(0)}(\omega^2) \right]^{-1} \bar{u}_{L,m}(+) \quad 5-45$$

$$Q_0 = \left[G_{0,0}^{(0)}(\omega^2) \right]^{-1}$$

and from relation 5-13, the generalized form of modal transmittance is obtained as

$$\tau_{n,m} = \tilde{u}_{R,n}(+) G_{r+1,0}(E) \left[G_{0,0}^{(0)}(\omega^2) \right]^{-1} \bar{u}_{L,m}(+) \quad 5-46$$

This is explicit relation for the modal transmittance or elements of the transmission matrix.

5.6 The Caroli Expression

In regard to Green's function approach, the transmission function is calculated using Caroli expression[92, 156]. Following the same notation as previous sections, the Caroli expression is given by

$$T = \text{Tr} \left[\Gamma_R G_{0,r+1} \Gamma_L G_{r+1,0}^\dagger \right] \quad 5-47$$

here the Γ 's are the escape rate or leakage of the self-energy terms which fundamentally point to the non-equilibrium aspect of Green's function approach; they are defined as

$\Gamma_{R/L} = i[\Sigma_{R/L} - \Sigma_{R/L}^\dagger]$. The Caroli expression is derived from the Kubo-Greenwood formula in the linear response regime. The expression is equivalent to the transmission coefficient in the Landauer formula as well. Physically it calculates the response on contact from an excitation on a distanced location and the normalized response counts for the transmission probability. Here we are going to expand the Caroli expression based on the transmission matrix.

As we discussed earlier the total transmission probability of the propagating modes is given in relation 5-47. Moreover, we can generalize the transmission probability that includes all the propagating and evanescent modes by defining the probability matrix as

$$t = V_R^{0.5}(+) \tau \tilde{V}_L^{0.5}(+) \quad 5-48$$

here the probability matrix is given for the right going wave and V 's are the mode group velocities of left and right contact. Mode group velocity is a diagonal element of the group velocity. For the right going propagating waves, the mode group velocity of right contact, $V_R(+)$, is the velocity $v_{R,n}$ times $(a_R)^{-1}$ and for evanescent waves, the mode group velocity of right contact is zero. Likewise, for the left going waves and left contact, the pseudoinverse mode group velocity \tilde{V}_L is velocity $1/v_{L,n}$ times a_L . If the solution for eigenvalues of the Bloch matrices is available, we can find an expression for the mode group velocities of left and right contacts. The general form of the Bloch velocity matrix is given by (the derivation is provided in appendix B)

$$V(\pm) = i[U^\dagger(\pm)B^\dagger U(\pm)\Lambda(\pm) - \Lambda^\dagger(\pm)U^\dagger(\pm)BU(\pm)] \quad 5-49$$

This relation can be expanded based on the Bloch matrices and hopping Hamiltonian matrices as shown below for the right contact mode group velocity of right going waves

$$\begin{aligned} V_R(+) &= iU_R^\dagger(+)[B_R^\dagger F_R(+) - F_R^\dagger(+)B_R]U_R(+) \\ &= iU_R^\dagger(+)[\Sigma_R(+) - \Sigma_R^\dagger]U_R(+) \\ &= U_R^\dagger(+) \Gamma_R U_R(+) \end{aligned} \quad 5-50$$

similar relation can be written for the left contact as

$$V_L(+) = U_L^{a\dagger}(-)\Gamma_L U_L^a(-) \quad 5-51$$

These two relations mean the leakage on the left and right contacts are projected into the propagating states of each contact. For left contact, propagating waves are the result of reflection, therefore the wavefunctions are the self-advance left going waves. For right contact, propagating modes are propagating right going as retarded wavefunctions of the right contact.

Now we recall the transmission relation 5-50 which is given as

$$\tau_{n,m} = \tilde{u}_{R,n}(+)G_{r+1,0}(E)\left[G_{0,0}^{(0)}(\omega^2)\right]^{-1}\tilde{u}_{L,m}(+) \quad 5-52$$

If we mix relation 5-48, 5-52 and $V_L\tilde{V}_L^{0.5} = V_L^{0.5}$, then we get the following relation for transmission matrix in a compact form of

$$t = iV_R^{0.5}(+)U_R^{-1}(+)G[U_L(-)]^{-1}V_L^{0.5}(+) \quad 5-53$$

Additionally, the relation 5-42 can be expressed as

$$T = \text{Tr}[t^\dagger t] \quad 5-54$$

and by inserting the relation 5-48, the total transmission probability based on the mode group velocities become

$$T = \text{Tr}[\tau^\dagger V_R(+)\tau\tilde{V}_L(+)] \quad 5-55$$

this is called transmission matrix which its elements are known as modal transmittance and they can be calculated as

$$t_{n,m} = 2i\omega \sqrt{\frac{v_{R,n}v_{L,m}}{\alpha_L\alpha_R}}\tilde{u}_{R,n}(+)G_{r+1,0}(E)\tilde{u}_{L,m}(-) \quad 5-56$$

which is a simplified form of the relations 5-41 and 5-46 in conjunction with flux-normalized factors. This concludes our calculation for modal transmittance and information that we would need to calculate when the transmission process is from left to right contact. All the calculations in this section could also be done in the reversed direction when the transmission process is from right to left contact.

5.7 Remarks

1. The results of eigenvalue problems are not necessarily orthonormal and particularly near the degenerate points of dispersion due to complex eigenvalues (nonequilibrium). Therefore, we use the Gram-Schmidt process to resolve the issue of orthonormality of Bloch states and we use QR decomposition to assure that we have the orthonormal set of Bloch states near the degenerate points (we will discuss them in appendix C).
2. We observed that for large eigenvalue problem of Bloch waves, the Bloch states are deeply ill-posed and non-orthogonal. We discovered singular value decomposition (SVD) on the set of Bloch states will remedy the ill-condition. We should note, in this case, the inverse Bloch states is equivalent of the conjugate transpose of the Bloch states.
3. There are multiple ways to calculate the modal transmittance and transmission matrix.
4. The conditions to determine the propagating states are described in Appendix D.

The full summary of the calculations for MAGF is as follows:

1. Using original AGF, calculate surface Green's functions, hopping and on-slice Hamiltonian matrices, and self-energy terms
2. Create four independent systems of equations for Bloch matrix calculations (retarded and self-advances for right and left contact) based on surface Green's function and hopping matrices (equations 5-36 & 5-37)
3. Solve the eigenvalue problems in step 2 in order to find the Bloch states and Bloch factors
4. Use Gram-Schmidt, QR decomposition, and SVD to orthonormalize the Bloch states and solve the eigenvalue crossing issue near the degeneracy occurrence.

5. Use the Bloch states to calculate the Bloch velocities (equations 5-51 & 5-52) and modal transmittance (equations 5-53 or 5-56)
6. Find the wavevectors for the propagating Bloch waves (equation 5-19 and appendix D)

5.8 Verifications

We developed in house code to solve the mode resolved AGF for large atomistic structures and embedded force constant from phonopy. Our verifications were done for pure graphene structures and empirical potential (Tersoff potential). Verification process takes two folds: one is to verify the propagating wavefunctions (corresponding to section 5.7 remarks 6) and second is to verify the reconstructed total transmission function based on the mode resolved transmission functions (e.g., check the equivalency of results of 5-54 or 5-55 with 3-65). The figure 28 compares the dispersion between propagating wavefunctions on the left or right lead obtained from mode resolved AGF simulation of pure graphene with the dispersion directly calculated from the phonopy.

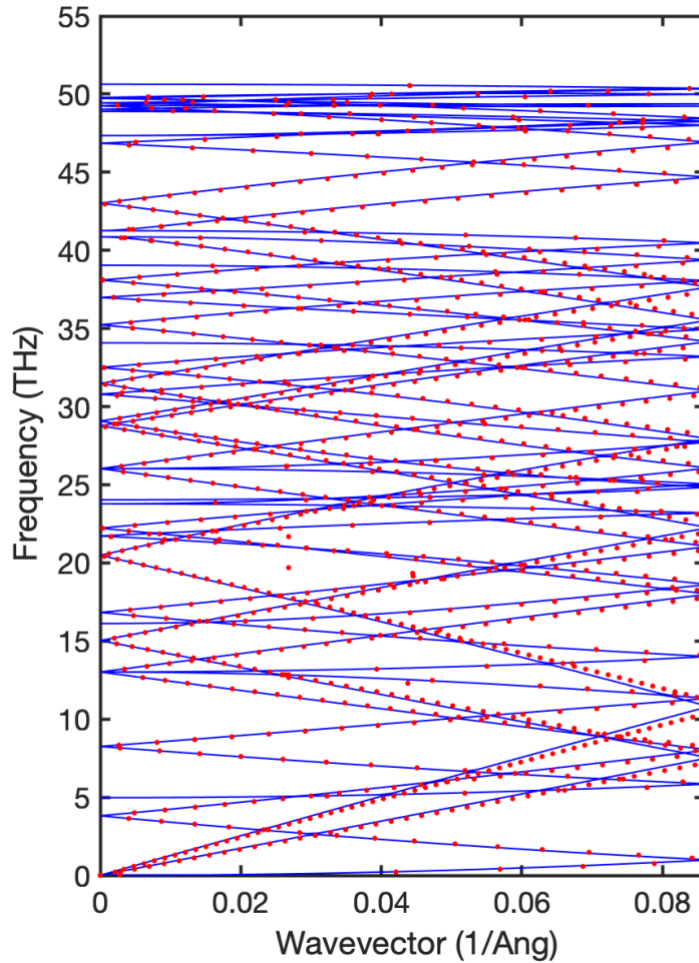


Figure 27 comparison of the dispersion between mode resolved AGF and direct phonopy calculation for pure graphene structure. Blue lines show the direct calculation from phonopy and red dots are the propagating modes of left or right contact calculated from mode resolved AGF solution of pure graphene

There is an excellent agreement between the mode resolved AGF and correct dispersion which indicates that eigenvalue problem based on the Bloch matrices are solved correctly and spatial resolution of mode resolved AGF code is verified. Next step is to verify the mode resolved transmission function. Regarding this step, we show that the trace of the transmission matrices of left and right leads are equivalent to the total transmission function calculated in equations 3-65

and 5-47. Figure 29 shows the comparison of aforementioned transmission functions for pure graphene structure.

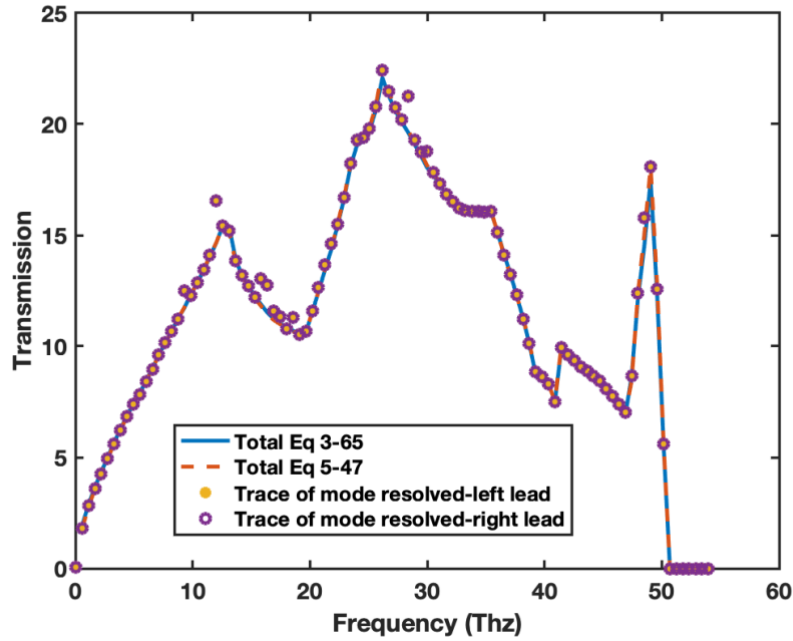


Figure 28 comparison of total transmission functions between total transmission function calculated from equations 3-65 and 5-47 with the trace of mode resolved transmission matrices of left and right leads

There is an excellent agreement between all the transmission function calculations. This means that decomposition of transmitting waves and reconstruction of total transmission through the trace calculation is validated. Successful outputs of above two-step process concludes the verification of the mode resolved AGF code.

5.9 Appendices

5.9.1 Appendix A: Boundary Condition for the Left Side of the Device

Here is the proof for the abbreviated terms of Hamiltonian matrices and the source term.

We begin with the dynamical equation for the unit 0

$$-H_{0,-1}u_{-1} + (\omega^2\mathbf{I} - H_{0,0})u_0 - H_{0,1}u_1 = 0 \quad 5-A1$$

If we put the given boundary condition based on the Bloch matrices into 5-A1, we get

$$\begin{aligned} -B_L([F_L^{-1}(+) - F_L^{-1}(-)]u_0(+) + F_L^{-1}(-)u_0) \\ + (\omega^2\mathbf{I} - H_{0,0})u_0 - H_{0,1}u_1 = 0 \end{aligned} \quad 5-A2$$

where it can be simplified as

$$\begin{aligned} -B_L[F_L^{-1}(+) - F_L^{-1}(-)]u_0(+) - B_L F_L^{-1}(-)u_0 \\ + (\omega^2\mathbf{I} - H_{0,0})u_0 - H_{0,1}u_1 = 0 \end{aligned} \quad 5-A3$$

If we simplify the operator multipliers and take the remaining to the right-hand side, we get

$$\begin{aligned} (\omega^2\mathbf{I} - [H_{0,0} + B_L F_L^{-1}(-)])u_0 - H_{0,1}u_1 \\ = B_L[F_L^{-1}(+) - F_L^{-1}(-)]u_0(+) \end{aligned} \quad 5-A4$$

comparing 5-A4 with the equation 5-A10, we can write the abbreviated terms of the similar equation as

$$\begin{aligned} H'_{0,0} &= [H_{0,0} + B_L F_L^{-1}(-)] \\ H'_{0,-1} &= 0 \\ Q_0 &= B_L[F_L^{-1}(+) - F_L^{-1}(-)] \\ Q_i &= 0, i = 1, \dots, r + 1 \end{aligned} \quad 5-A5$$

5.9.2 Appendix A: Boundary Condition for the Right Side of the Device

Similarly, here we pursue the same process as left side. We begin with the dynamical equation for the unit $r + 1$ which is closest to the device

$$-H_{r+1,r}u_r + (\omega^2\mathbf{I} - H_{r+1,r+1})u_{r+1} - H_{r+1,r+2}u_{r+2} = 0 \quad 5-A6$$

We impose the given boundary condition of the right side

$$-H_{r+1,r}u_r + (\omega^2\mathbf{I} - H_{r+1,r+1})u_{r+1} - B_R^\dagger F_R(+)u_{r+2} = 0 \quad 5-A7$$

and by simplifications, the abbreviated terms are calculated as

$$\begin{aligned} H'_{r+1,r+1} &= H_R + B_R^\dagger F_R(+) \\ H'_{r+1,r+2} &= 0 \\ H'_{0,-1} &= 0 \\ Q_i &= 0, i = 1, \dots, r + 1 \end{aligned} \quad 5-A8$$

5.9.3 Appendix B: Mode Group Velocity

Here we show how the mode group velocity is derived. We begin with equation 5-5 which is multiplied by a Bloch factor

$$-B\bar{u}_n\tilde{u}_m + (\omega^2\mathbf{I} - H_{i,i})\lambda_n\bar{u}_n\tilde{u}_m^* - B^\dagger\lambda_n^2\bar{u}_n\tilde{u}_m = 0 \quad 5-B1$$

Here we dropped (\pm) for a sake of simplicity. Also, we can show the conjugate transpose of 5-B1 which is

$$-B^\dagger\bar{u}_n\tilde{u}_m + (\omega^2\mathbf{I} - H_{i,i})\lambda_m^*\bar{u}_n\tilde{u}_m - B(\lambda_m^*)^2\bar{u}_n\tilde{u}_m = 0 \quad 5-B2$$

If we subtract the 5-B2 from 5-B1, we end up getting the following relation:

$$[B^\dagger\lambda_n\bar{u}_n\tilde{u}_m - B\lambda_m^*\bar{u}_n\tilde{u}_m](1 - \lambda_m^*\lambda_n) = 0 \quad 5-B3$$

and we know that $\lambda_m^* \lambda_n \neq 1$, therefore $[B^\dagger \lambda_n \bar{u}_n \tilde{u}_m - B \lambda_m^* \bar{u}_n \tilde{u}_m] = 0$. This term is the mode group velocity which in the compact form is given as

$$V(\pm) = i[U^\dagger(\pm)B^\dagger U(\pm)\Lambda(\pm) - \Lambda^\dagger(\pm)U^\dagger(\pm)BU(\pm)] \quad 5-B4$$

Similarly, we can derive the mode group velocity based on the self-advance matrices, thus we get

$$V(\pm) = i[U^{a\dagger}(\pm)B^\dagger U^a(\pm)\Lambda^a(\pm) - \Lambda^{a\dagger}(\pm)U^{a\dagger}(\pm)BU^a(\pm)] \quad 5-B5$$

which is also equivalent to

$$V(\pm) = i \left[\left(\Lambda^{a\dagger}(\pm) \right)^{-1} U^{a\dagger}(\pm) B^\dagger U^a(\pm) - U^{a\dagger}(\pm) B U^a(\pm) \left(\Lambda^a(\pm) \right)^{-1} \right] \quad 5-B6$$

5.9.4 Appendix C: Gram-Schmidt Procedure and QR Decomposition

The purpose of the Gram-Schmidt procedure is to orthonormalize the set of vectors which are slightly deviated through non-orthogonality. Here we define

$$\text{proj}_u(v) = \frac{\langle u, v \rangle}{\langle u, u \rangle} u \quad 5-C1$$

where $\langle \quad \rangle$ indicates the inner product. This relation rotates the matrix u into the direction which is orthogonal to the v . If we recursively do this for a set of non-orthogonal vectors of v_k , $k = 0, 1, \dots$, we can define the corresponding set of vectors which are orthogonal like as

$$u_{k+1} = v_{k+1} - \text{proj}_{v_k}(v_{k+1}) \quad 5-C2$$

with the initial condition of $u_0 = v_0$. In principle, column-wise Gram-Schmidt orthonormalization is equivalent to QR decomposition. In our work, we used both Gram-Schmidt and QR decomposition for all the Bloch states.

5.9.5 Appendix D: Propagating Waves

The eigenvalues are pairs function with either propagating or decaying behaviors where the solution is calculated using equation 5-19 for a Bloch state. In an infinite solid only real eigenvalues are available for Bloch states and the complex eigenvalues diverge eventually. In this case, eigenvalues of $\lambda\lambda^\dagger = |\lambda|=1$ are propagating waves and the rest of the modes are evanescent modes. However, for a finite solid, both real and complex eigenvalues are available. As we know for AGF calculation, the complex eigenvalues are important for surface Green's function calculation where a small imaginary value is added to eigenfrequencies. This will displace the propagating modes from the real axis. [157] In order to predict the change in propagating modes, we consider $\delta = 0^+$ as an addition to eigenstates in equation 5-19

$$\begin{aligned} |\exp(ika(\omega + i\delta))| &= \left| \exp\left(ia\left\{k(\omega) + \frac{\partial k(\omega)}{\partial\omega}i\delta + \dots\right\}\right) \right| \\ &= \left| \exp\left(-\frac{\delta a}{v_g}\right) \right| \end{aligned} \tag{5-D1}$$

where a is the size of the Bloch contact unit and v_g is the group velocity of the Bloch state.

Therefore, propagating waves of finite contacts are the ones with the following condition

$$|\lambda| = 1 - \left| \exp\left(-\frac{\delta a}{v_g}\right) \right| \tag{5-D2}$$

Here for forward-going propagating waves $v_g > 0$, then $|\lambda| < 1$. [93]

6.0 Summary and Future Directions

6.1 Summary

In this thesis, we discussed the quantum thermal transport in disordered media such as amorphous Si and grain boundary structures of graphene.

In the second chapter, we demonstrated the effect of MRO on propagon thermal conductivity in amorphous Si. We showed that MRO increases the propagon thermal conductivity up to 50% due to an increase of MFP of propagon modes. Our accomplishments include FEM implementation, equilibrium molecular dynamic simulations, and modal analysis of phonon properties. The outcome of our research was published in the Journal of Applied Physics [13] and was presented in IMECE 2019 [158].

In the third chapter, we lay the foundation for the AGF and the thermal conductance calculations. We particularly discussed the methodologies behind Green's function, AGF, local DOS, transmission function, and Landauer formalism. The in-house code was developed using the AGF simulation code based on the empirical potential which was received from Dr. Esfarjani. Our developments include the generalization of Hamiltonian matrices calculation with force constants calculation from phonopy, enhancing the system of equations solvers and surface Green's function calculations, and implementation of the parallel processing algorithm. Our modifications to the code showed three orders of magnitude reduction in computational cost.

In the fourth chapter, we implemented a simulation framework based on the MLIP to study the thermal resistance for a wide range of GB structures. We used the structural unit model to find a computationally efficient training set with high fidelity and transferability. Our MLIP shows the

high accuracy of thermal properties and interatomic force interactions as well as the ability to capture local atomistic properties such as core and strain energies. We showed 15-35 percent reduction in thermal conductance of GB structures in comparison with pristine graphene at room temperature, and we reported a temperature dependence of thermal conductance which is in contrast with previous studies at low temperatures. Also, we discussed the interplay of dislocation density with out-of-plane buckling and their influence on the scattering of flexural modes at GB. Thus, MLIP is a useful and powerful tool to study the structure with the disorder with a rational computational cost. Additionally, our findings will shed clarity on the growth process of polycrystalline graphene structures and their use in a wide range of applications.

In the fifth chapter, we lay the foundation for the mode resolved AGF in order to calculate the mode resolved transmission where the spatial resolution is resolved. We discussed the methodologies behind the Bloch theorem and Bloch waves, mode matching approach, mode resolved AGF and the connection with the total transmission function. The in-house code was developed for the AGF simulation with the inclusion of the force constants from phonopy calculations.

6.2 Future Directions

The mode matching AGF for ballistic phonon transport has been used in recent works for crystalline graphene structures [159, 160] and non-symmetric graphene GBs [115]; however, the analysis of symmetric graphene's grain boundary structures have not been studied to the best of our knowledge. Thus, it is possible to utilize the mode matching AGF to find detailed information on thermal transport through grain boundary structures. Previously, we discussed the grain

boundary structures perpendicularly placed with respect to the heat carrier's direction since the traditional AGF is unable to address the directionality of heat flux through the grain boundary structures. One possible future direction is to investigate the directionality of the heat carrier dependence on thermal transport through grain boundary structures. Furthermore, mode matching AGF, in contrast to traditional AGF, distinguishes between different polarizations and, as a result of plane wave calculation, allows us to calculate MFP, group velocity, transmission probabilities, and modal transmission. These pieces of information are essential for our understanding of thermal transport through grain boundaries; for instance, in graphene, the flexural branch has an immense contribution to thermal transport; however, these modes' role and contribution are unsettled for graphene's GBs especially the influence of disorder on the scattering process. The previous studies show a direct correlation between buckling of GB scattering of flexural modes in graphene GBs [151, 152], but they do not consider a full range of MAs for graphene GBs and mode conversion analysis of the transmitting modes near the GB disorder. Also, previous works are limited to the use of empirical potentials which are shown to be inaccurate near the GB dislocations.

Additionally, a grain boundary is a disordered structure that alters the structural order from crystallinity and, therefore, the modes with wavelength larger than the structural disorder are more likely to transmit while the modes with wavelengths smaller than the structural order are more likely to behave reflected diffusively. The distinction between the propagating- or diffusive-like behavior is the advantage of mode matching AGF where the modes are polarization-resolved, and the wavelengths are calculated. All in all, a more detailed analysis of phonon transport will be delivered. Finally, the outcome of mode resolved AGF lead to calculating the scattering matrix useful for the simulation of phonon transport based on the Boltzmann transport equation.

Additionally, it is possible to investigate the effect of chemical bonding on thermal conductance. Thermal conductance is significantly affected by the type of chemical bonding, e.g., covalent and ionic bondings. So far, we have discussed the graphene grain boundaries with covalent bondings; however, it is indeed that ionic character adds interesting and challenging issues to the thermal transport problem. Furthermore, in recent years, ionic materials' applications are increasing in compound semiconductors and insulators because of their electronic and optical properties with a larger electronic bandgap compared to covalent bonding semiconductors. Thus, it is important to examine the ionic bonding character of materials (e.g., GaN, h-BN) on thermal conductance and phonon transmission. Our simulation framework for mode matching AGF can be used to study the interplay of the structural order with the wavelengths of transmitting modes through the grain boundaries to understand the thermal resistance of the disorder grain boundary for ionic materials. The differences between ionic and covalent material in two compasses are: one is the difference of atomic structure of dislocations in the grain boundaries, and the second is the presence of Coulomb interaction.

First, it is observed that the dislocations of ionic bonding material have a larger void volume compared with covalent bonding materials. [161] For instance, while the dislocations in graphene consist of heptagon and pentagon [100], the dislocations in h-BN can additionally have square and octagon rings shown in Figure 30 [161]. The square-octagon dislocations are energetically more favorable in ionic bonding materials because it retains no ions with the same charge sign as nearest neighbors. This results in the grain boundary dislocations which are more distinct and variational in terms of structural order. Also, the structural order's variation and distinction would cause a larger variation of force constants near the grain boundaries. Therefore,

we hypothesize the differences in dislocation structures between the covalent and ionic materials affect the thermal transport and scattering process near the grain boundaries.

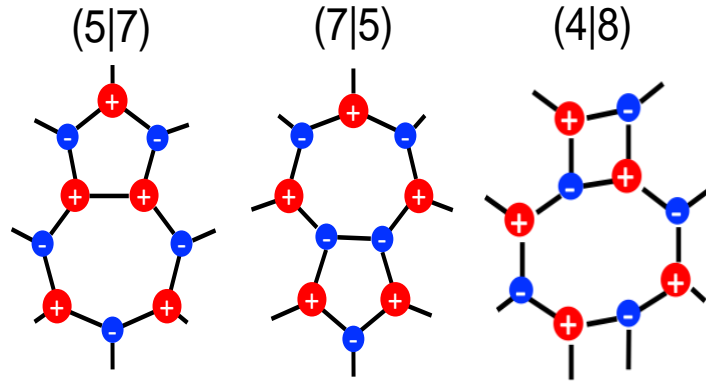


Figure 29. Dislocations in h-BN

Secondly, Coulomb interaction in ionic bonding materials differentiates their characteristics in terms of directionality and the range of interactions compared with covalent materials. In this case, we speculate that the long-range Coulombic interaction would allow more propagating-like transmitting modes and consequently contribute to the larger thermal transport through ionic structures' grain boundaries. However, the disorder grain boundary structure in ionic materials changes the ion's distribution near the grain boundaries and can converse long-range interaction as a transmitting factor. The interplay of the disorder ion's distribution and long-range order interaction and its influences on the total and modal thermal transport is not evident. Therefore, one immediate future direction is to investigate the differences between ionic and covalent structures, and in order to do that, we follow a similar simulation framework to graphene structures. The implemented simulation framework is equipped to capture the modal transmission through the grain boundaries. It is worth mentioning that the thermal transport process for this set of materials has not been investigated to the best of our knowledge.

Bibliography

1. Katie Costello and R.v.d. Meulen. Gartner Identifies Five Emerging Technology Trends That Will Blur the Lines Between Human and Machine. 2018; Available from: <https://www.gartner.com/en/newsroom/press-releases/2018-08-20-gartner-identifies-five-emerging-technology-trends-that-will-blur-the-lines-between-human-and-machine>.
2. Phillpot, S.R. and A.J.H. McGaughey, Introduction to thermal transport. *Materials Today*, 2005. 8(6): p. 18-20.
3. Touloukian, Y.S., et al., Thermophysical properties of matter - the TPRC data series. Volume 1. Thermal conductivity - metallic elements and alloys. (Reannouncement). Data book. 1970.
4. Toberer, E.S., L.L. Baranowski, and C. Dames, Advances in Thermal Conductivity. *Annual Review of Materials Research*, 2012. 42(1): p. 179-209.
5. Yang, H.-S., et al., Anomalously high thermal conductivity of amorphous Si deposited by hot-wire chemical vapor deposition. *Phys. Rev. B*, 2010. 81(10): p. 104203-104203.
6. Kwon, S., et al., Unusually High and Anisotropic Thermal Conductivity in Amorphous Silicon Nanostructures. *ACS Nano*, 2017. 11(3): p. 2470-2476.
7. Braun, J.L., et al., Size effects on the thermal conductivity of amorphous silicon thin films. *Physical Review B*, 2016. 93(14): p. 1-5.
8. Regner, K.T., et al., Broadband phonon mean free path contributions to thermal conductivity measured using frequency domain thermoreflectance. *Nature Communications*, 2013. 4: p. 1640-1647.
9. Larkin, J.M. and A.J.H. McGaughey, Thermal conductivity accumulation in amorphous silica and amorphous silicon. *Physical Review B - Condensed Matter and Materials Physics*, 2014. 89(14).
10. Seyf, H.R. and A. Henry, A method for distinguishing between propagons, diffusions, and locons. *Journal of Applied Physics*, 2016. 120(2): p. 025101.
11. Treacy, M.M.J. and K.B. Borisenko, The local structure of amorphous silicon. *Science (New York, N.Y.)*, 2012. 335(6071): p. 950-3.
12. Treacy, M.M.J., J.M. Gibson, and P.J. Keblinski, Paracrystallites found in evaporated amorphous tetrahedral semiconductors. *Journal of Non-Crystalline Solids*, 1998. 231(1-2): p. 99-110.

13. Hashemi, A., H. Babaei, and S. Lee, Effects of medium range order on propagon thermal conductivity in amorphous silicon. *Journal of Applied Physics*, 2020. 127(4): p. 45109-45109.
14. Schelling, P.K., S.R. Phillpot, and P. Keblinski, Kapitza conductance and phonon scattering at grain boundaries by simulation. *Journal of Applied Physics*, 2004. 95(11): p. 6082-6091.
15. Little, W.A., THE TRANSPORT OF HEAT BETWEEN DISSIMILAR SOLIDS AT LOW TEMPERATURES. *Canadian Journal of Physics*, 1959. 37(3): p. 334-349.
16. Swartz, E.T. and R.O. Pohl, Thermal resistance at interfaces. *Applied Physics Letters*, 1987. 51(26): p. 2200-2202.
17. Swartz, E.T. and R.O. Pohl, Thermal boundary resistance. *Reviews of Modern Physics*, 1989. 61(3): p. 605-668.
18. Sadasivam, S., et al., CHAPTER 4 THE ATOMISTIC GREEN ' S FUNCTION METHOD FOR INTERFACIAL PHONON TRANSPORT. 2014: p. 89-145.
19. Stevens, R.J., L.V. Zhigilei, and P.M. Norris, Effects of temperature and disorder on thermal boundary conductance at solid–solid interfaces: Nonequilibrium molecular dynamics simulations. *International Journal of Heat and Mass Transfer*, 2007. 50(19-20): p. 3977-3989.
20. Deng, B., et al., Kapitza resistance of Si/SiO₂ interface. *Journal of Applied Physics*, 2014. 115(8).
21. Schelling, P.K., S.R. Phillpot, and P. Keblinski, Comparison of atomic-level simulation methods for computing thermal conductivity. *Physical Review B - Condensed Matter and Materials Physics*, 2002. 65(14): p. 1-12.
22. Ong, Z.-y. and G. Zhang, Efficient approach for modeling phonon transmission probability in nanoscale interfacial thermal transport. 2015. 174302: p. 1-17.
23. Sadasivam, S., et al., the Atomistic Green'S Function Method for Interfacial Phonon Transport. *Annual Review of Heat Transfer*, 2014. 17(N/A): p. 89-145.
24. Zhang, W., T.S. Fisher, and N. Mingo, Simulation of Interfacial Phonon Transport in Si–Ge Heterostructures Using an Atomistic Green's Function Method. *Journal of Heat Transfer*, 2007. 129(4): p. 483-483.
25. Babaei, H., et al., Machine-learning based interatomic potential for phonon transport in perfect crystalline Si and crystalline Si with vacancies. *Physical Review Materials*, 2019. 3(7).
26. Hashemi, A., et al., Ab initio phonon transport across grain boundaries in graphene using machine learning based on small dataset. 2021.

27. Igram, D., et al., Large and realistic models of amorphous silicon. *Journal of Non-Crystalline Solids*, 2018. 492(February): p. 27-32.
28. Moon, J., B. Latour, and A.J. Minnich, Propagating elastic vibrations dominate thermal conduction in amorphous silicon. *Physical Review B*, 2018. 97(2): p. 1-6.
29. Sosso, G.C., et al., Understanding the thermal properties of amorphous solids using machine-learning-based interatomic potentials. *Molecular Simulation*, 2018. 44(11): p. 866-880.
30. Seyf, H.R. and A. Henry, A method for distinguishing between propagons, diffusions, and locons. *Journal of Applied Physics*, 2016. 120(2).
31. Allen, P.B., et al., Diffusons, locons and propagons: Character of atomic vibrations in amorphous Si. *Philosophical Magazine B: Physics of Condensed Matter; Statistical Mechanics, Electronic, Optical and Magnetic Properties*, 1999. 79(11-12): p. 1715-1731.
32. Allen, P.B. and J.L. Feldman, Thermal conductivity of disordered harmonic solids. *Physical Review B*, 1993. 48(17): p. 12581-12588.
33. Feldman, J.L., et al., Thermal conductivity and localization in glasses: Numerical study of a model of amorphous silicon. *Physical Review B*, 1993. 48(17): p. 12589-12602.
34. Liu, X., et al., High Thermal Conductivity of a Hydrogenated Amorphous Silicon Film. 2009. 035901(January): p. 1-4.
35. He, Y., D. Donadio, and G. Galli, Heat transport in amorphous silicon: Interplay between morphology and disorder. *Applied Physics Letters*, 2011. 98(14).
36. Elliott, S.R., Medium-range structural order in covalent amorphous solids. *Nature*, 1991. 354(6353): p. 445-452.
37. Barkema, G. and N. Mousseau, High-quality continuous random networks. *Physical Review B*, 2000. 62(8): p. 4985-4990.
38. Pedersen, A., L. Pizzagalli, and H. Jónsson, Optimal atomic structure of amorphous silicon obtained from density functional theory calculations Optimal atomic structure of amorphous silicon obtained from density functional theory calculations. 2017.
39. Voyles, P.M., et al., Structure and physical properties of paracrystalline atomistic models of amorphous silicon. *Journal of Applied Physics*, 2001. 90(9): p. 4437-4451.
40. Gibson, J.M. and M.M.J. Treacy, Fluctuation microscopy analysis of amorphous silicon models. *Ultramicroscopy*, 2017. 176: p. 74-79.
41. Hosemann, R. and S.N. Bagchi, *Direct analysis of diffraction by matter*. 1962: North-Holland Publishing Company. 734-734.

42. Elliott, S.R., *Physics of amorphous materials*. 1990: Longman Scientific & Technical.
43. Biswas, P., et al., Real space information from fluctuation electron microscopy : applications to amorphous silicon Real space information from fluctuation electron microscopy : applications to amorphous silicon. *Journal of Physics Condensed Matter*, 2007. 19.
44. Voyles, P.M., et al., Absence of an abrupt phase change from polycrystalline to amorphous in silicon with deposition temperature. *Physical Review Letters*, 2001. 86(24): p. 5514-5517.
45. Bogle, S.N., et al., Quantifying nanoscale order in amorphous materials: Simulating fluctuation electron microscopy of amorphous silicon. *Journal of Physics Condensed Matter*, 2007. 19(45).
46. Gibson, J.M., et al., Substantial crystalline topology in amorphous silicon. *Physical Review Letters*, 2010. 105(12): p. 1-4.
47. Gibson, J.M., M.M.J. Treacy, and P.M. Voyles, Atom pair persistence in disordered materials from fluctuation microscopy. *Ultramicroscopy*, 2000. 83(3-4): p. 169-178.
48. Liu, X., et al., Hydrogen-free amorphous silicon with no tunneling states. *Physical Review Letters*, 2014. 113(2): p. 1-5.
49. Wada, H. and T. Kamijoh, Thermal Conductivity of Amorphous Silicon. *Japanese Journal of Applied Physics*, 1996. 35(5B): p. L648-L648.
50. Cahill, D.G., M. Katiyar, and J.R. Abelson, Thermal conductivity of a-Si:H thin films. *Physical Review B*, 1994. 50(9): p. 6077-6081.
51. Kuo, B.S.W., J.C.M. Li, and A.W. Schmid, Thermal conductivity and interface thermal resistance of Si film on Si substrate determined by photothermal displacement interferometry. *Applied Physics A Solids and Surfaces*, 1992. 55(3): p. 289-296.
52. Zink, B.L., R. Pietri, and F. Hellman, Thermal conductivity and specific heat of thin-film amorphous silicon. *Physical Review Letters*, 2006. 96(5): p. 1-4.
53. Moon, S., et al., Thermal conductivity of amorphous silicon thin films. *International Journal of Heat and Mass Transfer*, 2002. 45(12): p. 2439-2447.
54. Wiczorek, L., H.J. Goldsmid, and G.L. Paul, in *Thermal Conductivity*, D.P.H. Hasselman and J.R. Thomas, Editors., Springer US.
55. Zhang, P., *Atomic Scale Medium Range Order and Relaxation Dynamics in Metallic Glass*. 2018.
56. Tersoff, J., Empirical interatomic potential for silicon with improved elastic properties. *Physical Review B*, 1988. 38(14): p. 9902-9905.

57. Lee, I.H., et al., Computational search for direct band gap silicon crystals. *Physical Review B - Condensed Matter and Materials Physics*, 2014. 90(11).
58. Borisenko, K.B., et al., Medium-range order in amorphous silicon investigated by constrained structural relaxation of two-body and four-body electron diffraction data. *Acta Materialia*, 2012. 60(1): p. 359-375.
59. Nakhmanson, S.M., et al., Realistic models of paracrystalline silicon. *Physical Review B*, 2001. 63(23): p. 235207-235207.
60. Hwang, J. and P.M. Voyles, Microscopy Microanalysis on Cu-Zr Metallic Glass Using a Wide Range of Coherent STEM Probe Size. *Microscopy and Microanalysis*, 2011. 17: p. 67-74.
61. Fan, L., et al., Fluctuation X-ray microscopy : a novel approach for the structural. *Journal of microscopy*, 2007. 225(May 2006): p. 41-48.
62. Maldonis, J.J., J. Hwang, and P.M. Voyles, FEMSIM + HRMC : Simulation of and structural refinement using fluctuation electron microscopy for amorphous materials ☆. *Computer Physics Communications*, 2017. 213: p. 217-222.
63. Julian, N.H., et al., Ultramicroscopy MS – STEM – FEM : A parallelized multi-slice fluctuation TEM simulation tool. *Ultramicroscopy*, 2018. 194(May): p. 117-125.
64. Giri, A., B.F. Donovan, and P.E. Hopkins, Localization of vibrational modes leads to reduced thermal conductivity of amorphous heterostructures. *Phys. Rev. Materials*, 2018. 2(5): p. 56002-56002.
65. Gale, J.D. and A.L. Rohl, The General Utility Lattice Program (GULP). *Molecular Simulation*, 2003. 29(5): p. 291-341.
66. Plimpton, S., Fast parallel algorithms for short-range molecular dynamics. 1995. p. 1-19.
67. McGaughey, A.J.H. and J.M. Larkin, Predicting Phonon Properties From Equilibrium Molecular Dynamics Simulations. *Annual Review of Heat Transfer*, 2014. 17(N/A): p. 49-87.
68. Ziman, J.M., *Electrons and Phonons*. 2001: Oxford University Press, New York.
69. Yazyev, O.V. and S.G. Louie, Topological defects in graphene : Dislocations and grain boundaries. *Physical Review B*, 2010. 81: p. 1-7.
70. Bartók, A.P., et al., Machine Learning a General-Purpose Interatomic Potential for Silicon. *Physical Review X*, 2018. 8(4): p. 041048.
71. Behler, J. and M. Parrinello, Generalized Neural-Network Representation of High-Dimensional Potential-Energy Surfaces. *Physical Review Letters*, 2007. 98(14): p. 146401.

72. Bartók, A.P., et al., Gaussian Approximation Potentials: The Accuracy of Quantum Mechanics, without the Electrons. *Physical Review Letters*, 2010. 104(13): p. 136403.
73. Sosso, G.C., et al., A neural network interatomic potential for the phase change material GeTe. *Physical review B*, 2012. 174103: p. 1-13.
74. Artrith, N., A. Urban, and G. Ceder, Efficient and accurate machine-learning interpolation of atomic energies in compositions with many species. *Physical Review B*, 2017. 96(1): p. 014112.
75. Kolb, B., L.C. Lentz, and A.M. Kolpak, Discovering charge density functionals and structure-property relationships with PROPhet: A general framework for coupling machine learning and first-principles methods. *Scientific Reports*, 2017. 7(1): p. 1192.
76. Zhang, Y., H. Wang, and S. Jiang, Evolution of structural topology of forming nanocrystalline silicon film by atomic-scale-mechanism-driven model based on realistic network. *AIP Advances*, 2018. 8(9).
77. Qian, X. and R. Yang, Temperature effect on the phonon dispersion stability of zirconium by machine learning driven atomistic simulations. *Physical Review B*, 2018. 98(22): p. 224108.
78. Thompson, A.P., et al., Spectral neighbor analysis method for automated generation of quantum-accurate interatomic potentials. *Journal of Computational Physics*, 2015. 285: p. 316-330.
79. Khorshidi, A. and A.A. Peterson, Amp: A modular approach to machine learning in atomistic simulations. *Computer Physics Communications*, 2016. 207: p. 310-324.
80. Deringer, V.L. and G. Csányi, Machine learning based interatomic potential for amorphous carbon. *Physical Review B*, 2017. 95(9): p. 094203.
81. Campi, D., et al., Electron-phonon interaction and thermal boundary resistance at the crystal-amorphous interface of the phase change compound GeTe. *Journal of Applied Physics*, 2015. 117(1): p. 015304.
82. Behler, J., et al., Metadynamics Simulations of the High-Pressure Phases of Silicon Employing a High-Dimensional Neural Network Potential. *Physical Review Letters*, 2008. 100(18): p. 185501.
83. Dragoni, D., et al., Achieving DFT accuracy with a machine-learning interatomic potential: Thermomechanics and defects in bcc ferromagnetic iron. *Physical Review Materials*, 2018. 2(1): p. 013808.
84. Deringer, V.L., C.J. Pickard, and G. Csányi, Data-Driven Learning of Total and Local Energies in Elemental Boron. *Physical Review Letters*, 2018. 120(15): p. 156001.

85. Bartók, A.P. and G. Csányi, Gaussian approximation potentials: A brief tutorial introduction. *International Journal of Quantum Chemistry*, 2015. 115(16): p. 1051-1057.
86. Bartók, A.P., J. Kermode, and N. Bernstein, Machine Learning a General-Purpose Interatomic Potential for Silicon. *Physical Review X*, 2018. 8(4): p. 41048-41048.
87. Bartók, A.P., R. Kondor, and G. Csányi, On representing chemical environments. *Physical Review B - Condensed Matter and Materials Physics*, 2013. 87(18): p. 1-16.
88. Mahoney, M.W. and P. Drineas, CUR matrix decompositions for improved data analysis. *Proceedings of the National Academy of Sciences*, 2009. 106(3): p. 697-702.
89. Snelson, E. and Z. Ghahramani, Sparse Gaussian processes using pseudo-inputs, in *Proceedings of the 18th International Conference on Neural Information Processing Systems*. 2005, MIT Press: Vancouver, British Columbia, Canada. p. 1257–1264.
90. Quinonero Candela, J. and C.E. Rasmussen, A Unifying View of Sparse Approximate Gaussian Process Regression. *Journal of Machine Learning Research*, 2005. 6: p. 1935-1959.
91. Datta, S., *Quantum Transport Atom to Transistor*. 2013.
92. Zhang, W., T.S. Fisher, and N. Mingo, The atomistic Green's function method: An efficient simulation approach for nanoscale phonon transport. *Numerical Heat Transfer, Part B: Fundamentals*, 2007. 51(4): p. 333-349.
93. Wang, J.S., J. Wang, and J.T. Lü, Quantum thermal transport in nanostructures. *European Physical Journal B*, 2008. 62(4): p. 381-404.
94. Sancho, M.P.L., J.M.L. Sancho, and J. Rubio, Quick iterative scheme for the calculation of transfer matrices: application to Mo (100). *Journal of Physics F: Metal Physics*, 1984. 14(5): p. 1205-1215.
95. Sancho, M.P.L., et al., Highly convergent schemes for the calculation of bulk and surface Green functions. *Journal of Physics F: Metal Physics*, 1985. 15(4): p. 851-858.
96. Tian, Z., K. Esfarjani, and G. Chen, Enhancing phonon transmission across a Si / Ge interface by atomic roughness : First-principles study with the Green ' s function method. 2012. 235304: p. 1-7.
97. Tian, Z., K. Esfarjani, and G. Chen, Green's function studies of phonon transport across Si/Ge superlattices. *Physical Review B - Condensed Matter and Materials Physics*, 2014. 89(23).
98. Duong, D.L., et al., Probing graphene grain boundaries with optical microscopy. *Nature*, 2012. 490(7419): p. 235-9.

99. Zheng-Lu Li, Z.-M.L., Hai-Yuan Cao, Ji-Hui Yang, Qiang Shu, Yue-Yu Zhang, H. J. Xiang and X. G. Gong, What are grain boundary structures in graphene? *Nanoscale*, 2014. 6: p. 4309-4315.
100. Ophus, C. and A. Shekhawat, Large-scale experimental and theoretical study of graphene grain boundary structures. *Physical Review B*, 2015. 92: p. 12.
101. Yazyev, O.V. and Y.P. Chen, Polycrystalline graphene and other two-dimensional materials. *nature nanotechnology*, 2014. 9(August): p. 1-13.
102. Yazyev, O.V. and S.G. Louie, Electronic transport in polycrystalline graphene. *Nat Mater*, 2010. 9(10): p. 806-9.
103. Angadi, M.A., et al., Thermal transport and grain boundary conductance in ultrananocrystalline diamond thin films. *Journal of Applied Physics*, 2006. 99(11).
104. Watanabe, T., et al., Thermal conductance across grain boundaries in diamond from molecular dynamics simulation. *Journal of Applied Physics*, 2007. 102(6).
105. Bagri, A., et al., Thermal transport across twin grain boundaries in polycrystalline graphene from nonequilibrium molecular dynamics simulations. *Nano Lett*, 2011. 11(9): p. 3917-21.
106. Červenka, J. and C.F.J. Flipse, Structural and electronic properties of grain boundaries in graphite: Planes of periodically distributed point defects. *Physical Review B*, 2009. 79(19).
107. Fujii, S., et al., Quantitative prediction of grain boundary thermal conductivities from local atomic environments. *Nat Commun*, 2020. 11(1): p. 1854.
108. Amorim, R.G., et al., Topological line defects in graphene for applications in gas sensing. *Carbon*, 2017. 129: p. 803-808.
109. Serov, A.Y., Z.-Y. Ong, and E. Pop, Effect of grain boundaries on thermal transport in graphene. *Applied Physics Letters*, 2013. 102(3).
110. Chen, J.H., et al., Controlled growth of a line defect in graphene and implications for gate-tunable valley filtering. *Physical Review B*, 2014. 89(12).
111. Xu, D., et al., Thermal boundary resistance correlated with strain energy in individual Si film-wafer twist boundaries. *Materials Today Physics*, 2018. 6: p. 53-59.
112. Azizi, K., et al., Kapitza thermal resistance across individual grain boundaries in graphene. *Carbon*, 2017. 125: p. 384-390.
113. Liu, T.-H., et al., Anomalous thermal transport along the grain boundaries of bicrystalline graphene nanoribbons from atomistic simulations. *Carbon*, 2014. 73: p. 432-442.

114. Spiteri, D., J. Anaya, and M. Kuball, The effects of grain size and grain boundary characteristics on the thermal conductivity of nanocrystalline diamond. *Journal of Applied Physics*, 2016. 119(8).
115. Ong, Z.-Y., G. Schusteritsch, and C.J. Pickard, Structure-specific mode-resolved phonon coherence and specularity at graphene grain boundaries. *Physical Review B*, 2020. 101(19).
116. Fei Tian, et al., Unusual high thermal conductivity in boron arsenide bulk crystals. *Science*, 2018. 361: p. 4.
117. Joon Sang Kang, et al., Experimental observation of high thermal conductivity in boron arsenide. *Science*, 2018. 361: p. 4.
118. Sheng Li, et al., High thermal conductivity in cubic boron arsenide crystals. *Science*, 2018. 361: p. 579–581.
119. Lindsay, L., D.A. Broido, and T.L. Reinecke, First-principles determination of ultrahigh thermal conductivity of boron arsenide: a competitor for diamond? *Phys Rev Lett*, 2013. 111(2): p. 025901.
120. Lee, S., et al., Hydrodynamic phonon transport in suspended graphene. *Nat Commun*, 2015. 6: p. 6290.
121. Cepellotti, A., et al., Phonon hydrodynamics in two-dimensional materials. *Nat Commun*, 2015. 6: p. 6400.
122. Jeong, J., et al., Transient Hydrodynamic Lattice Cooling by Picosecond Laser Irradiation of Graphite. *Phys Rev Lett*, 2021. 127(8): p. 085901.
123. Huberman, S., et al., Observation of second sound in graphite at temperatures above 100 K. *Science*, 2019. 364: p. 4.
124. Rohskopf, A., et al., Fast & accurate interatomic potentials for describing thermal vibrations. *Computational Materials Science*, 2020. 184.
125. George, J., et al., Combining phonon accuracy with high transferability in Gaussian approximation potential models. *J Chem Phys*, 2020. 153(4): p. 044104.
126. Korotaev, P., et al., Accessing thermal conductivity of complex compounds by machine learning interatomic potentials. *Physical Review B*, 2019. 100(14).
127. Mortazavi, B., et al., Materials Horizons Machine-learning interatomic potentials enable first-principles multiscale modeling of lattice thermal conductivity in graphene/borophene heterostructures. *Materials Horizons*, 2020. 7(9).
128. Zhang, Y., et al., Thermal conductivity of h-BN monolayers using machine learning interatomic potential. *J Phys Condens Matter*, 2021. 33(10): p. 105903.

129. Carrete, J., et al., Nanoscale and twin boundaries in semiconducting nanowires. *Nanoscale*, 2019. 11: p. 16007-16016.
130. Behler, J., Atom-centered symmetry functions for constructing high-dimensional neural network potentials. *J Chem Phys*, 2011. 134(7): p. 074106.
131. Behler, J., First Principles Neural Network Potentials for Reactive Simulations of Large Molecular and Condensed Systems. *Angewandte Chemie - International Edition*, 2017. 56(42): p. 12828-12840.
132. Shapeev, A.V., Moment Tensor Potentials: A Class of Systematically Improvable Interatomic Potentials. *Multiscale Modeling & Simulation*, 2016. 14(3): p. 1153-1173.
133. Pun, G.P.P., et al., Physically informed artificial neural networks for atomistic modeling of materials. *Nature Communications*, 2019. 10(2339): p. 1-10.
134. Mortazavi, B., et al., Exploring phononic properties of two-dimensional materials using machine learning interatomic potentials. *Applied Materials Today*, 2020. 20.
135. Tersoff, J., New empirical approach for the structure and energy of covalent systems. *Physical Review B*, 1988. 37(12): p. 6991-7000.
136. Lindsay, L., D.A. Broido, and N. Mingo, Flexural phonons and thermal transport in graphene. *Physical Review B*, 2010. 82(11).
137. Deringer, V.L., et al., Realistic Atomistic Structure of Amorphous Silicon from Machine-Learning-Driven Molecular Dynamics. *The Journal of Physical Chemistry Letters*, 2018. 9(11): p. 2879-2885.
138. Vandermause, J., et al., On-the-fly active learning of interpretable Bayesian force fields for atomistic rare events. *npj Computational Materials*, 2020. 6(1).
139. Xie, Y., et al., Bayesian force fields from active learning for simulation of inter-dimensional transformation of stanene. *npj Computational Materials*, 2021. 7(1).
140. Sivaraman, G., et al., Machine-learned interatomic potentials by active learning: amorphous and liquid hafnium dioxide. *npj Computational Materials*, 2020. 6(1).
141. Sutton, A.P. and V. Vitek, On the structure of tilt grain boundaries in cubic metals I. Symmetrical tilt boundaries. *Philosophical Transactions of the Royal Society A*, 1983. 309: p. 36.
142. Sutton, A.P. and V. Vitek, On the structure of tilt grain boundaries in cubic metals II. Symmetrical tilt boundaries. *Philosophical Transactions of the Royal Society A*, 1983. 309: p. 18.

143. Sutton, A.P. and V. Vitek, On the structure of tilt grain boundaries in cubic metals III. Symmetrical tilt boundaries. *Philosophical Transactions of the Royal Society A*, 1983. 309: p. 14.
144. Rosenbrock, C.W., et al., Discovering the building blocks of atomic systems using machine learning : application to grain boundaries. *npj Computational Materials*, 2017. 3(April): p. 1-6.
145. Togo, A. and I. Tanaka, First principles phonon calculations in materials science. *Scripta Materialia*, 2015. 108: p. 1-5.
146. Plimpton, S., Fast parallel algorithms for short-range molecular dynamics. *Journal of Computational Physics*, 1995. 117: p. 1-19.
147. Shekhawat, A., C. Ophus, and R.O. Ritchie, A generalized Read–Shockley model and large scale simulations for the energy and structure of graphene grain boundaries. *RSC Advances*, 2016. 6(50): p. 44489-44497.
148. Koehler, J.S., On the Dislocation Theory of Plastic Deformation. *Physical Review*, 1941. 60(5): p. 397-410.
149. Read, W.T. and W. Shockley, Dislocation Models of Crystal Grain Boundaries. *Physical Review*, 1950. 78(3): p. 275-289.
150. Carlsson, J.M., L.M. Ghiringhelli, and A. Fasolino, Theory and hierarchical calculations of the structure and energetics of [0001] tilt grain boundaries in graphene. *Physical Review B*, 2011. 84(16).
151. Helgee, E.E. and A. Isacsson, Scattering of flexural acoustic phonons at grain boundaries in graphene. *Physical Review B*, 2014. 90(4).
152. Helgee, E.E. and A. Isacsson, Diffraction and near-zero transmission of flexural phonons at graphene grain boundaries. *Physical Review B*, 2015. 91(20).
153. Ando, T., Quantum point contacts in magnetic fields. *Physical Review B*, 1991. 44(44): p. 8017-8027.
154. ; Available from: https://en.wikipedia.org/wiki/Bloch%27s_theorem.
155. Khomyakov, P.A., et al., Conductance calculations for quantum wires and interfaces : Mode matching and Green ' s. 2005: p. 1-13.
156. Caroli, C., et al., A direct calculation of the tunnelling current. II. Free electron description. *J. Phys.-Cond. Matt.*, 1971. 4.
157. Velev, J. and W. Butler, On the equivalence of different techniques for evaluating the Green function for a semi-infinite system using a localized basis. *Journal of Physics: Condensed Matter*, 2004. 16(21): p. R637-R657.

158. Amirreza Hashemi, H.B., Ruiqiang Guo, Sangyeop Lee. Thermal Transport in Crystalline Si With Vacancies and Amorphous Si. in ASME 2019 International Mechanical Engineering Congress and Exposition. 2019. Salt Lake city, Utah.
159. Ong, Z.-y., Atomistic S -matrix method for numerical simulation of phonon reflection , transmission , and boundary scattering. PHYSICAL REVIEW B, 2018. 195301: p. 1-18.
160. Ong, Z.-Y. and M.-H. Bae, Energy dissipation in van der Waals two-dimensional devices. 2019: p. 1-59.
161. Liu, Y., X. Zou, and B.I. Yakobson, Dislocations and Grain Boundaries in Two-Dimensional Boron Nitride. ACS Nano, 2012. 6(8): p. 7053-7058.